論文 / 著書情報
Article / Book Information

題目(和文)	
Title(English)	HIGH-ASPECT-RATIO RECTANGULAR JET ACTIVE FLOW CONTROLLED BY DIELECTRIC-BARRIER-DISCHARGE PLASMA ACTUATORS
著者(和文)	PhamAnh Viet
Author(English)	Anh Viet Pham
出典(和文)	学位:博士(工学), 学位授与機関:東京工業大学, 報告番号:甲第12574号, 授与年月日:2023年9月22日, 学位の種別:課程博士, 審査員:因幡 和晃,吉田 和弘,齊藤 滋規,秋田 大輔,土方 亘
Citation(English)	Degree:Doctor (Engineering), Conferring organization: Tokyo Institute of Technology, Report number:甲第12574号, Conferred date:2023/9/22, Degree Type:Course doctor, Examiner:,,,,
学位種別(和文)	博士論文
Type(English)	Doctoral Thesis

HIGH-ASPECT-RATIO RECTANGULAR JET ACTIVE FLOW CONTROLLED BY DIELECTRIC-BARRIER-DISCHARGE PLASMA ACTUATORS

by

PHAM VIET ANH

A dissertation submitted to Tokyo Institute of Technology in fulfillment of the requirements for the degree of Doctor of Engineering.

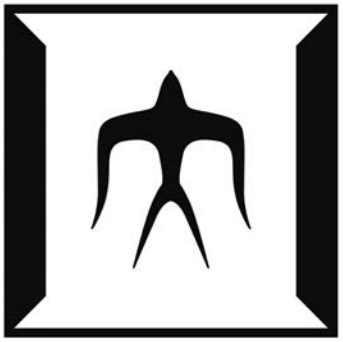

Meguro, Tokyo

March, 2023

Abstract

High-aspect-ratio (HAR) rectangular jets have gained prominence among turbulent jet applications due to excellent mixing, entrainment, and acoustic properties. Active flow controls rectangular jets by Plasma Actuator (PA) is proven to be a promising technique as the actuator is simple in structure, has low energy consumption, and can create different flow features without flow interference. By studying the effects of manipulating turbulent structure, the mechanisms, and operating parameters of the Plasma Actuator effecting the HAR rectangular jet, a deeper understanding of how to optimize and control sub-sonic jets for improved velocity and temperature performance can be obtained. This knowledge can then be applied to designing and developing new automobile air conditioning technologies and leading to advancements in various industries. This research presents the velocity and temperature performance of a high-aspect-ratio rectangular jet controlled by two dielectric barrier discharge plasma actuators located on the longer sides of the nozzle and

controlled by high-voltage and high-frequency pulse-width modulation sinusoidal waves. The scanning method was used to cover 362 cases as combinations of working parameters (modular frequency vs. duty vs. phase difference) for the velocity and temperature performances of the jets. Results show that PAs can control velocity and temperature distribution with minor input power compared with the rectangular jet's kinetic energy and heat flux. Distinctive velocity and temperature distributions were observed under notable cases, indicating the potential of the actuator to create various flow features without installing new hardware on the flow. The velocity increased up to 16%, and the temperature increased up to 14% measured at the automobile driver's position where distance normalized by the jet height x/h = 70 on the centerline. The main mechanisms of PAs to control high-aspect-ratio rectangular jets are multi-scale turbulence structures, energy cascades, and potential vorticity. The combination of the periodic excitation and vectoring effects from the modular actuator frequency and phase difference, respectively, transfers the mean energy of the flow to complex organized structures known as spanwise vortexes having an integral length scale as large as 6 mm. The interaction between these coherent structures and the dissipative environment compresses the vortexes, resulting in rectangular jet width changes as the flow converges on the spanwise-streamwise (X–Y) plane and diverges on the transverse-streamwise

(X–Z) plane. Enhancing or suppressing the integral length scale introduced into the flow at the beginning shear layer can further affect the velocity and temperature performance in the flow field. Flow features and quantitative characteristics of the rectangular jet flow can be predicted for specific cases by calculating the Strouhal number based on PA operating parameters.

Academic Advisor: Kazuaki Inaba

Acknowledgments

First and foremost, I am extremely grateful to my esteemed academic supervisor, Prof. Kazuaki Inaba, for his continuous support, guidance, and valuable ideas. Without the support, advice, and encouragement, I would be unable to finish this doctoral thesis.

My gratitude extends to Mrs. Miyuki Saito, Mr. Toshinori Ochiai, and Dr. Masaharu Sakai, technical experts at DENSO Corporation. They have provided insights and expertise that greatly assisted the research. My appreciation also goes to my laboratory members for their support, friendship, and helpful discussions. I could spend precious time with them since I came to Inaba's laboratory.

Finally, I would like to express my gratitude to my wife, Hai Anh. Without her tremendous understanding, support, and encouragement over the past few years, it would be impossible for me to complete my study.

Contents

List of Tables

List of Figures

Chapter 1

Introduction

1.1 Motivations

Maintaining thermal comfort in car passenger cabins has long been a focus for HVAC (Heating, Ventilation, and Air Conditioning) applications as well as automakers. In that context, High-aspect-ratio (HAR) rectangular air vents have become increasingly popular in modern automobiles due to their numerous benefits to fit various thermal condition of a automobile. These vents, which are characterized by their elongated and slender shape, are particularly useful for providing adequate ventilation within a vehicle.

One of the main reasons for using high-aspect-ratio rectangular air vents in automobiles is to improve the overall airflow within the vehicle. High-aspect-

ratio rectangular air vents, on the other hand, provide a uniform and controlled flow of air, allowing to easily direct air to specific areas such as the front or rear seats. By body part, it is observed that cool and warm sensitivities differ greatly. In contrast, the cheek, neck, back, and seat region are 2-3 times more sensitive to cooling and warming stimuli than the foot, lower leg, and upper chest. Conditioning temperature for sensitive human body parts is important to archive thermal comfort [1]. Using HAR rectangular jet also has another benefit to creating air curtains [2] to archive personal A/C systems capable of controlling the heating/cooling of different areas to fit different thermal conform of passengers as can be seen in Fig. 1.1. High-aspect-ratio rectangular air vents are also highly functional. These vents are typically larger than traditional circular vents, which means that they can provide more air flow with less effort and fewer air vents [3]. This makes them particularly useful for vehicles with larger interiors, where more airflow is needed to cool or heat the cabin effectively.

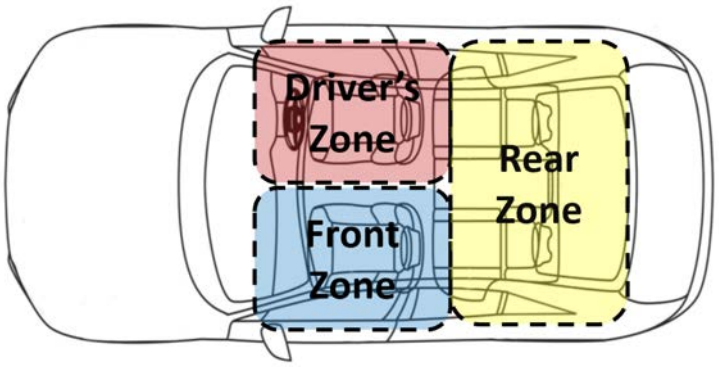

Figure 1.1: Automotive personal A/C system capable of controlling the heating/cooling of different areas.

Another benefit of high-aspect-ratio rectangular air vents is their ability to blend seamlessly into a vehicle's interior design [4]. This type of design motive can be found by both prototype and commercialized automobile models [5] [6] [7] [8]. Automobile interior designers would like to utilize the HAR rectangular jet as these vents have a sleek and modern appearance and can easily be integrated into a vehicle's dashboard without interfering with its overall aesthetic [3]. This makes them particularly useful for vehicle interior design, where a cohesive and stylish design is a crucial selling point.

$$Hf = 0.6 \times C \times V^2 \tag{1.1}$$

where, Hf – Pressure loss (Pa);

C – Pressure loss coefficient due to duct shape;

V – Initial velocity (m/s).

However, there are still engineering challenges to this application's use of rectangular jets. The velocity and temperature far from the distance of the rectangular jet nozzle are challenging to control due to the energy-diffusive nature of the rectangular jet emitted into the still air. Equation 1.1 describes the pressure loss due to the duct shape. Looking at Eq. 1.1, since using any nozzle outlet to discharge air will result in the pressure loss coefficient due to duct shape being $C = 1.0$ [9], hence, pressure loss will be 60% of the total pressure of the A/C system. Therefore, improving the outlet performance will significantly increase the total A/C power efficiency. As a high-aspect-ratio rectangular jet has a narrower opening, the centerline velocity and temperature will decay quickly after the distance from the outlet. Therefore, when it reaches the passengers' position, the velocity and temperature are insufficient to provide thermal comfort. Another challenge is controlling jet width, which is related to the mixing effect to adapt to various thermal situations. This is problematic because the jet width mainly depends on the boundary condition of the jet. Therefore, this research has chosen High-aspect-ratio rectangular jet to improve its flow characteristics, such as mixing, spreading, velocity and temperature decay to benefit automobile as well as various engineering appli-

cations.

There are two approaches to controlling any jet type: passive flow control and active flow control. The passive control approach creates a persistent change in flow; consequently, it is only suitable for the stationary deployment of jets, and it is not adaptable to a rapid-changing environment like an automobile. Active flow control techniques can produce a more significant and precise effect on the flow than passive techniques [10]. Because active flow control techniques use an external energy source, such as an actuator, to manipulate the flow actively, allowing for more precise control and a more substantial effect on the flow compared to passive techniques, which rely on the natural properties of the flow to produce a change. Additionally, it is more flexible and adaptable than passive techniques, as it can be easily adjusted and tuned to have the desired effect on the flow. As a result, the active flow control technique is chosen to control the HAR rectangular jets.

1.2 Research backgrounds

1.2.1 Rectangular Turbulent Jet

Turbulent jets are used in various industrial applications, including air conditioners, combustion, and fuel ejectors. Numerous studies have been conducted on jet properties and their applications, such as a textbook by Rajaratnam [11], the work of Shakouchi regarding the jet flow engineering fundamental [12], the influence of nozzle-exit shape on the performance of the jet by Deo *et al.* [13] and so on. A rectangular jet is a type of fluid flow in which a fluid is ejected from a rectangular opening. The definition sketch for a rectangular jet is shown in Fig. 1.2.

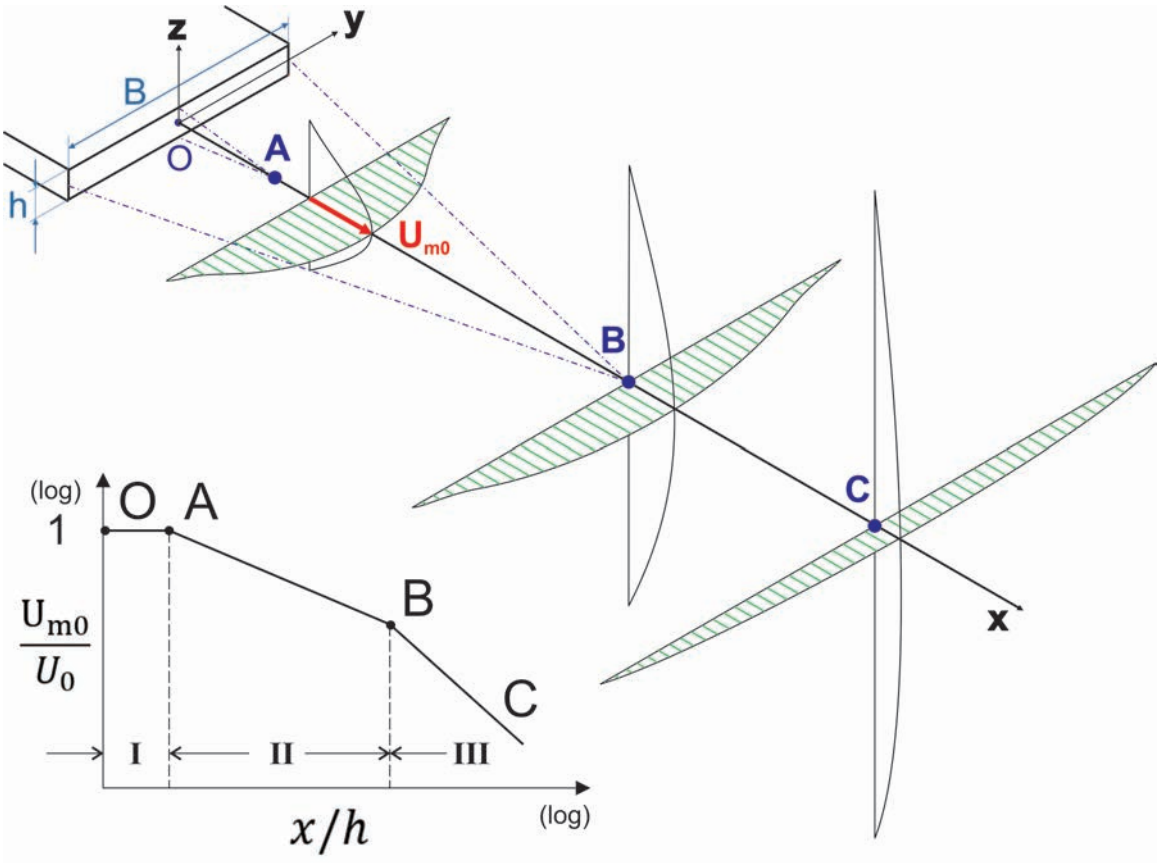

Figure 1.2: Sketch of a rectangular jet. B: nozzle width, h: nozzle height, x, y, z: distance from a suitable origin, U_0: the velocity efflux, U_{m0}: centerline velocities of cut sections. Adapted with permission from Ref. [11] 1976 Elsevier Science & Technology Journals.

The aspect ratio of the rectangular jet is $AR = B/h$, as shown in Fig. 1.2. If $AR > 5$, the jet is classified as a high-aspect-ratio rectangular jet or slender jet. The efflux and centerline velocities are U_0 and U_{m0}, respectively, and the variation of U_{m0}/U_0 with x/h is shown schematically in Fig. 1.2, where x is

the longitudinal distance from the nozzle. Rectangular air jets can be divided into three main zones by Tuve [14], which approximately characterized based on the maximum or center core velocity at the jet cross-section being analyzed (refer to Fig. 1.2): Zone I (line OA), the initial core zone; Zone II (line AB), the transition zone; and Zone III (line BC), the fully developed zone. Zone I is a brief zone that extends from the diffuser face two to six slot widths, depending on the kind of diffuser and the turbulence of the air supply. The centerline velocity of the jet stays about equal to the initial supply velocity throughout its length in this zone.

Zone II is a transitional zone whose length is determined by the shape of the outlet. The transitional zone for a rectangular jet is typically eight or ten widths from the exit. Within this zone, the centerline velocity gradually decreases as follows [15]:

$$U_m/U_0 \propto 1/x^n \tag{1.2}$$

where: n is an index between 0.33 and 1.00.

Zone III is the most important zone for evaluating jet performance since it has a fully formed turbulent flow. It is crucial in engineering applications since

it is generally in this zone that the jet reaches the interested region. The length of this zone is determined by the air jet form, the kind and size of the supply air diffuser, the air jet's beginning velocity, and the turbulence characteristics of the ambient air. The centerline velocity here decreases inversely with the distance from the outlet [15]:

$$U_m/U_0 \propto 1/x \tag{1.3}$$

By using experimental results and some empirical extrapolation, Yevdjevich [11] prepared a useful diagram for anticipating the decay of center-line rectangular jet velocity of multiple aspect ratios displayed in Fig. 1.3 where three characteristic areas could easily be seen. The velocity decay of the jet centerline can be calculated using Eq. (1.4). K_1 is an empirical constant derived from centerline experiment data. Similar work to find K_1 can be obtained from the work of Shepelev [16], Gortler and Tollmein [17], Heskestad [18], and Kotsovinos [19].

$$\frac{U_{m0}}{U_0} = K_1\sqrt{\frac{h}{x}}, \tag{1.4}$$

where,

U_{m0}—Centerline velocity at x;

U_0—Average velocity at outlet where (x_0, y_0, z_0) = (0,0,0);

h—Height of rectangular nozzle; and

K_1—Centerline velocity decay constant.

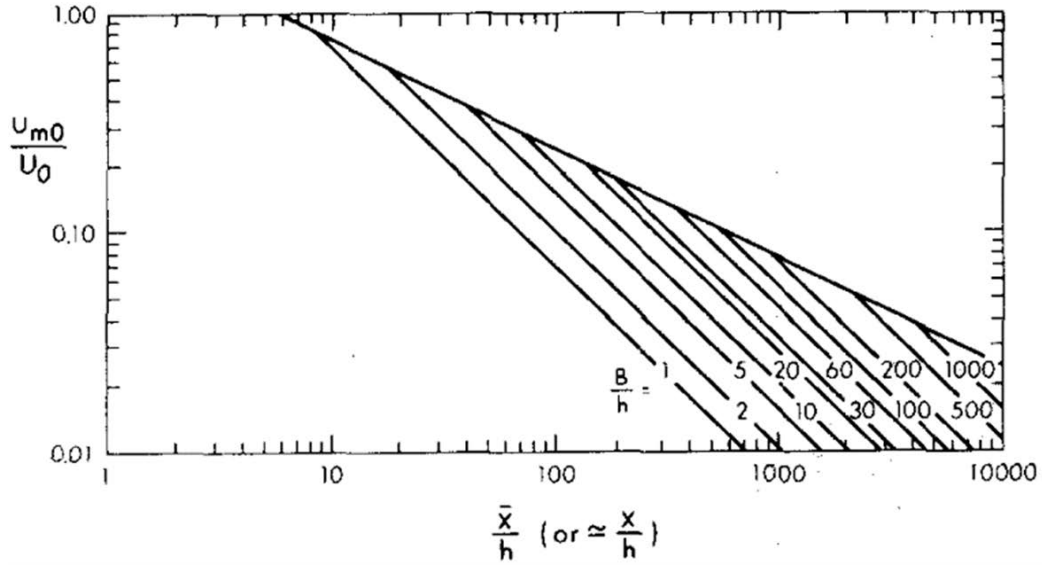

Figure 1.3: Velocity-decay prediction diagram for rectangular jets. Reprint with permission from Ref. [11] 1976 Elsevier Science & Technology Journals.

In term of the temperature decay along the centerline, the phenomenon is like that of centerline velocity. Centerline temperature decay is illustrated on Fig. 1.4. θ_T is the total heat flux across the jet to within ρC_p. It is equal to d_0 if a uniform temperature and velocity distribution at the jet mouth is archived. The decay of the centerline temperature is discovered to behave like the veloc-

ity. The location closed to the outlet exit is called potential core region, where $(T/T_j) = 1$, after that there is the two-dimensional region $(T/T_j)^2 \propto (\theta_T/x)$, and finally a final axisymmetric region extending to infinity where $(T/T_j) \propto (\theta_T/x)$.

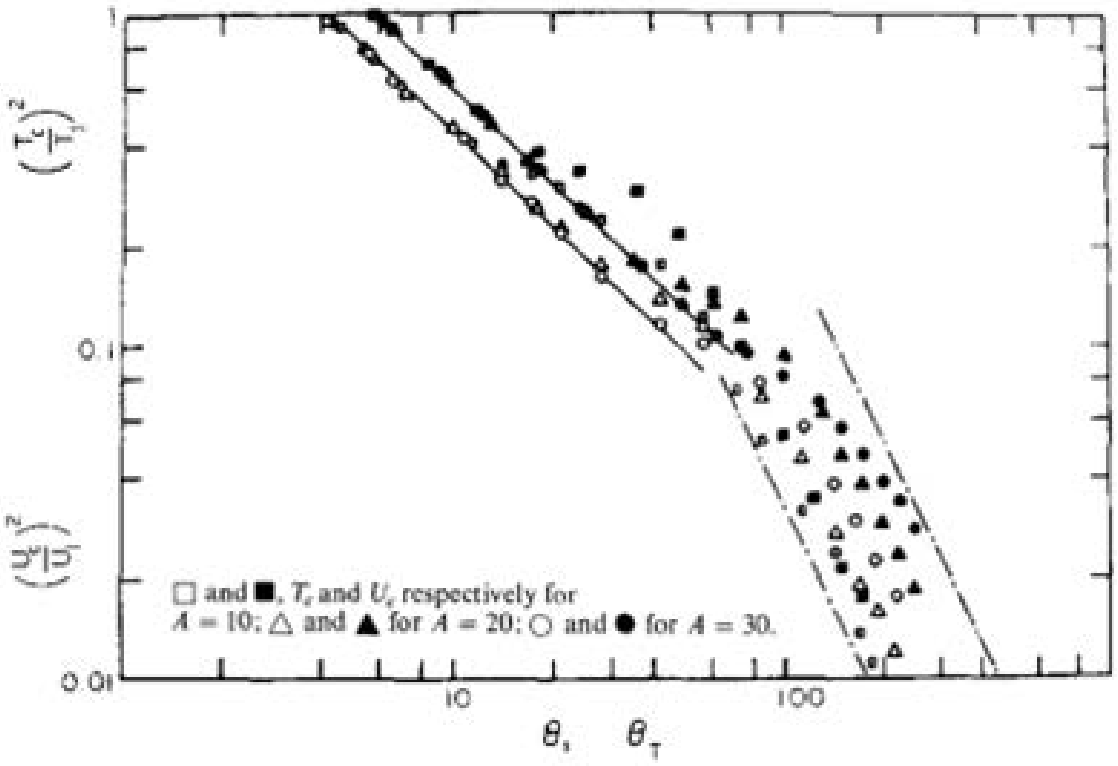

Figure 1.4: Centerline velocity and temperature of rectangular jet. Reprint with permission from Ref. [11] 1976 Elsevier Science & Technology Journals.

The spread of temperature is being quicker than that of momentum. Furthermore, the temperature potential core is shorter than the velocity potential core. The centerline normalized temperature can be calculated by theoretical

work of Koestel [20] in Equation (1.5) and Abramovich [21] in Equation (1.6).

$$\tau_{m0} = \sqrt{0.83 K_2 \frac{h}{x}}, \tag{1.5}$$

$$\tau_{m0} = \frac{1.04}{\sqrt{\frac{ax}{B_0}} + 0.41}, \tag{1.6}$$

where,

τ_{m0}—Normalized centerline temperature at x;

B_0—Half length of nozzle height;

K_2—Centerline temperature decay constant [20];

a—Temperature decay constant [21].

1.2.2 Active Flow Control and Plasma Actuator

1.2.2.1 Overview to Active Flow Control

Active flow control (AFC) refers to techniques used to manipulate the flow of fluids in order to achieve a desired outcome. This can be accomplished through the use of actuators which are used to regulate the flow of the fluid and maintain it at a specific level or within a certain range. Active flow control is often

used in a variety of applications, including HVAC systems, process control in manufacturing, and fluid dynamics research. It is an important tool for optimizing the performance of systems that rely on the flow of fluids, and has the potential to improve efficiency, reduce energy consumption, and increase the accuracy and precision of these systems [10].

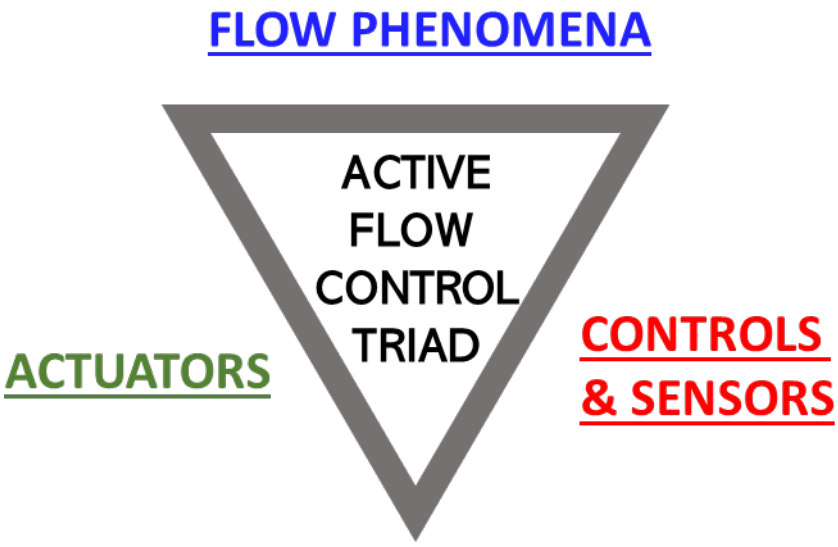

Figure 1.5: The feedback flow control triad [10].

AFC involves the use of sensors to measure characteristics of the flow, actuators to produce forces that alter the flow, and controls to coordinate the operation of the sensors and actuators. There are various types of flow sensors and actuators that can be used in active flow control, each with their own advantages and limitations. The triad of flow control phenomena, actuator-sensors,

and controls is shown in Fig. 1.5 to give an overview of the active flow control technique.

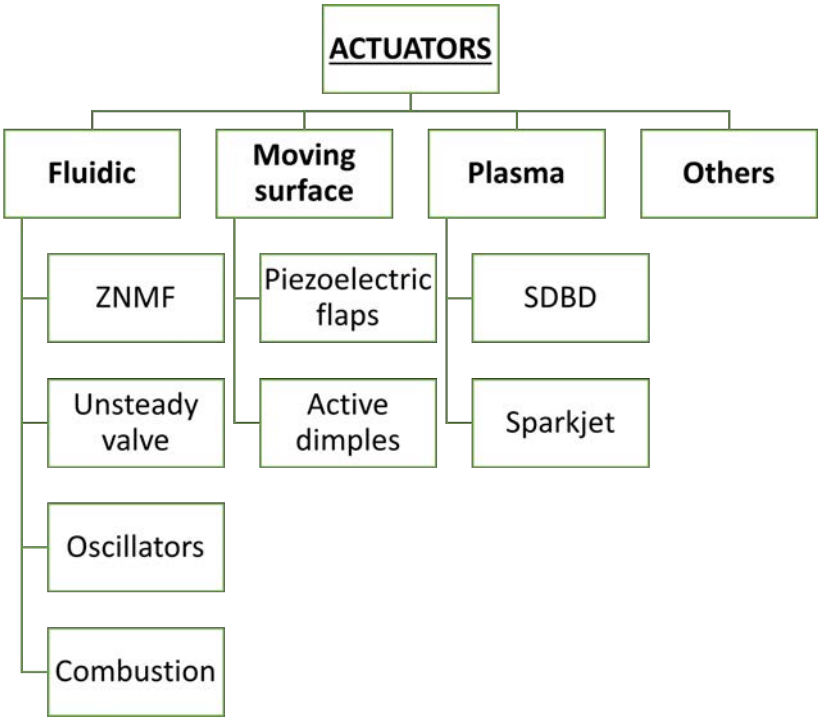

Figure 1.6: A type classification of flow control actuators [22].

In active flow control, flow phenomena refer to the physical characteristics and behavior of the fluid flow in a system. This includes factors such as the velocity and direction of the fluid, as well as the pressure and temperature of the fluid. Based on the motivation of this research, High-aspect-ratio rectangular jet is selected as a triad component. Sensors are devices used to measure the properties of the fluid in a system, such as velocity, temperature, pressure,

and so on. For practical reasons, flow sensors should not interfere so they will not add pressure loss and turbulence to the flow. Sensors can be selected from a wide range of conventional pressure sensors, optical, and MEMs. Control refers to the process of regulating the actuator to interact with the fluid in a system. This is typically done using a controller, which receives input from a flow sensor and activates the appropriate flow actuator to adjust the flow rate as needed. The details of chosen sensors and controls are described in chapter 2.

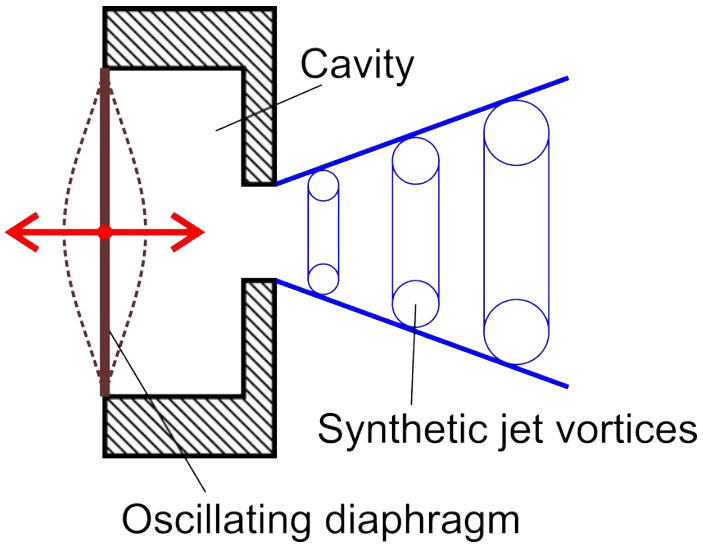

Figure 1.7: Schematic of a typical ZNMF actuator.

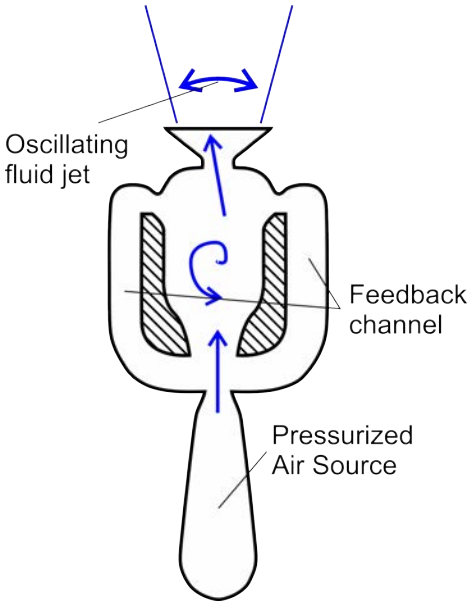

Figure 1.8: Schematic of a Sweeping Jet Actuator.

Last but not least, selecting appropriate actuators plays a vital role in the success of an AFC application. Cattafesta *et al.* [22] summarized a variety of types of actuators suitable for active flow control technique based on their functions, as can be seen in Fig. 1.6. The most common type is fluidic actuators, which utilize the injection or suction of fluids in order to generate control movement. These fluidic actuators can be further divided into two categories: zero-net mass-flux (ZNMF) actuators and synthetic jet actuators. ZNMF actuators (Fig. 1.7) operate by oscillating fluid in and out of an orifice or slot using only the working fluid, without the need for an external fluid source. On the other hand, nonzero net mass-flux actuators require an external fluid

source or sink and utilize a variety of methods to generate fluidic motion, including valves [23], natural fluidic oscillators [24] as can be seen in Fig. 1.8, and combustion-driven devices [24]. These actuators can vary in scale, ranging from traditional macro-scale actuators to extremely small micro-jets. Another class of actuators utilizes a moving object or surface to induce local fluid motion. Examples of this type of actuator include vibrating flaps [25], oscillating wires [26], rotating surface elements [27], and morphing surfaces [28]. These actuators are used to generate movement in a variety of applications, such as laminar boundary layer transition, fluid flow control, and more.

Finally, Plasma Actuators (PA) has recently gained popularity due to their solid-state nature and fast response times [29]. The most popular variant of plasma actuators is the single dielectric barrier discharge (SDBD) plasma actuator, which has been the subject of numerous reviews discussing its physics, design, and applications. Plasma actuators utilize plasma to influence fluid flow, such as air or water. Plasma actuators generate plasma by applying a high-voltage electric field to a gas, causing ionization. When the plasma is applied to a fluid flow, it can alter the flow properties and generate forces that can be used to control the movement of the fluid. Table 1.1 summarize the main advantages and disadvantages of common AFC actuators.

Table 1.1: Summary of common unsteady flow control actuators. Reprint with permission from Ref. [22] 2011 Annual Review of Fluid Mechanics.

Type	Subtype	Advantages	Disadvantages
Fluidic			
	ZNMF	Requires no external fluid source	Peak velocities typically limited to low to moderate subsonic speeds
		Amenable to various types of drivers and sizes	Resonant devices
		Suitable for feedback control	
	Unsteady valves	Capable of high velocities with either fast time response or high bandwidth but generally not both	May not be amenable to feedback control
			Requires an external flow source
	Oscillators	Capable of producing large disturbances	Standard versions not suitable for feedback control
		Amenable to a range of sizes and hence frequencies	Requires an external flow source
		Potential extensions possible to enable independent control of frequency and velocity	
	Combustion	Capable of producing large perturbations in high-speed flows	Currently limited to relatively low frequencies (a few hundred hertz)
			Requires combustion
Moving surface			
	Piezoelectric flaps	Simple design amenable to different frequency ranges of interest	Has constant product of max deflection and bandwidth
		Can produce spanwise or streamwise vorticity	Susceptible to fluid loading
		Suitable for feedback control	Resonant devices
	Active dimples	Potentially suitable for feedback control of turbulent wall-bounded flows	Further development needed to achieve required size and frequency response
Plasma			
	SDBD	Easily installed on models	Limited velocity output
		Low mass	Requires high voltage (kV)
		Fast time response	
		No moving parts	
	Sparkjet	All solid-state device capable of producing large perturbations in high-speed flows	Potential issues associated with EMI, acoustic level, and high temperature

Abbreviations: EMI, electromagnetic interference; SDBD, single dielectric barrier discharge; ZNMF, zero-net mass flux.

Based on table 1.1, the Plasma actuator has advantages over other types of actuators for controlling a high-aspect-ratio rectangular jet in this research:

- Plasma actuators have a short response time, which makes them suitable

for closed-loop control and having potential for high-frequency control;

- Plasma actuators have no moving parts, which makes them more robust and less prone to wear and tear compared to other types of actuators;
- Plasma actuators can be scaled up by staggering multiple devices, which allows for greater control authority;
- Plasma actuators can be easily integrated into a system due to their low system weight, simple and flexible construction, and the fact that they only require electrical power for operation;
- Plasma actuator are suitable for creating various flow features for the rectangular jet at low cost and effort;
- Plasma actuators do not produce significant heat, which is a potential issue with other types of actuators;
- Plasma actuators have a low momentum output, which may be suitable for controlling high-aspect-ratio rectangular jets that require low to moderate sub-sonic speeds;
- Plasma actuators have a very low energy conversion efficiency, which may be a disadvantage in some applications. However, this may not be an

issue in the case of controlling high-aspect-ratio rectangular jets, where low momentum output may be sufficient.

Therefore, Plasma actuator has been chosen as the actuator for active flow control technique applied to controlling the High-aspect-ratio rectangular jets.

1.2.2.2 Introduction to Plasma Actuator

Compared to other types of actuators, the plasma actuator (PA) as an active flow controlling device is relatively simple (as it is only made from copper tape, dielectric tape, and acrylic plate). They are made up of two electrodes separated by a dielectric material. Typically, one of the electrodes is exposed to the atmosphere, as known as the exposed electrode. Dielectric material completely covers the other electrode, which calls the covered electrode. It is more accurate to call this device as a single dielectric barrier discharge (SDBD). In this case, the ”plasma” refers to the ionized air formed by the dielectric over the electrode area. Figure 1.9 demonstrates an illustration of a common plasma actuator SDBD system and an ionized air (plasma) illustrator forming over the dielectric layer-covered electrode in the region.

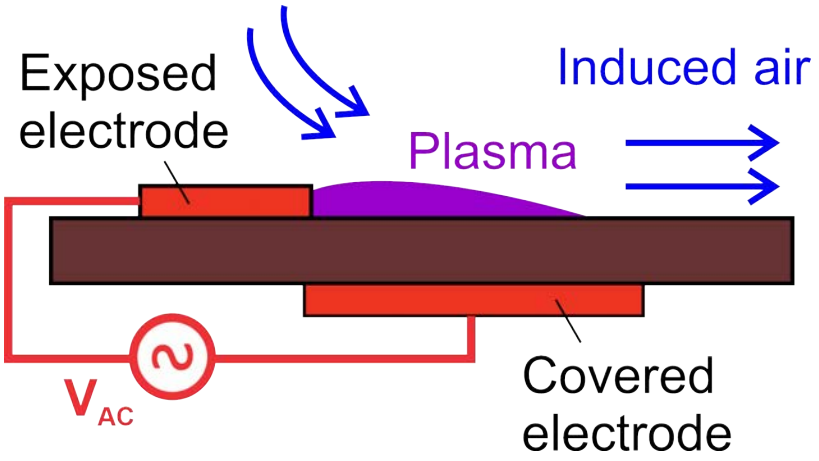

Figure 1.9: Schematic illustration of a SDBD (Single Dielectric-Barrier Discharge) plasma actuator.

A gas discharge is developed when an electric field of adequate amplitude is supplied to a volume of gas to produce electron–ion pairs by electron-impact neutral gas ionization [30]. This involves the existence of an initiating number of free electrons that can either be present from ambient conditions or forcefully introduced. The benefits of Plasma Actuators are being 100% electronic with no moving parts, incredibly fast response time, low mass actuator, low input power, and the easy ability to be implemented in simulation.

Relative humidity (RH) may impact plasma discharge effectiveness by disrupting the plasma regime. Measurements of the induced electric wind clearly show a decline in momentum transfer efficacy as RH levels increase [31]. Electric wind production decreases beyond 70% RH, but the actuator maintains its ability to transmit momentum at the applied electrical frequency. The first sig-

nificant decrease occurred when the RH exceeded 85%. However, increasing the applied high voltage can also easily compensate for the negative effects of high RH on actuator efficacy.

The working principle of an asymmetric-electrode SDBD plasma actuators are described as follow: a downward-induced flow toward the left edge of the enclosed electrode in the direction of the covered electrode, simultaneously, a jet of the stream to the far edge of the covered electrode is formed. There are two main effects caused by the SDBD Plasma Actuator, which are starting a vortex effect and wall jetting effect.

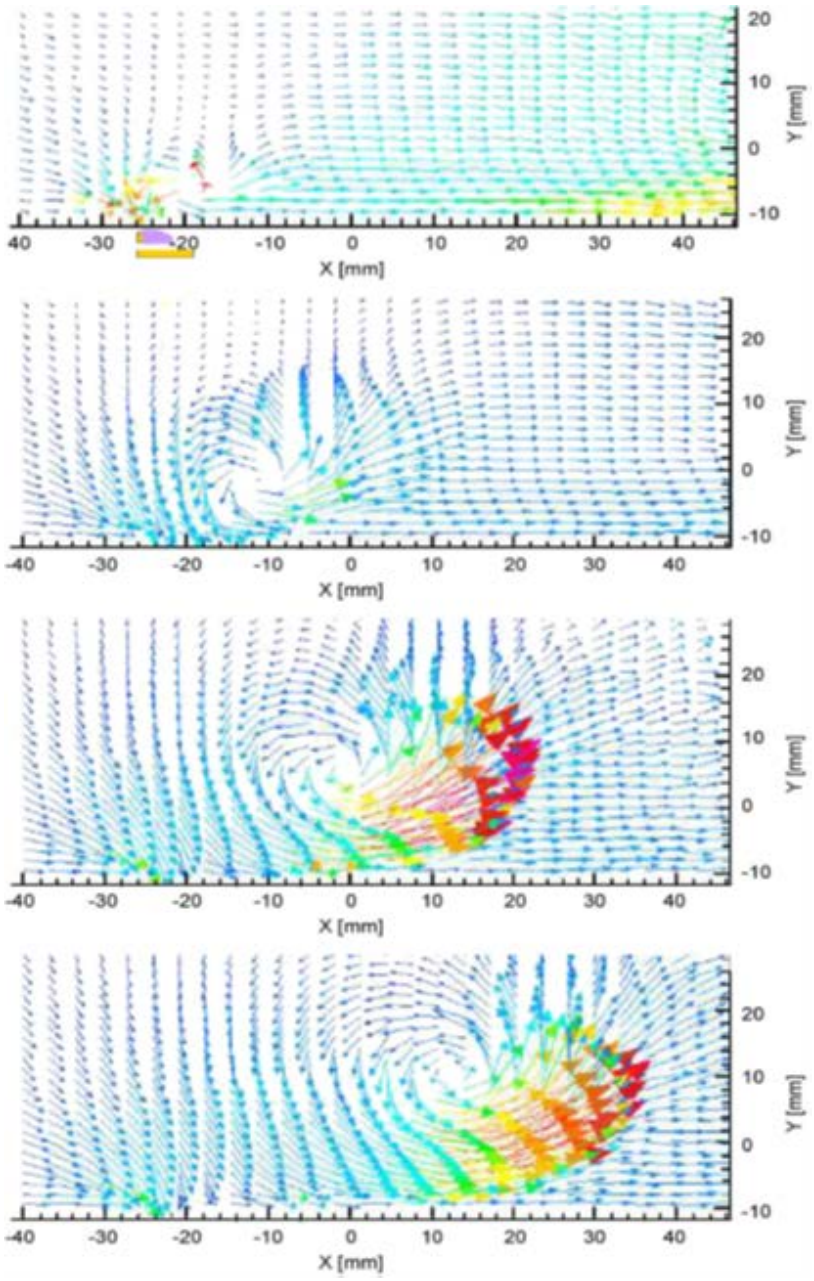

Figure 1.10: PIV image illustrates the flow induced by an SDBD plasma actuator in still air. Reprint with permission from Ref. [32] 2007 Progress in Aerospace Sciences.

A shear layer is developed when DBD plasma is launched in quiescent air,

which rolls up to form a vertical structure. The starting vortex shifted along and away from the wall under continuous plasma forcing. Figure 1.10 shows the velocity vectors of the SDBD, as shown in Figure 1.9, obtained using PIV measurement method [32].

At the top plot, the Plasma Actuator is just start being activated. The velocity vectors are aimed to the wall just upstream of the actuator location. This is noticeable in all plots at all phase angles and is similar with the downward-bent smoke streamline found on the plasma actuator. Near the wall, the vectors show that the flow is accelerating and moving parallel to the wall away from the act. The Plasma Actuator start-up generates a "starting vortex" equivalent to an impulsively moving wall due to that the actuator is in still air.

According to [33], the method of starting vortex formation and growth suggested by WHALLEY indicates that the laterally ejected jet flow was replenished by fluid trapping above the plasma actuator, which created a starting vortex. The secondary vorticity was produced along the wall in order to maintain the no-slip boundary condition as shown in the figure. The secondary vorticity wrapped around the starting vortex and steered away from the wall its path. It is also shown that the plasma momentum improved linearly after the plasma actuator achieved a steady state speed U_0. This indicates that with a steady force, the DBD plasma actuator entrained and accelerated the

surrounding fluid.

After the initiation of Plasma Actuator as known as the starting vortex, steady wall jet was created. The wall jet caused by DBD plasma differs from a classic laminar wall jet because the flow is not mass-added. The plasma actuator brought ambient fluid to the wall here, then ejects this fluid tangentially from the electrode by the plasma ionized air [34], where fluid is driven from just above and upstream of the plasma into the SDBD Plasma Actuator, then laterally driven along the wall by the body force to form the laminar wall jet effect.

1.3 Literature survey

The plasma actuator is described in detail in the review article by Corke *et al.* [29], which highlights some of the capabilities of plasma actuators through examples from experiments and simulations. Benard *et al.* [35] developed an active control device for a circular jet comprised of two plasma actuators combined with a passive diffuser to improve free shear layer mixing significantly. This resulted in increased jet spreading, a shorter potential core, and increased turbulence kinetic energy. Corke *et al.* [36] used phased plasma arrays to control unsteady flow. Their findings showed that a two-frequency phased plasma

array could influence mean and unsteady flow development by increasing actuation velocities compared to a single-frequency, single-phase plasma approach. The plasma produced by an Alternating Current (AC) driven Dielectric barrier discharge (DBD) plasma actuator is a non-thermal plasma in which heavy species have temperatures close to ambient while electron temperatures are much higher [37]. The thermal effect is not responsible for the local airflow produced by a single DBD plasma actuator and has no effect on the flow control process [38].

Rizzetta *et al.* [39] explored different shapes of the plasma actuator, namely standard and serpentine. They found that standard and serpentine actuators performed equally well in LES simulations. The pulsed mode is superior to continuous plasma actuation at lower power consumption. Plasma actuators can also be used to create a novel device, such as the fan-shaped dielectric barrier discharge (DBD) plasma reactor developed by Portugal [40]. It achieved a better ozone distribution in a closed environment than in an ordinary reactor by plasma actuation-induced suction and vortical structures. Research on improving the characteristic of the PA was conducted by Wojewodka [41] to achieve the highest induced velocity of 5.22 m/s by the surface ac-DBD plasma actuator with Kapton compared to those of Teflon and Glass Reinforced Epoxy. Different maximum velocities were obtained with an active plate electrode and

sawtooth electrode by increasing the actuation voltage by Moreau [42]. Furthermore, a new type of stair-shaped dielectric barrier discharge layer was explored by Rodrigues *et al.* [43] to improve the power conversion efficiency up to 5 times more efficiently than conventional actuators.

Many studies have shown that various actuators can control turbulence jet mixing and spreading rates by using appropriate excitation at the jet exit. By utilizing pulsed fluidic piezoelectric wedge actuators, a large spreading can be archived with significant increases in mixing over subsonic and transonic rectangular jets [44]. With modification to the nozzle, a fluidic system using self-excited global oscillations is established in the jet by applying suction to an annular cavity placed around the jet periphery [45]. These oscillations are responsible for enhanced mixing between the jet and the surrounding fluid, and increased mixing appears insensitive to the jet's initial conditions. The acoustic excitation to control the turbulence jet flow is studied in-depth by Ginevsky *et al.* [46]. Another attempt using microelectromechanical systems (MEMS) also demonstrated the efficiency of promoting the initial instabilities of axisymmetric jet flows by Suzuki *et al.* [47]. Pair of plasma actuators were effective at controlling the rectangular jet width, as investigated by Kozato *et al.* [48] when there is a phase difference between the upper and lower PAs.

Based on the literature review, Plasma Actuator is well-developed technol-

ogy for active flow control fluid jet applications. However, only one study has been conducted on DBD plasma actuators with rectangular jets. There are existing research gaps, mainly for using PA to control the temperature of the high-aspect-ratio rectangular jet, the mechanism of how the actuator affects the flow, and which PA operating parameter is essential to focus on for optimization. Plasma Actuator shows the potential to increase the kinetic energy and control the fluid jet's boundary layer and shear layer to archive various effects on the flow. The actuator can alleviate the disadvantages of using high-aspect-ratio rectangular jets as an air vent for automobile A/C systems to archive better air distribution, car interior, or fuel consumption. Therefore, Plasma Actuator is chosen to actively control a HAR rectangular jet for use in an automobile air conditioner system in this research.

Kelvin-Helmholtz Instability (KHI) is the leading cause of velocity and temperature decay on the original rectangular jet. As the jet spreads, minor disturbances begin to form, as shown in Fig. (1.11). This Instability is caused by the difference in velocity between the fluid layers, resulting in the formation of vortices and the breakdown of the laminar flow (or potential core region) [49]. As the vortices grow from disturbances (small in size and number) to "roll-up" vortexes, they begin interacting with each other, creating even more disturbances in the flow. Therefore, applying a small effort of flow control by Plasma

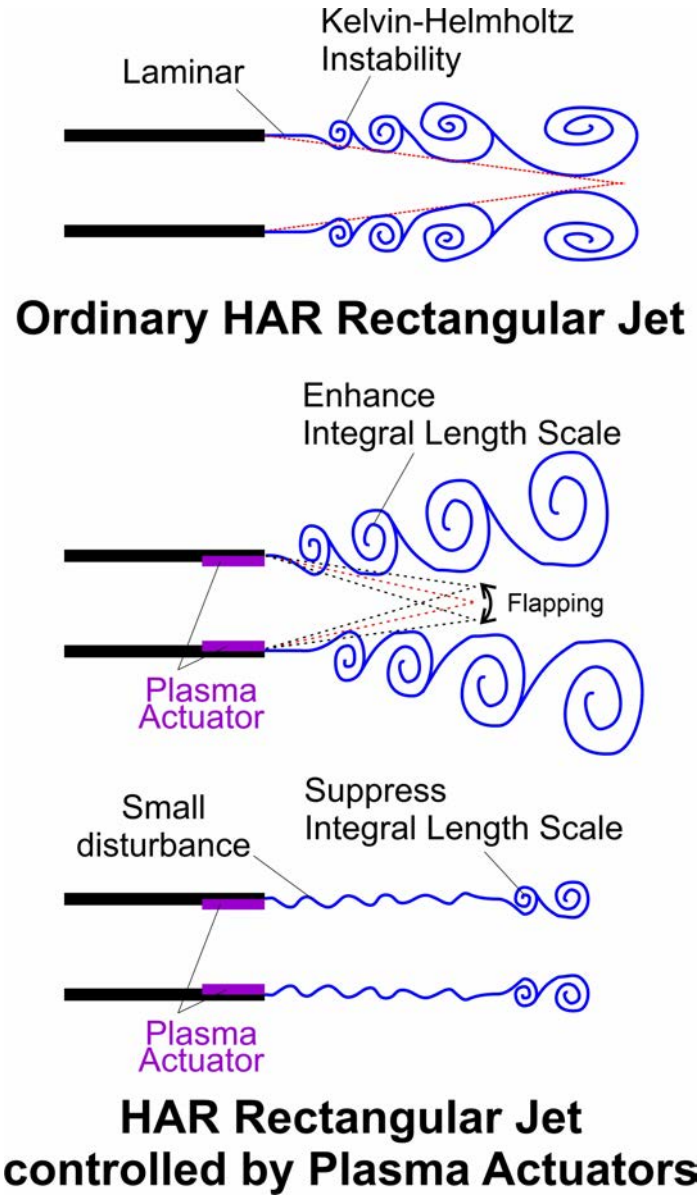

Figure 1.11: Schematic of High-aspect-ratio controlled by a pair Plasma Actuators.

Actuators at the beginning shear layer can further affect the formation of KHI by over-driving this phenomenon. The flow field's velocity and temperature can be controlled through this action.

1.4 Research objective and scope

The research objective is:

To clarify the physical phenomena of the interaction of the High-aspect-ratio Rectangular Jet and Plasma Actuator during the optimization process, with a focus on the delay of the decay of centerline velocity and temperature at the driver's location without increasing the air-conditional system total energy budget.

Understanding the mechanism also opens possibilities for using PAs as a design tool to craft turbulent structures in the flow. As a result, the flow features can be re-created by other active flow control techniques or other types of actuators.

1.5 Outline of thesis

This thesis is divided into four chapters. First, introduction for this thesis is explained in Chapter 1 including motivation, research background of the thesis with the theory of turbulence jets and plasma actuator fundamental, literature survey, and objective of thesis. Afterward, effect of plasma actuator on velocity and temperature profiles of high-aspect-ratio rectangular jet and the mechanisms of high-aspect-ratio rectangular jet width controlled by plasma actuators are provided in Chapters 2 and 3. The more detailed overview of Chapters 2 and 3 are described as follows.

In Chapter 2, the velocity and temperature performance of a high-aspect-ratio rectangular jet controlled by two dielectric barrier discharge plasma actuators located on the longer sides of the nozzle and controlled by high-voltage and high-frequency pulse-width modulation sinusoidal waves. The scanning method was used to cover 362 cases as combinations of working parameters (modular frequency vs. duty vs. phase difference) for the velocity and temperature performances of the jets. Results show that plasma actuators can control both velocity and temperature distribution with minor input power compared with the rectangular jet's kinetic energy and heat flux. Distinctive velocity and temperature distributions were observed under noteworthy cases, indicating

the potential of the actuator to create various flow features without installing new hardware on the flow.

In Chapter 3, this chapter aims to understand the interaction between a PA and rectangular flow with a high aspect ratio of 20. It also investigates the change in jet width using hot-wire anemometry, particle image velocimetry, and theoretical studies. The combination of the periodic excitation and vectoring effects from the modular actuator frequency and phase difference, respectively, transfers the mean energy of the flow to complex organized structures known as spanwise vortexes, which are as large as 6 mm. The interaction between these coherent structures and the dissipative environment compresses the vortexes, resulting in rectangular jet width changes as the flow converges on the spanwise-streamwise (X–Y) plane and diverges on the transverse-streamwise (X–Z) plane. Flow features and quantitative characteristics of the rectangular jet flow controlled by the actuator can be predicted for specific cases by calculating the Strouhal number based on PA operating parameters.

Lastly, in Chapter 4, “Summary, Conclusions and Future Works”, the findings of this research are recapitulated. Future works concerning this thesis are proposed.

Chapter 2

Effect of Plasma Actuator on Velocity and Temperature Profiles of High Aspect Ratio Rectangular Jet

Abstract

In this research, one of the goals is to archive better velocity and temperature performance at the driver's location without increasing the air-conditional system's total energy budget. Since there is limited knowledge in the literature, this chapter will explore effects of Plasma Actuator to the HAR Rectangular Jet to archive better velocity and temperature performances, and ability to create various flow features to fit various working condition of the automobile air conditioner.

2.1 Experiment setup

2.1.1 Apparatus, Velocity Measurement, Temperature Measurement, Pressure Measurement, and Visualization

The experimental setup is illustrated in Fig. 2.1. The experimental system consists of several subsystems. An open-channel wind tunnel Tsukubarika Seiki Co., Ltd, Japan WGT-10 generated airflow at an initial velocity U_0 = 4.5 m/s measured at the nozzle exit. A HAR rectangular jet $AR = B/h = 20$ (B = 150 mm and h = 7.5 mm) was attached to the end of the wind tunnel for the experiments using a 3D printed adapter. With this setup, the Reynolds number of the HAR rectangular jet is 2150; as the experiments have shown, if Re exceeds 2000, the jet flow will be turbulent [50]. Plasma actuators (PAs) were implemented on the nozzle to control the turbulence jet flow actively. The HAR rectangular jet performance was evaluated by measuring the velocity and temperature centerline decay under different plasma actuator operating conditions.

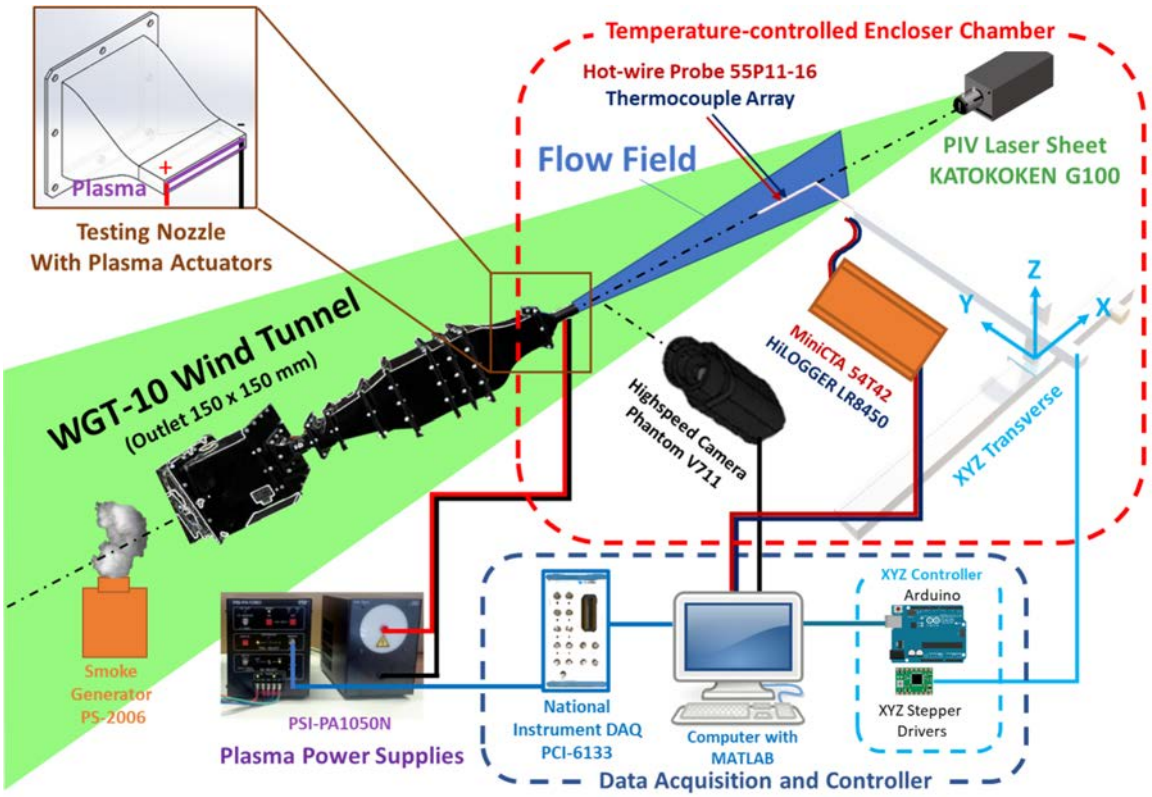

Figure 2.1: Overview of the experiment setup.

Hot-wire anemometry was implemented to measure velocity and integral length and dissipation length scales and analyze the energy density spectrum at specific points. The system included a mini hot-wired constant temperature anemometer (54T42, Dantec Dynamics), miniature X-wire probe (55P61, Dantec Dynamics) for measuring U- and V-velocity components, and probe support (55H25, Dantec Dynamics) for mounting the hot-wire probe. The raw volt-

age data were collected using a data acquisition device (DAQ, PCI-6133, National Instruments) at a 50-kHz sampling rate. The transverse system affixed the hot-wire anemometry system to a controlled XYZ transverse system. This transverse system consisted of an Arduino UNO board as a microcontroller, three stepper motors, and three stepper motor drivers. The system was positioned along the X-, Y-, and Z-axis with a precision of ±0.02 mm. A workstation PC with MATLAB installed collected the hot-wire measurement data through the DAQ device and output measuring point XYZ coordinates to the transverse system as the experimental plan. The origin of the coordinate system where (x_0, y_0, z_0) = (0,0,0) is an identical coordinate system to that in Fig. 1.2 which (x) is the streamwise direction, (y) is the spanwise direction, and (z) is the lateral direction.

The probe was calibrated with the probe located in the middle of the outlet of the wind tunnel. The calibration velocity ranged from 0 to 12 m/s, and the wire voltage was recorded at each velocity. This calibration data was used to convert the wire voltage to velocity. The fast Fourier transform (FFT) was used to extract results, such as the turbulent energy density spectra, integral length scale, and dissipation length scale by processing the velocity data. The process is explained in detail in the study of El-Gabry *et al.* [51].

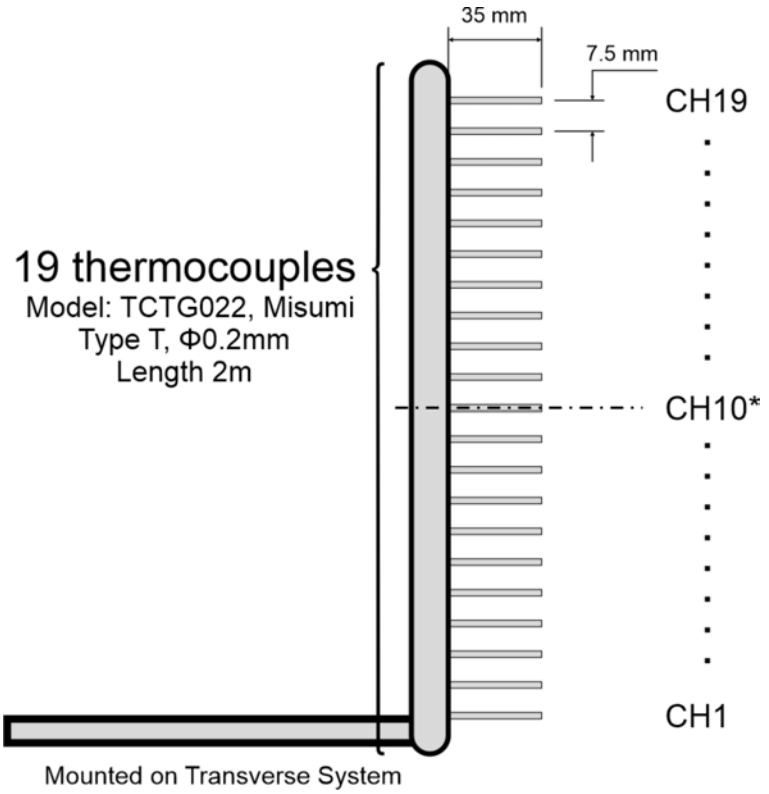

Figure 2.2: The thermocouple array consists of 19 thermocouples used to measure the temperature of flow. CH10* was located in the middle of the array.

An array of 19 thermocouples (TCTG022, MISUMI) was installed in the same XYZ transverse system to measure the temperature of the rectangular jet. The channel arrangement details are shown in Fig. 2.2. The temperature data were recorded using a Hioki Model LR8450 connected to a PC to acquire the data at the sampling rate of the thermocouple was 10 Hz in 30 s for each measurement. In addition to the temperature-measuring equipment, an enclosure chamber (1400 mm × 2140 mm × 1980 mm) made of vinyl-covered

thermal insulation sheets was used to create a controlled temperature environment for the test. The chamber was equipped with 12 ceramic heaters (600 W MISUMI MCHNN2) to heat air. A dual-element thermocouple was installed on top of the nozzle to provide the controlling signal to a proportional-integral-derivative (PID) control unit (OMRON E5EC) and the ambient temperature of the chamber to the data logger. Two solid relays, OMRON G3PJ, received the control signal from the PID control and then drove the ceramic heaters to heat the enclosure to the desired ambient temperature with a precision of ± 1 °C. The wind tunnel inlet installed a circulator chiller YAMATO SCIENCE CF800 and a custom-made radiator to cool the air feeding to the rectangular outlet. A schematic of the experiment is shown in Fig. 2.3.

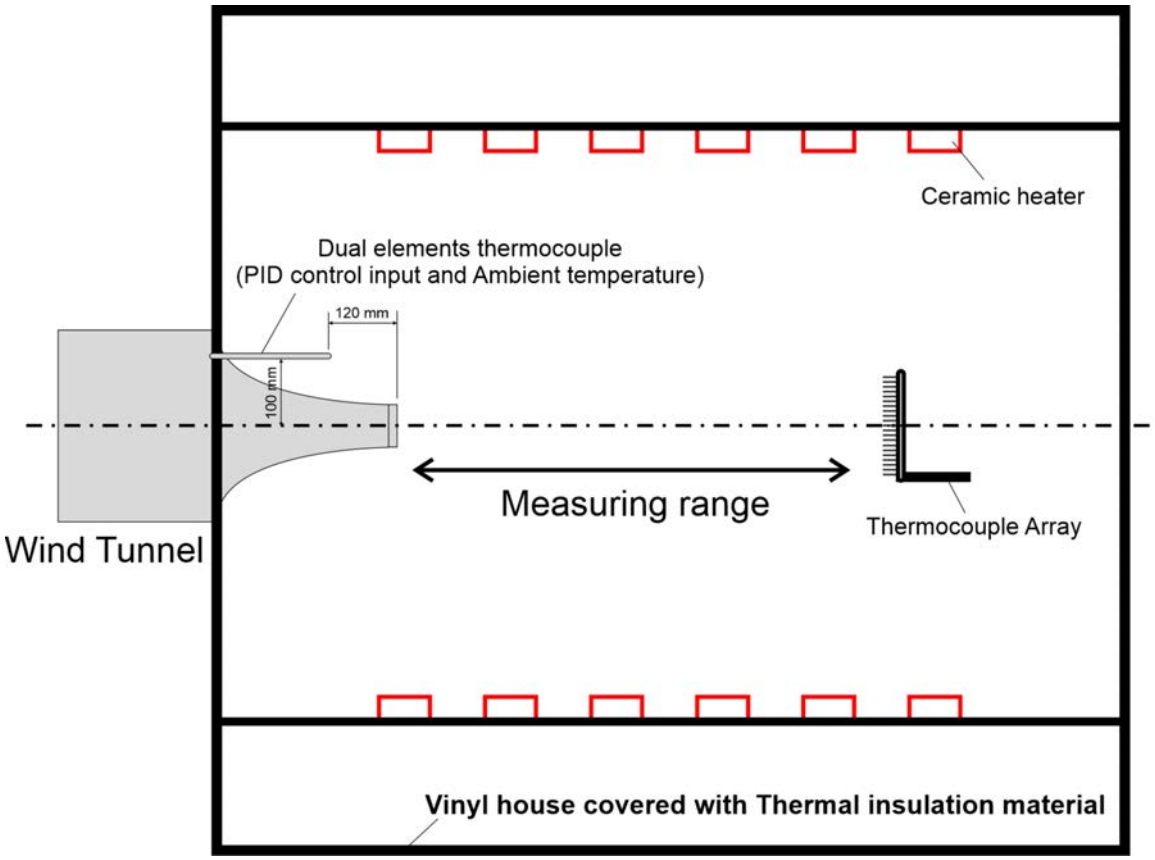

Figure 2.3: Temperature-controlled enclosure chamber schematic.

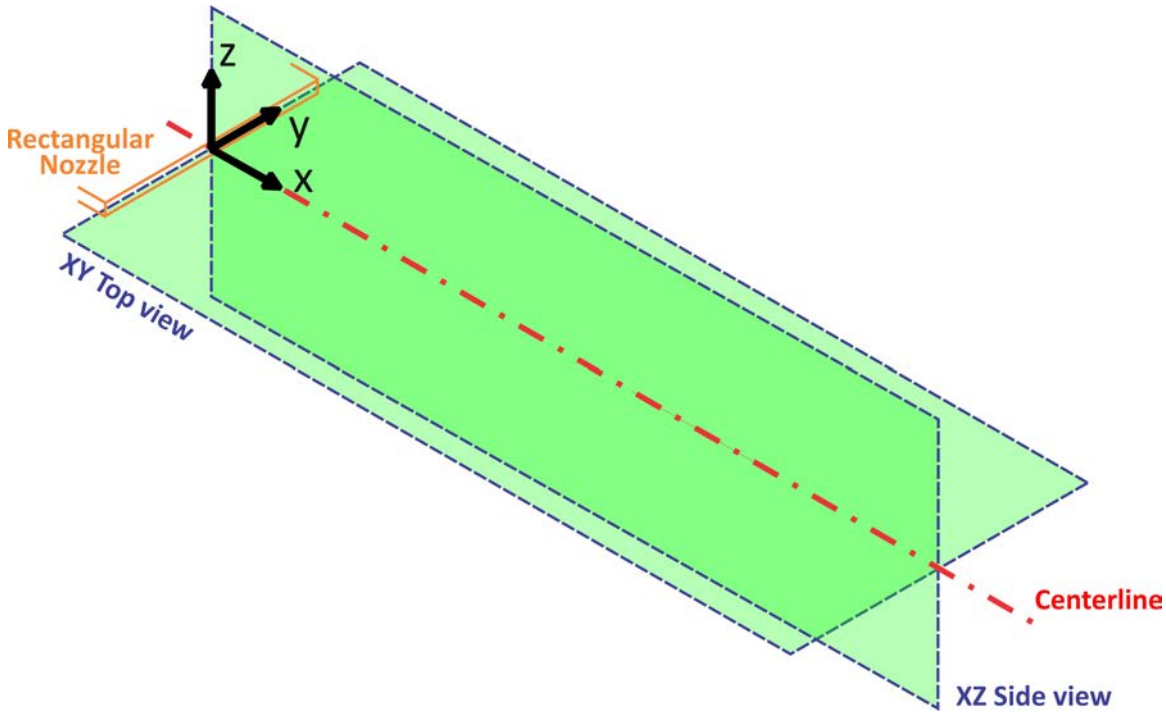

Figure 2.4: Visualized planes by PIV laser sheet.

The experiment setup for measuring the pressure of a high-aspect-ratio rectangular jet controlled by a Plasma Actuator involves using a Pitot tube with a differential pressure sensor to measure the total pressure. The differential pressure sensor (OMRON D6F-PH0505AD4) is used to measure this pressure difference, and it has a range of ±50 Pa and a precision of ±3% RD. This allows for accurate and precise measurements of the pressure of the fluid. The sampling rate for the differential pressure sensor is 20 Hz, which means that

it takes a measurement every 1/20th of a second. A total of 600 samples are taken per point over 30 seconds, giving a comprehensive picture of the pressure of the fluid over time.

The flow visualization system contained a laser sheet (G100, KATOKOKEN CO 100 MW) to visualize the flow, a smoke generator (PS-2006, DAINICHI) to inject seeding particles into the flow, and a high-speed camera (Phantom V711 by Vision Research Inc.) to record a video for analysis. The laser sheet illuminated these particles at the X-Y Top View and X–Z Side View planes, as shown in Fig. 2.4. Then, the videos recorded at 2000 fps for 5 s were analyzed using PIVlab software embedded in MATLAB by Thielicke *et al.* [52].

Table 2.1: List of main experimental equipment.

Category	Name	Model and Manufacturer	Description
Flow	Wind tunnel	WGT-10, Tsukubarika Seiki Co., Ltd, Japan"	Generating the flow for the test
Velocity	Hot-wire MiniCTA	54T42, Dantec Dynamics	Measuring the velocity of the flow in high-frequency and high-precision
	X-wire hot-wire probe	55P61, Dantec Dynamics	Sensor that can measure U-component and V-component velocity
	Probe support	55H25, Dantec Dynamics	Support for the hot-wire sensor
Temperature	Thermocouple	TCTG022, MISUMI	Sensor to measure temperature
	Data logger	LR8450, Hioki	Log the data from thermocouples
	Ceramic heater	MCHNN2, MISUMI	Heater to heat up the encloser chamber
	PID controller	E5EC, OMRON	Control the temperature of the encloser chamber to desired temperature
	Solid-state relay	G3PJ, OMRON	Actuator for control the heaters
	Circulatory chiller	CF800, YAMATO SCIENCE	Cool the air feeding to the wind tunnel
Pressure	MEMS Differential pressure sensor	6F-PH0505AD4, OMRON	Sensor to measure the pressure
Data acquisition	Multi-function I/O DAQ device	PCI-6133, National Instruments	Input data from sensors, output data for actuators flowing to experimental plan

Table 2.2: List of main experimental equipment (continued).

Category	Name	Model and Manufacturer	Description
Transverse system	Micro-controller	Arduino UNO, Arduino	Receive the command from the PC to control the transverse system
	Stepper motor	PKP268D28A-L, Oriental Motor	Actuator operate the transverse system to move the probe to desired location
	Stepper motor driver	CVD228-K, Oriental Motor	Driver to precisely control the stepper motors
	XYZ linear bearing frame		Mechanical assembly for supporting for the transverse system
Visualization	PIV laser sheet	G100, KATOKOKEN CO	Laser sheet used to light up the seeding particle
	Smoke generator	PS-2006, DAINICHI	Generating the seeding particle into the flow
	High-speed camera	Phantom V711, Vision Research Inc.	Record the flow visualization in high-speed
Plasma Actuator	Plasma power supply	PSI-PA1050N, PSI Co., Ltd	Generating the plasma controlling signal which is high-voltage high-frequency AC
Software	Programming environment	MATLAB, MathWorks	Software and programming language use to automatically implement the experimental plan

Tables 2.1 and 2.2 shows the experimental equipment to clearly and concisely present the specific details and information about the various equipment used in HAR rectangular jet controlled by Plasma Actuator experiment. This includes the category of the equipment, the name of the equipment, the model and manufacturer, and a description of the equipment's function and usage. Having this information organized in a table format allows for easy reference and understanding of the experimental setup and the role of each piece of equipment. Additionally, having a table to present this information can aid in the replication of the experiment, as well as in the maintenance and troubleshooting of the equipment.

In conducting the experiments, a significant effort was made to capture a wide range of data to achieve accurate and reliable results. This involved measuring various parameters such as velocity, temperature, vorticity, integral length scale, and so on using advanced techniques. Additionally, visualization techniques, such as using a PIV laser sheet, provided clear flow flied pictures for further analysis. By implementing this comprehensive set of measures, the experiments gathered a wide range of data that helped support the research and conclusions drawn. Overall, the combination of various measurements and visualization techniques allowed us to understand the phenomena under this research comprehensively.

2.1.2 High-aspect-ratio Rectangular Jet Controlled by Plasma Actuators Experiment Setup

The structure of the single DBD plasma actuator is shown in Fig. 2.5. The working condition of Plasma Actuator and the dimension of the device were referred to Plasma Actuator design guideline by Grosse *et al.* [53] and refer to well-established research using Plasma Actuator for AFC control [48] [54] [55] [56]. The parameters for design consideration are shown in Table 2.3. At first, the design was chosen as the straight bar for simplicity and uniformity of the velocity distribution along the spanwise direction. The velocity has the most substantial effect on the thrust generation and power consumption; it is advisable to pre-determine the operating voltage. Therefore, V_{pp} = 6 kV at the base frequency is f_b = 15 kHz was chosen to control the flow because this voltage was proved it could have enough thrust power to perform AFC control for HAR rectangular jet according to [48]. Next, other parameters of the structure of the PA as the dielectric layer thickness, negative inter-electrode gap, and narrow and thin exposed electrodes, were selected based on the design guidelines. A thin dielectric layer of low-permittivity (polyamide tape, $t = 80$ μm), short or minus-electrode gap (g = -1 mm, the negative number means overlap inter-electrode gap), and narrow and thin exposed electrode ($h1 = h2 = 70$ μm) were used to

archive the best thrust. Based on the constraint of the HAR nozzle design, the spanwise length of the PA L was chosen to be equaled the length of the nozzle as 150 mm. About the width of the cover electrode, there is no influence on the performance of the Plasma Actuator. However, it is known that a thin and narrow covered electrode can constrain the extent of generated plasma and reduce the thrust. Therefore, the width $w_2 = 4$ mm was chosen that was longer than the reach of plasma at the given working condition by conducting experiment. The width $w_1 = 2$ mm of the exposed electrode was chosen to match the cover electrode-based Plasma Actuator scale in the design guideline. After that, Two PAs were constructed on the tip of the nozzle. The actuator was composed of an exposed electrode, an electrode covered in copper, and two layers of dielectric material made of polyamide.

Table 2.3: Typical DBD Plasma Actuator design parameter.

Parameter	Symbol (units)
Exposed electrode width	w_1 (mm)
Encapsulated electrode width	w_2 (mm)
Inter-electrode gap	g (mm)
Exposed electrode height	h_1 (μm)
Encapsulated electrode height	h_2 (μm)
Dielectric layer thickness	t (mm)
Permittivity of the dielectric	ϵ_r
Applied voltage	Vpp (kV)
Signal frequency	f_b (kHz)

The technique for constructing a DBD PA refers to the procedure to make the PA described by Fukagata *et al.* [57].

- Cut copper adhesive tape to the designed width and length and paste it onto the edge of Part a ; this becomes the copper-covered electrode. Then, cut the polyamide adhesive tape and attach it next to the copper-covered electrode to complete the first layer.

- Take two layers of polyamide tape and paste them on top of the first layer

to create the dielectric layers. These become the second and third layers of the PA.

- Cut copper adhesive tape to the width and length of the exposed electrode and paste it on top of the third layer at the designed position.

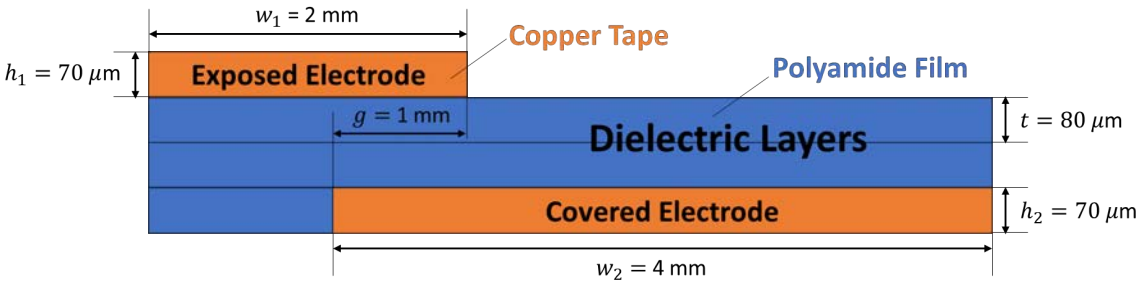

Figure 2.5: Single DBD plasma actuator configuration.

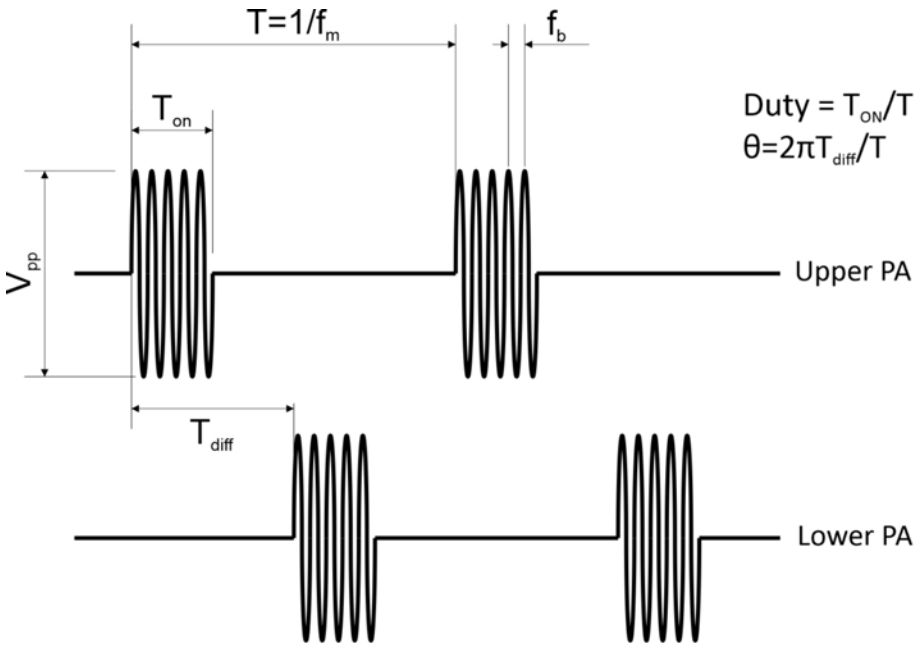

Figure 2.6: High-voltage high-frequency pulse-width modulation sinusoidal Wave. The signal is amplified by the high voltage plasma power supply. Whereas: Vpp—peak to peak voltage, T_{ON}—ON time of plasma actuator, T—time per phase, $Duty$—Duty of the PWN signal, f_b—base frequency generated by the plasma power supply, f_m—modular frequency, T_{diff}—Time difference between the upper PA and lower PA signal, θ—Phase difference between the upper PA and lower PA signal.

The PAs were driven by a high-voltage, high-frequency power supply (PSI-PA1050N, PSI Co., Ltd). The multi-function I/O device (National Instruments PCI-6133) generated a pulse-width modulation signal with a duty cycle ranging from 0% to 100% to control the plasma power supply to generate a high-voltage, high-frequency, pulse-width modulation sinusoidal wave as can be seen in Fig. 2.6. An oscilloscope was utilized to monitor the signal for precise adjustment of the PA working condition determined by the following parameters: V_{pp}, f_b,

f_m, and θ as the peak-to-peak voltage, base frequency, modular frequency, and phase difference between the upper and lower PAs, respectively. The phase difference between the upper and lower PAs determined the operating time between the two PAs; θ values of zero and π mean that the two PAs were operating simultaneously and alternately, respectively. Details of the experimental conditions are listed in Table 2.4.

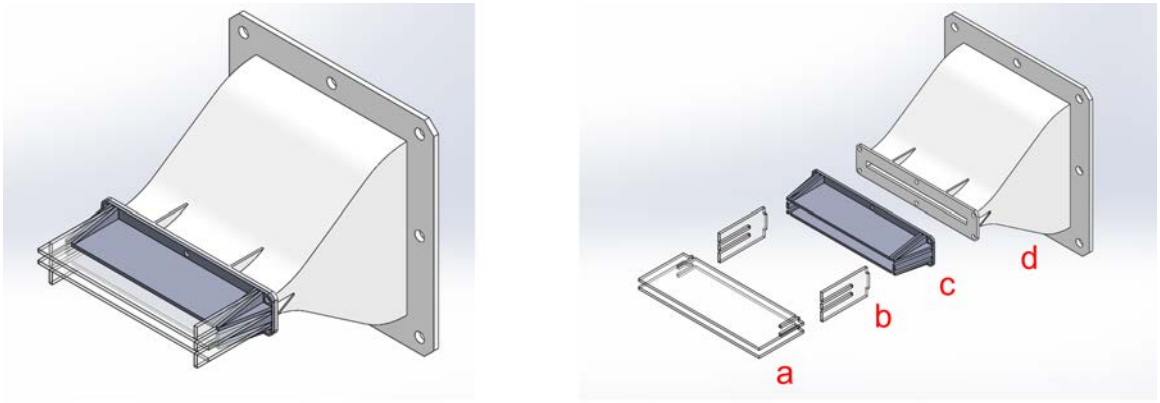

Figure 2.7: 3D design of rectangular nozzle (7.5 mm $\times$ 150 mm) AR = 20 assembly with plasma actuators. Parts (a), (b), (c), and (d) to construct the assembly are indicated in the right-side exploded view.

Figure 2.8: Parts (**a**) and (**b**) to construct the nozzle outlet.

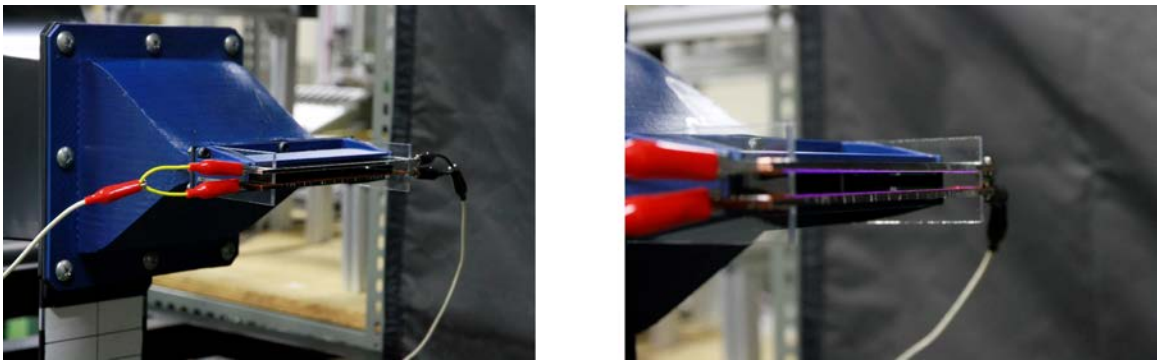

Figure 2.9: Full installation of an operating nozzle and plasma actuators onto the wind tunnel.

A 3D model of an adapter was printed using the 3D printer AirWolf AXIOM Dual extruders to constrain the flow from the wind tunnel outlet to the rectangular jet outlet (Fig. 2.7). A scale of 101% to tackle the problem of ABS shrinkage was sufficient to produce appropriate nozzles. The nozzle interior was

sanded with 120, 200, 400, and 800 sandpapers. Subsequently, the painting process of filler primer, spot putty, and painting was used to achieve a smooth inner surface inside the adapter with a surface roughness of approximately 11 $\pm$ 1 μmm. The nozzle assembly is constructed using four components. Parts (a) and (b) (Fig. 2.8) were laser-cut from an acrylic board to obtain the designed shape; subsequently, PAs were attached to the surface of the parts (a) facing inside the nozzle; parts (c) and (d) indicated in Fig. 2.7 were made using a 3D printer from ABS to complete the nozzle assembly. A HAR rectangular nozzle with plasma actuator assembly is shown in Fig. 2.9. High-frequency, high-voltage signals were fed to the two plasma actuators located on the tips of the nozzle with the settings mentioned in the single DBD plasma actuator experiment (Fig. 2.6).

Table 2.4: Details of velocity and temperature experiment conditions for testing the effect of plasma actuators on the rectangular jet.

Symbol	**Description**	**Value**	**Unit**
B	Nozzle width	150	mm
h	Nozzle height	7.5	mm
U_0	Outlet velocity	4.5	m/s
T_a	Controlled ambient temperature (average)	40	°C
T_0	Controlled nozzle temperature (average)	12	°C
V_{pp}	Peak-to-peak voltage	6	kV
f_b	Base frequency	15	kHz
f_m	Modular frequency voltage	0–1000, 50 each step	Hz
$duty$	Duty of PA controlling signal	0–1, 0.1 each step	
θ	Phase difference between upper and lower PA	0 and π	

Details of the experimental conditions are listed in Table 2.4. The experiment was designed to simulate the situation when leaving a car under the sun for 30 minutes as the temperature inside the car reaching $T_a = 40$°C and the A/C system operating at maximum power $T_0 = 12$°C. The effect of the plasma actuator on the HAR rectangular jet was examined by changing three key pa-

rameters: modular frequency (0 Hz, 50 Hz, 100 Hz,..., 1000 Hz), duty cycle (0, 0.1, 0.2,..., 1), and θ (0 and π). Consequently, changing these parameters yielded 362 working conditions for the plasma actuator. A point in the centerline x = 525 mm (x/h = 70) in the fully developed region was chosen to observe the velocity and temperature performance of the jet under different PA working conditions. This location was selected because it is where the driver is in the automobile; the flow velocity and temperature at this location are crucial for the thermal comfort of the driver and passengers. Higher velocity and lower absolute temperature are preferable for the automobile air-conditioning application at locations far from the outlet. The procedures used to evaluate the effect of plasma actuators on rectangular jets for both velocity and temperature are identical. First, on the centerline of the jet where x/h = 70, the hot-wire probe for measuring the velocity and the thermocouple array for measuring the temperature were positioned. Then, the velocity and temperature data were obtained after changing the multiple PA working conditions. After obtaining the data, exceptional cases were selected based on the values of the data (higher than average and lower than average velocities and temperature). The centerline velocity, centerline temperature, and cut section temperature were measured for these cases to examine the effect of the plasma actuator on the rectangular jet in detail. The normalized temperature τ_{xyz} was used to

evaluate all the temperature results between all measurement points as:

$$\tau_{xyz} = \frac{T_{xyz} - T_a}{T_0 - T_a} \tag{2.1}$$

where T_{xyz} is the temperature measured at a point in space, T_a is the ambient temperature inside the temperature-controlled chamber, and T_0 is the temperature at the outlet of the nozzle, where (x_0, y_0, z_0) = (0,0,0). Looking at Equation (2.1), the normalized temperature is inversely proportional to the absolute temperature. Starting from this point of the manuscript, "increase the temperature" means "increase the normalized temperature" and vice versa.

2.2 Plasma Actuator Effect on High Aspect Ratio Rectangular Jet Velocity

The operating images of the nozzle with the PA are shown in Fig. 2.10 with the ON and OFF events. Kelvin–Helmholtz instability vortexes were observed as in the base case. These vortexes, known as initial vortexes, break down at the end of the potential core region. As shown in the Fig., the PAs can actively control the flow by generating pair of spanwise vortexes when the PA is operating during "ON" events. When compared to the base case, it can be observed

that the periodic “pumping” effect on the airflow as the modular frequency f_m with duty is applied to the PAs. The width of the jet changed when the plasma actuator was ON and operated under different working conditions. These actuators can overdrive the natural vortex generation frequency of the rectangular jets. The PA working condition once again determines the size of the vortex ring generated by the PA.

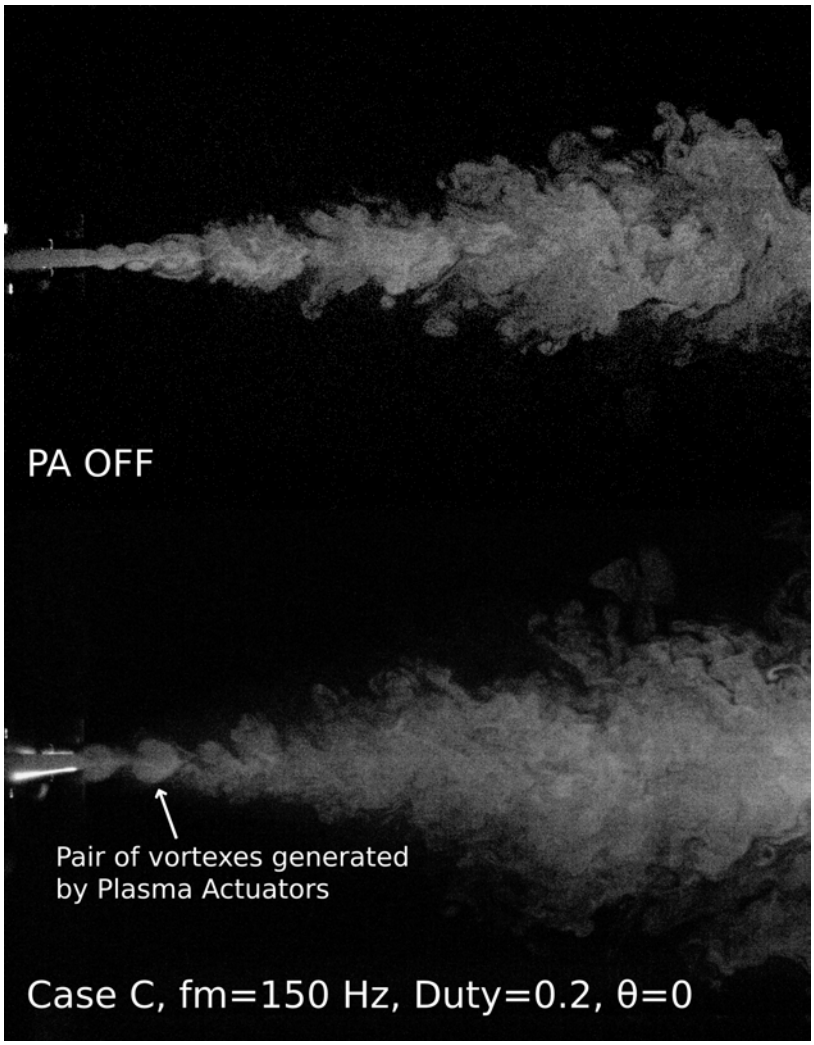

Figure 2.10: Images of flow visualized by PIV laser sheet and high-speed camera (Side view).

Figure 2.11 shows velocity distribution along the y and z axes at different locations to give an overview of the base case. It also verifies that the laboratory coordination established by the transverse system corresponds with the rectangular jet coordination system. Velocity measurements were conducted at

x/h = 70 under various working conditions of the plasma actuator. For a better comparison between a large number of cases, the surface plot and heat scatter plot results using the same set of data (velocity vs. modular frequency vs. duty) for θ = 0 and θ = π are shown in Fig.s 2.12 and 2.13, respectively. These plots confirm that the plasma actuator modifies the velocity at the measured point. Although θ = 0 can both increase and decrease the velocity, θ = π only shows a tendency to reduce the velocity. There is a clear tendency when θ = 0; when f_m is in the range of 50–200 Hz, PAs improve the velocity compared with the base case with PAs turning off. At the measuring point where x/h = 70, the velocity was 4% higher (Case A) and 11% lower (Case B) across all tested cases than in the base case. In contrast, when θ = π, a significant decrease in velocity can be seen in the same area where the velocity is increased when θ = 0 (from f_m = 50–200). Another point from this graph is that the modular frequency substantially affects the velocity more than the duty cycle in both major cases. For example, when f_m = 500 Hz and θ = π, changing the duty from 0.1 to 0.9 yields almost the same color on the heat scatter plot.

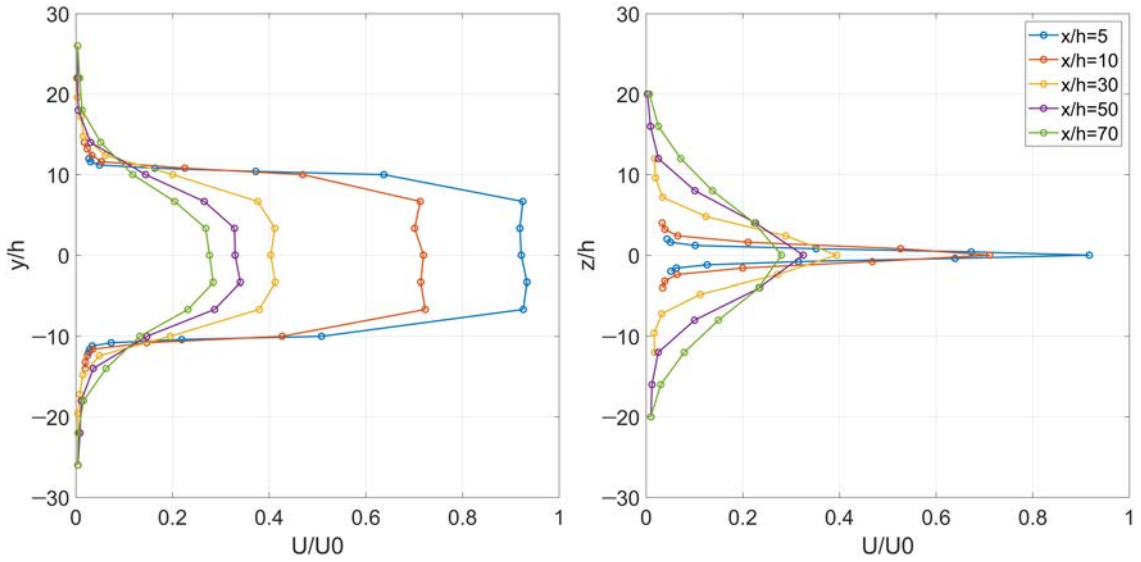

Figure 2.11: Velocity profiles along the y and z axes at different locations.

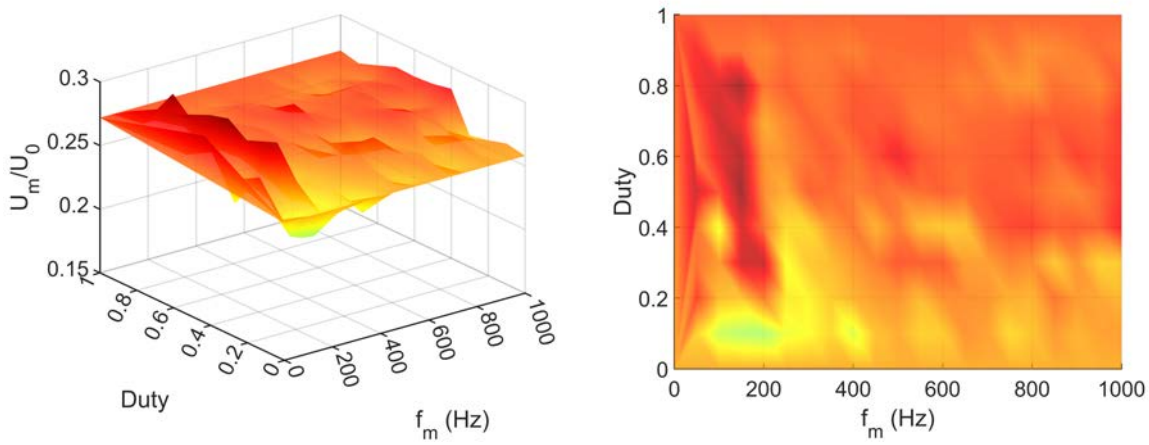

Figure 2.12: Surface plot and heat scatter plot (f_m vs. $duty$ vs. $velocity$) while $\theta = 0$ at centerline where x/h = 70.

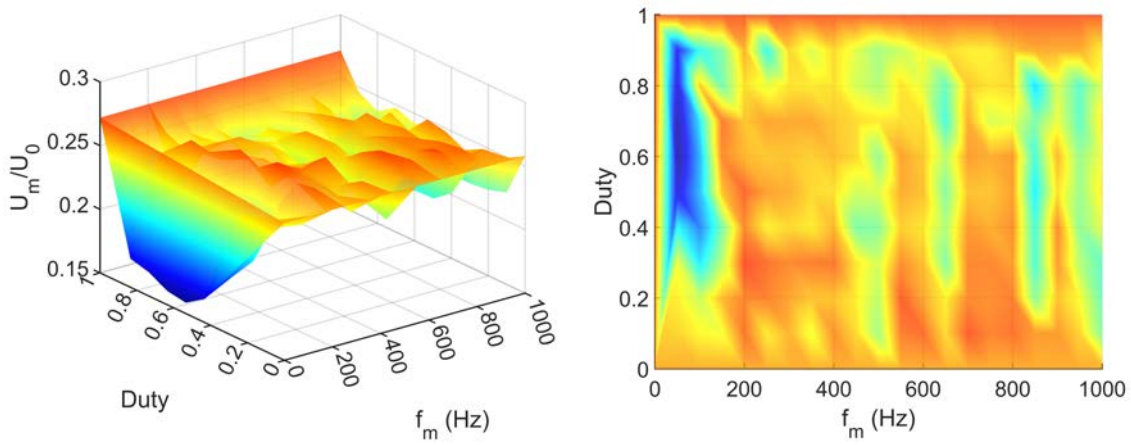

Figure 2.13: Surface plot and heat scatter plot (f_m vs. $duty$ vs. $velocity$) while $\theta = \pi$ at centerline where x/h = 70.

For further examination, two cases with the most significant effect on rectangular jet flow were selected. One case had a high-velocity performance when θ = 0, and the other had a low-velocity performance when θ = π was measured to acquire the centerline velocity. For cases where the plasma actuator was operating, the measurements started at x/h = 5 to maintain a safe distance from the plasma to protect the measuring equipment. The two cases are: case A—f_m = 150 Hz, $duty$ = 0.5, θ = 0, and case B—f_m = 50 Hz, $duty$ = 0.7, θ = π; the details are listed in Table 2.5.

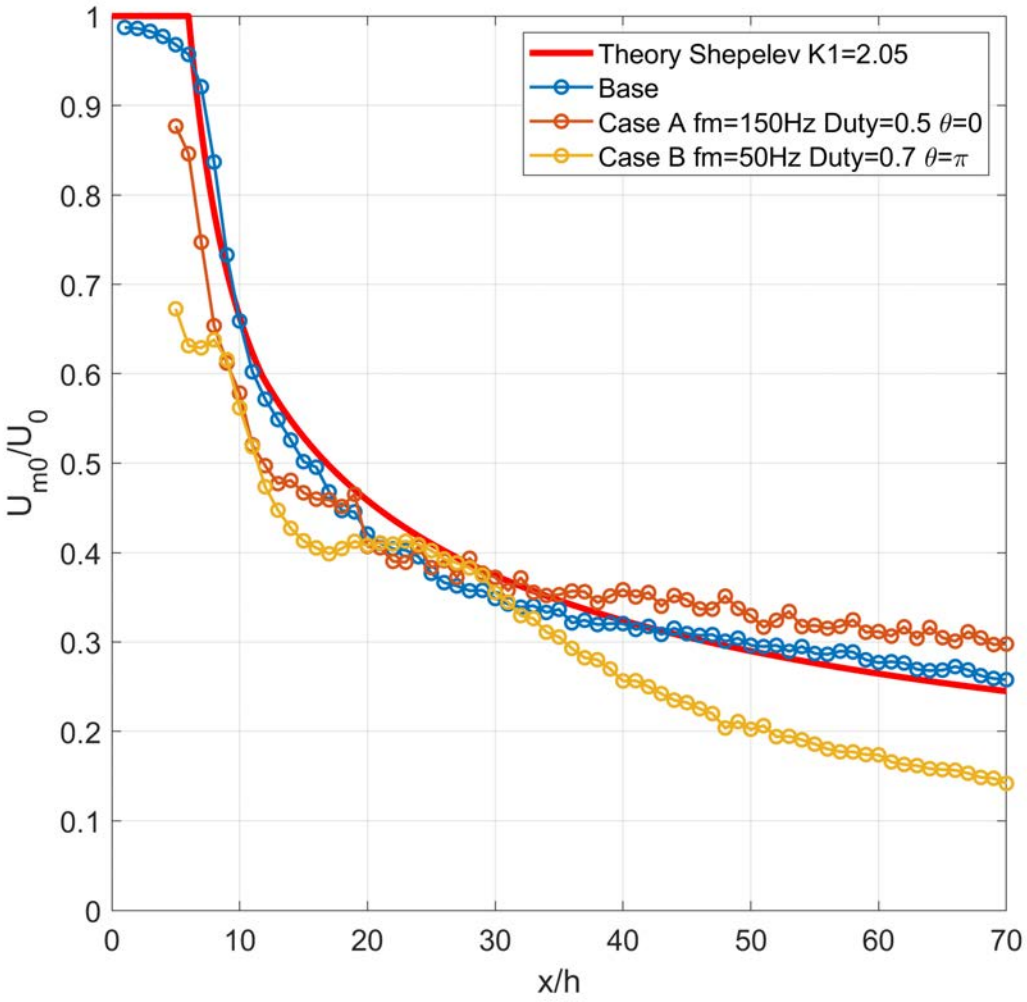

Figure 2.14: Comparison between centerline velocities of different cases.

Table 2.5: Denoted cases regarding Modular Frequency, Duty, and Phase Difference.

No.	Case name	Description	f_m (Hz)	$Duty$	θ	Δ_U[1](%)	Δ_τ[2](%)
1	Base	Base case	-	-	-	-	-
2	Case A	High Velocity	150	0.5	0	15.47	-
3	Case B	Low Velocity	50	0.7	π	-44.98	-
4	Case C	High Normalized Temp.	150	0.2	0	-	13.68
5	Case D	Low Normalized Temp.	450	0.8	0	-	-14.91
6	Case E	Low Normalized Temp.	100	0.4	π	-	-17.38
7	Case F	High Normalized Temp.	500	0.1	π	-	10.44

The velocity decay of the jet centerline in this zone can be calculated using Equation 1.4 repeated here as Equation 2.2. The centerline velocity compared with the theoretical and base cases are illustrated in Fig. 2.14. K_1 is an empirical constant derived from centerline experiment data. Similar work to find K_1 can be obtained from the work of Shepelev [16], Gortler and Tollmein [17], Heskestad [18], and Kotsovinos [19]. In this study, K_1 = 2.05 was found using the least square method to fit the model with experimental data. The equations for the velocity used in the centerline velocity equation assume that the jet is supplied from a virtual origin. The addition of the term, x_0, to the distance from

[1] Δ_U – Velocity increment compared with base case in % at x/h = 70;
[2] Δ_τ – Normalized temperature increment compared with base case in % at x/h = 70.

the outlet corrects the influence of the outlet size on the jet geometry. However, as reported by Goodfellow [58], it can be neglected by many researchers for practical use in experimental comparisons.

$$\frac{U_{m0}}{U_0} = K_1\sqrt{\frac{h}{x}}, \tag{2.2}$$

where,

U_{m0}—Centerline velocity at x;

U_0—Average velocity at outlet where (x_0, y_0, z_0) = (0,0,0);

h—Height of rectangular nozzle; and

K_1—Centerline velocity decay constant.

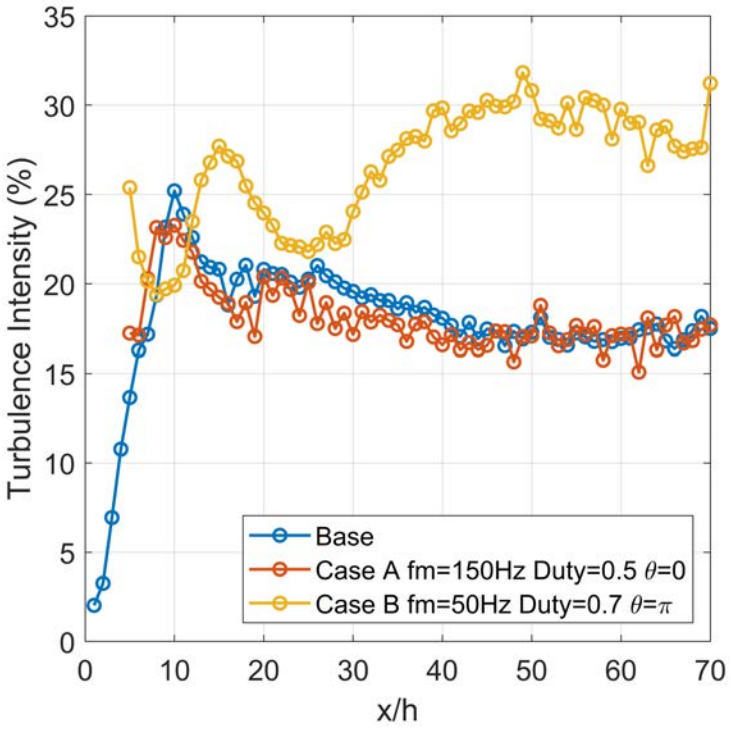

Figure 2.15: Comparison of centerline turbulence intensity between cases.

From x/h = 0 to x/h = 30, these cases perform worse than the base case with a shorter potential core; in particular, for case B, the normalized velocity at this point is 30% less than that of the base case. After x/h = 30, case A performed better, resulting in an increased offset velocity profile from the base case, and case B vastly decreased compared with the base case. Fig. 2.15 shows the turbulence intensity along the centerline. The turbulence intensity is related to the mixing phenomena in the flow. As seen from the base case, the

maximum mixing on the centerline happened at x/h = 10, and the intensity gradually decreased and stabilized at 16%. Case A turbulence intensity peaked at the exact location as the base case. After that, the profile trended similarly to the base case when PAs were off. In contrast, the evolution of turbulence intensity profile changed entirely when PAs operated at phase difference in case B. While other cases got their peaks turbulence intensity, case B got its low. After x/h = 30, the turbulence intensity increased rapidly, whereas the other cases decreased and then reached the maximum turbulence intensity at 30%. As a result, PAs can introduce turbulence intensity to the flow when working in the phase difference mode at a particular frequency.

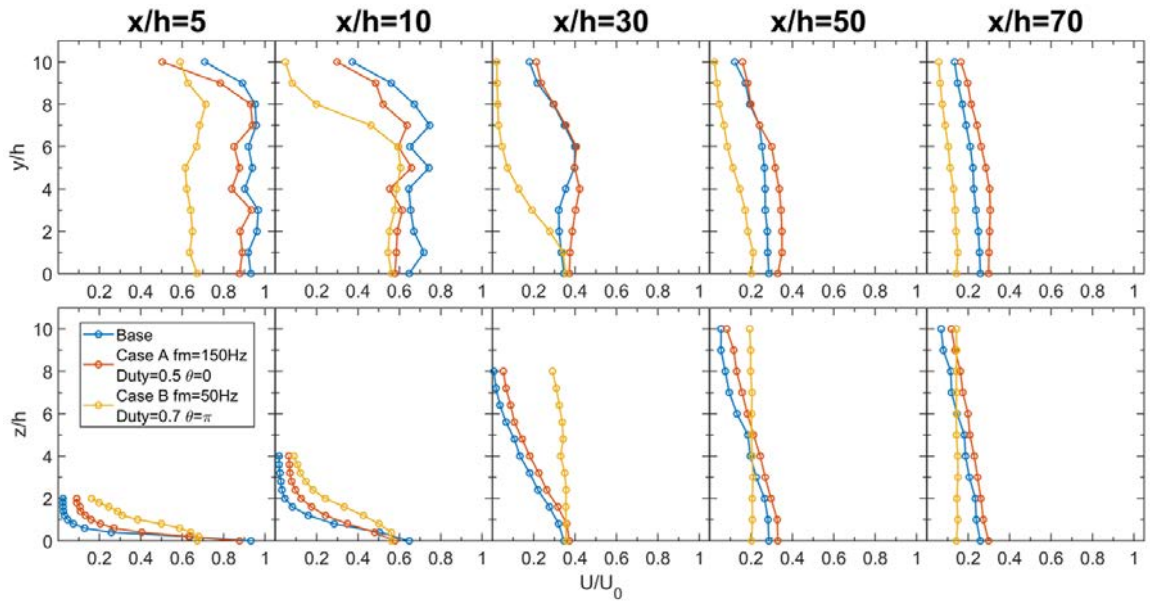

Figure 2.16: Velocity distribution along the *oy* and *oz* directions at different locations.

Plasma Actuators can influence the distribution in the *oy* and *oz* direction, as shown in Fig. 2.16. In case A, velocity profiles along the z-axis were improved at all measured locations; the *y* profiles were decreased at x/h equaled 5 and 10 and had positive offsets at x/h = 30, 50, and 70. In the case of B, the velocity profiles in the *z*-direction performed better than other cases from x/h = 5, 10, and 30, whereas the profiles in the *y*-direction performed worse than others. The jet width was expanded in the oz direction and constrained in the *oy* direction, indicating the conversion of kinetic energy from one direction to the other. The cross-section of a rectangular jet evolves downstream with its major

and minor axis rotated at angles compared to jet geometry. This phenomenon is called axis-switching. Consequently, plasma actuators operating at different conditions can change the profile to increase or decrease the centerline velocity of HAR rectangular jets.

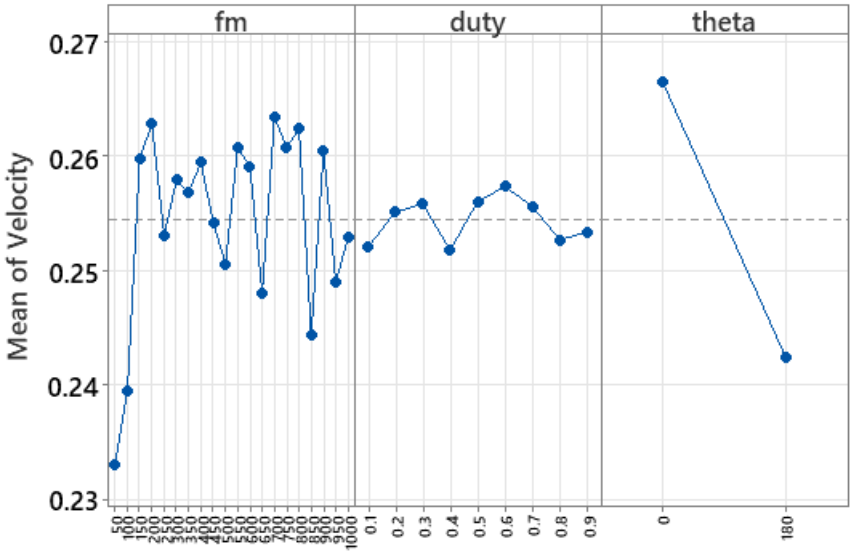

Figure 2.17: Main effects for velocity at x/h = 70.

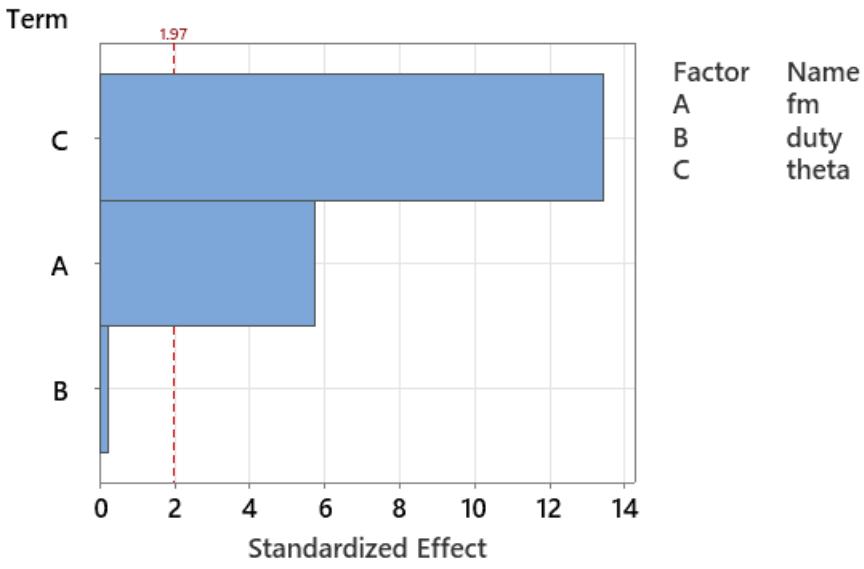

Figure 2.18: Pareto chart for velocity at x/h = 70.

Identifying the most critical operating parameters of plasma actuators is crucial for optimizing the velocity performance when controlling HAR rectangular jet. Full fractional designs are an effective method for identifying these critical operating parameters because they allow for estimating all factors' main effects and interaction effects by utilizing the velocity screening data. In a full fractional design, all possible combinations of the operating parameters are tested; then, a comprehensive understanding of how each parameter impacts the performance of the plasma actuator can be obtained. Figure 2.17 illustrates the main effects of different parameters for the velocity at x/h = 70.

Also, Fig. 2.18 shows the Pareto chart to summarize the analysis result: the phase difference (theta) is the most critical parameter that can affect the velocity at the driver's location; in contrast, the effect caused by duty is tiny. Since the phase difference θ only has two levels as 0 and π, hence, changing modular frequency f_m is the main parameter for optimizing the velocity.

2.3 Plasma Actuator Effect on High Aspect Ratio Rectangular Jet Temperature

The scanning method was also applied for temperature evaluation using the same logic as velocity analysis. The uncertainty of a temperature measurement equaled the measurement precision of the T-thermocouple as $\pm 0.75\%$. Accordingly to Eq.2.1, the total uncertainty was calculated as about $\pm 7.3\%$ for normalized temperature data at x/h = 70. The surface plot and heat scatter plot results using the same set of data (normalized temperature vs. modular frequency vs. duty) for θ = 0 and $\theta = \pi$ are shown in Fig. 2.19 and 2.20, respectively. Even though the same scanning method was used for temperature and velocity measured at the same point on the centerline where x/h = 70, there

was no correlation between these surface plots and contour plots for velocity and temperature. In this context, duty seems to have a more substantial influence on the temperature than the modular frequency f_m, unlike the previous velocity analysis. The duty from 0.1 to 0.5 generally results in better temperature, and having a duty from 0.6 to 0.9 has the opposite effect.

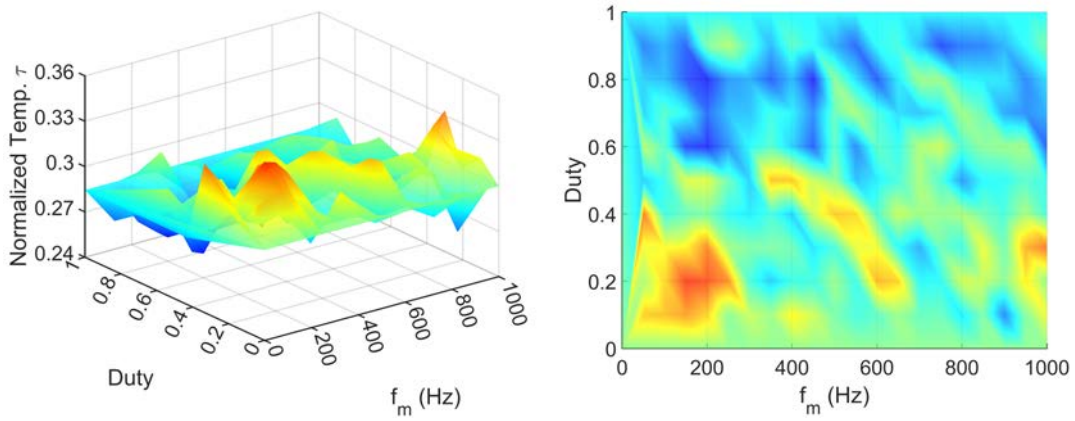

Figure 2.19: Surface plot and heat scatter plot (f_m vs. $duty$ vs. Normalized Temperature) while $\theta = 0$ at centerline where x/h = 70.

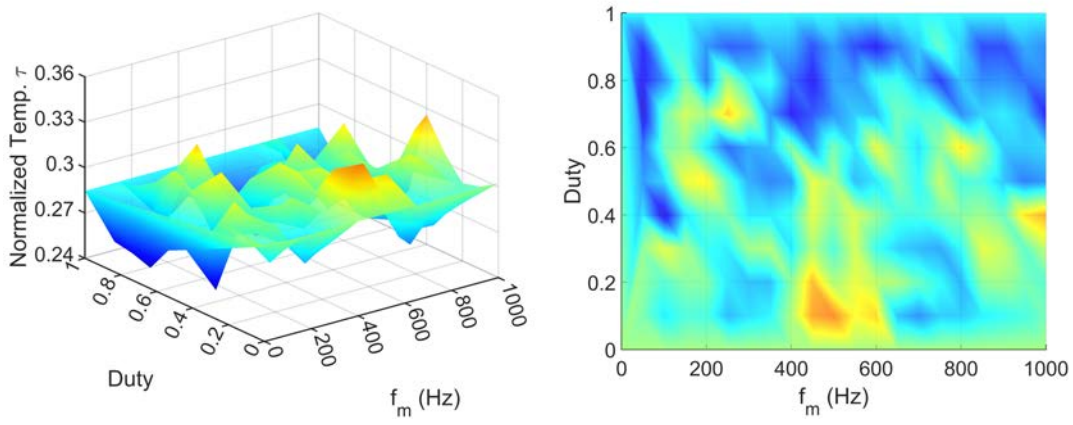

Figure 2.20: Surface plot and heat scatter plot (f_m vs. $duty$ vs. Normalized Temperature) while $\theta = \pi$ at centerline where x/h = 70.

Four cases were chosen for further examinations: two cases (C and D) with a high and low temperature performance while θ = 0, and another two cases (E and F) while θ = π all compared to the base case. The details of these cases are listed in Table 2.5. The temperature contour plots on the *xz* cut section where y/h = 0 in these cases are illustrated in Fig. 2.21. The theoretical distribution was calculated based on Shepelev [59] and Goodfellow [58]. It can be done by curve fitting the experimental data to find the empirical constant c = 0.1253 and then computing the velocity using Equation (2.3) to yield the temperature at any given point in space using Equation (2.4). In these two equations, the term "erf" represents the mathematical error function.

$$U_{xyz} = \frac{U_0}{\sqrt{2}} \sqrt{\operatorname{erf} \frac{B_0 - z}{cx} + \operatorname{erf} \frac{B_0 + z}{cx}}, \tag{2.3}$$

$$\begin{aligned} \frac{U_{xyz}(T_{xyz} - T_a)}{U_0(T_0 - T_a)} = \frac{1}{4} \left(\operatorname{erf} \sqrt{\frac{1+Pr}{2}} \frac{y + A_0}{cx} - \operatorname{erf} \sqrt{\frac{1+Pr}{2}} \frac{y - A_0}{cx} \right) \\ X \left(\operatorname{erf} \sqrt{\frac{1+Pr}{2}} \frac{z + B_0}{cx} - \operatorname{erf} \sqrt{\frac{1+Pr}{2}} \frac{z - B_0}{cx} \right), \end{aligned} \tag{2.4}$$

where,

U_{xyz}—Velocity at any given point in space with (x, y, z) coordinate;

U_0—Average velocity at outlet where (x_0, y_0, z_0) = (0,0,0);

T_{xyz}—Temperature at any given point in space with (x, y, z) coordinate;

T_a—Ambient temperature;

T_0—Average temperature at outlet where (x_0, y_0, z_0) = (0,0,0);

A_0—Half length of nozzle width;

B_0—Half length of nozzle height;

Pr—Prandtl number;

c—Empirical constant.

When comparing these cases with the theoretical and base cases, it can be

observed that the plasma actuator changes the temperature jet width and temperature distribution. In particular, the jet was spread in Case E. In the near outlet region, where x/h = 5 to 10, the jet has a wide distribution across the y-axis. From x/h = 20 to x/h = 40, the temperature distribution was denser than in the other cases, which means that most thermal interactions occurred in this general area. As a rule of thermal conservation, this intense thermal interaction creates a stronger mixing effect. This area mixed air at lower thermal energy with higher thermal energy. This resulted in a higher temperature near the outlet and a lower temperature in the far region after intensive mixing.

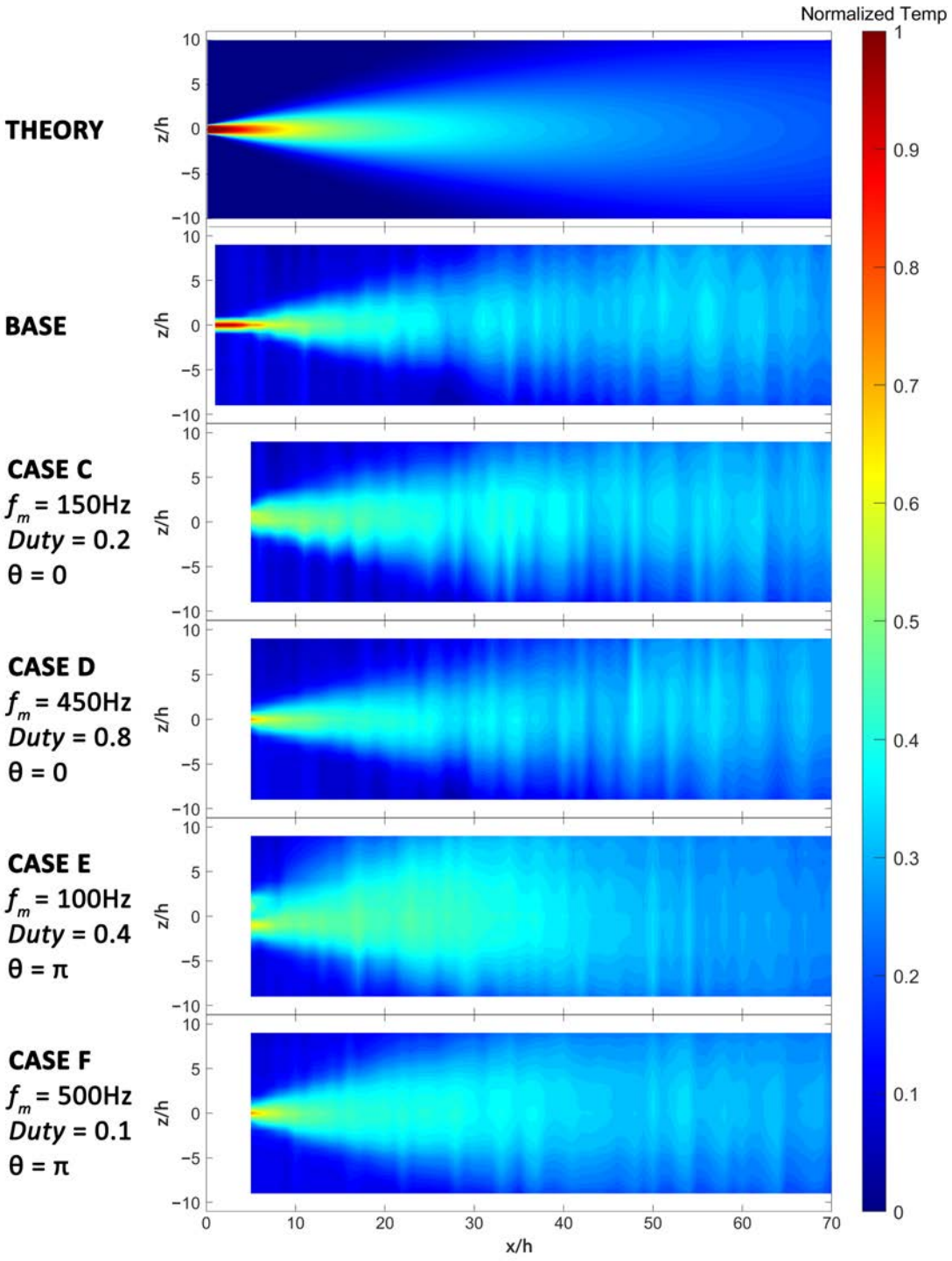

Figure 2.21: Normalized temperature contour plot on xz cut section where $y/h = 0$ for different cases.

For better visualization and comparison, the normalized centerline temperature for these cases and the theoretical distribution were extracted from the same data set, as shown in Fig. 2.22. It can be concluded that PAs also affect changing the temperature distribution in the xz plane and the yz cut sections. The diverging and converging jet width effects occur in all jet domains. Reasons for this phenomenon are out of this research's scope and will be further studied in future research. Furthermore, the axis-switching effect can be observed in case E, where x/h = 30, and the jet's axis is rotated by 90° compared with the theoretical and base-case temperatures. By combining Fig. 2.21 and 2.22, this general area where x/h = 20 to 40 has a high normalized temperature focused on a smaller area because of the earlier axis-switching effect.

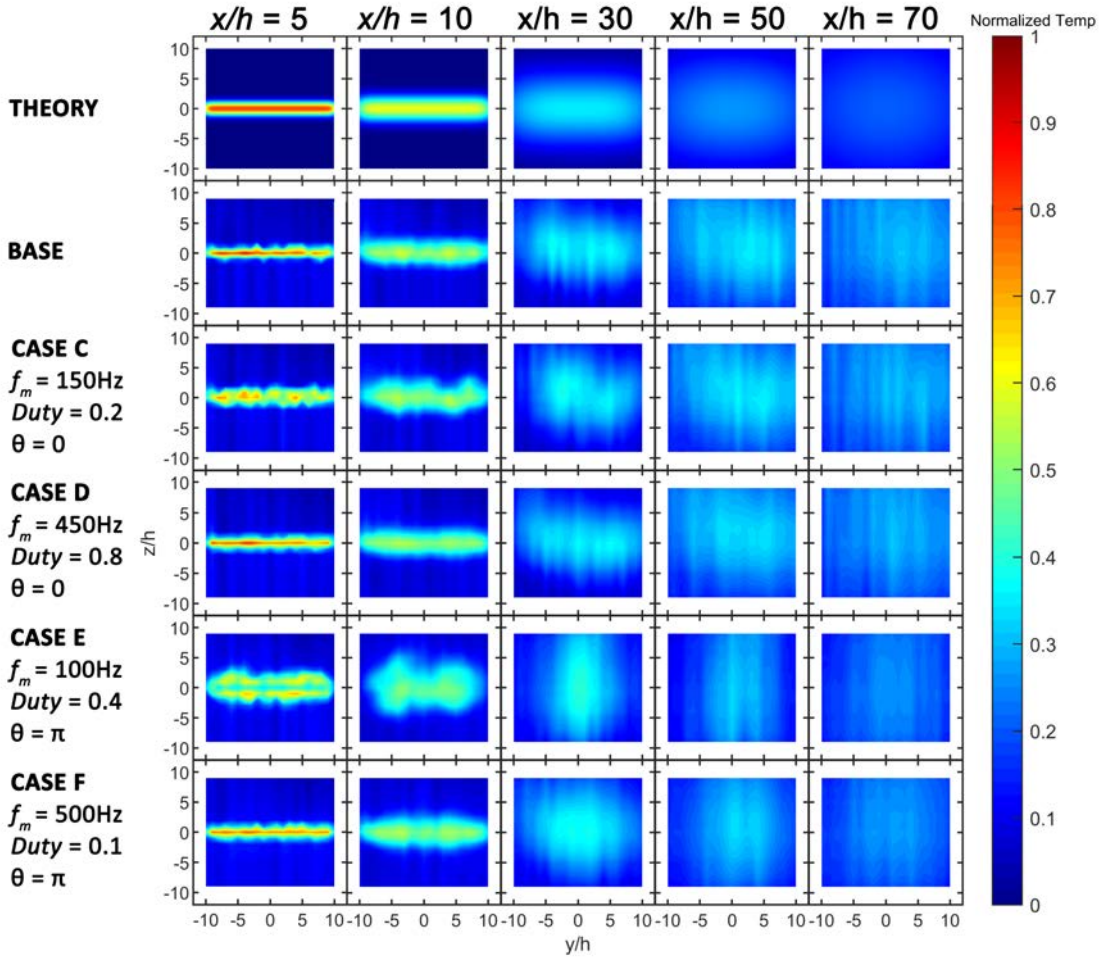

Figure 2.22: Normalized temperature contour plot on yz cut section where x/h = 5, 10, 30, 50, and 70 for different cases.

The centerline temperature is shown in Fig. 2.23. The temperature was normalized and compared with the theoretical work of Koestel [20] in Equation (2.5) and Abramovich [21] in Equation (2.6). Two empirical coefficients at

K_2 = 4.134 and a = 0.0988 were determined by fitting these models to the experimental data using the nonlinear least-squares method. Since there are fluctuations, all the experimental data were fitted by 4^{th} order Polynomial curve to show the trend and to compare the improvement among the cases. The fitting curves indicated well-matched profiles ($R^2 > 0.9$). After fitting, the improvement for normalized temperature for cases C and F are 18.20% and 13.02%, respectively, which indicates the temperature improvements are not outlier data points.

$$\tau_{m0} = \sqrt{0.83 K_2 \frac{h}{x}}, \tag{2.5}$$

$$\tau_{m0} = \frac{1.04}{\sqrt{\frac{ax}{B_0}} + 0.41}, \tag{2.6}$$

where,

τ_{m0}—Normalized centerline temperature at *x*;

B_0—Half length of nozzle height;

K_2—Centerline temperature decay constant [20];

a—Temperature decay constant [21].

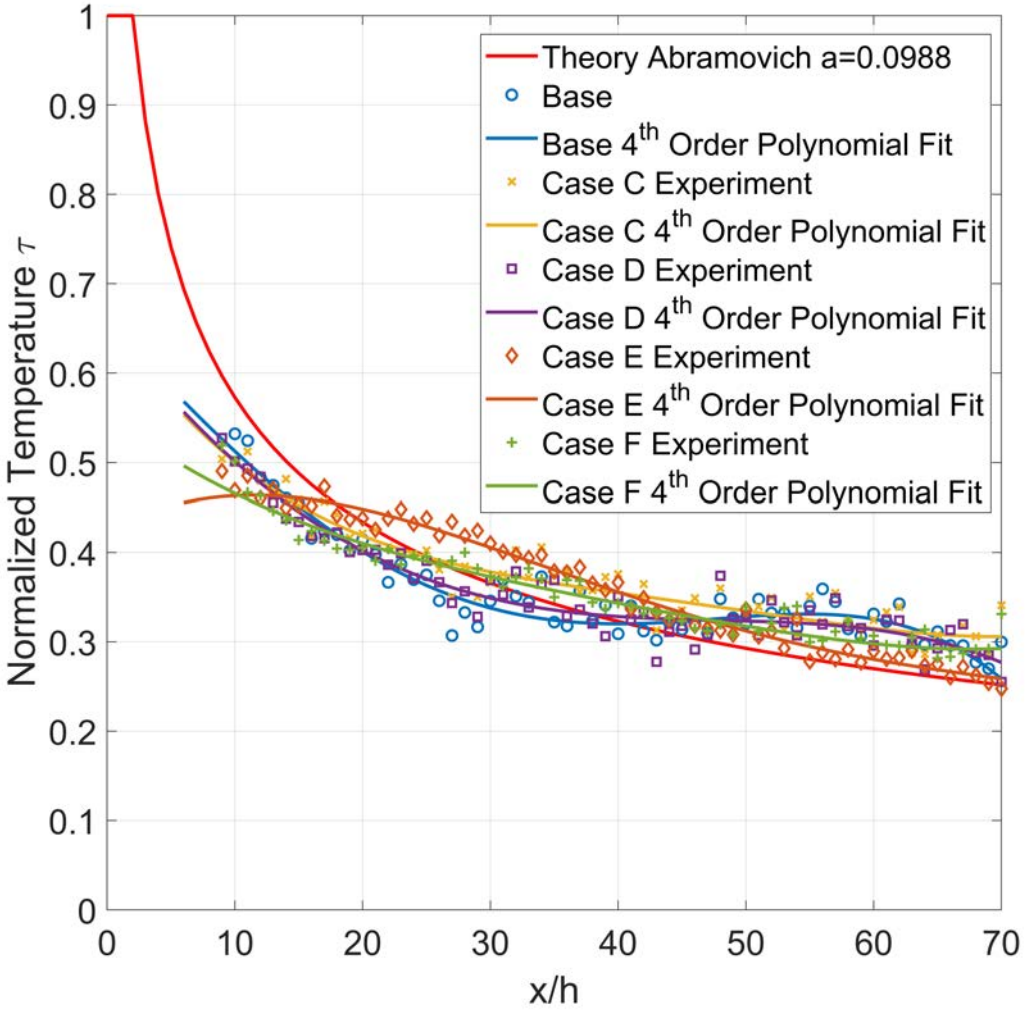

Figure 2.23: Comparison of centerline temperature between cases.

When applying the plasma actuator, the potential temperature core be-

comes shorter than the base case and decays faster. However, after the distance from the nozzle of x/h = 30, the temperature became higher than the base case. Furthermore, considering case E when f_m = 100 Hz, duty = 0.4, and $\theta = \pi$, in the region near the outlet $x/h < 20$, the centerline velocity performs worse than the base case. However, when it reaches the region $20 \leq x/h \leq 40$, there is a significant increment compared to the theory, base case, and other cases. This region is also where the axis-switching phenomena are described in the previous discussion.

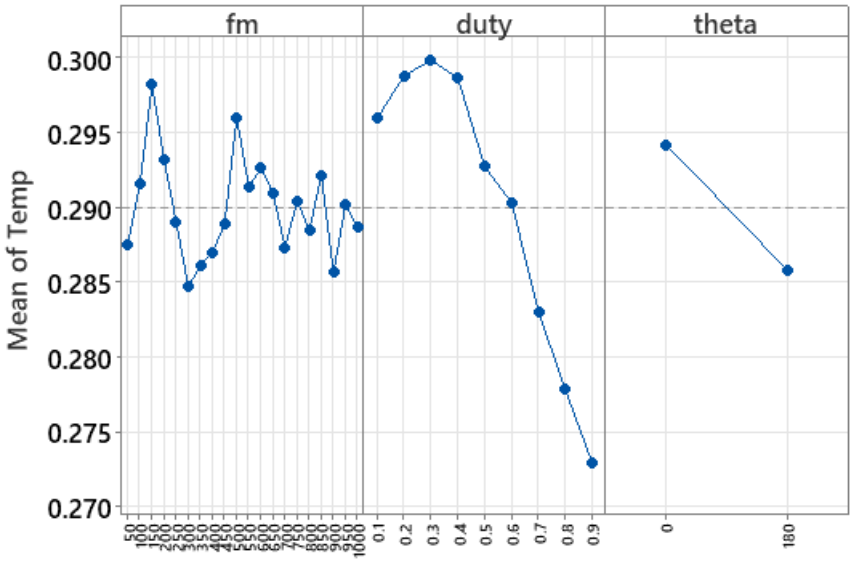

Figure 2.24: Main effects for velocity at x/h = 70.

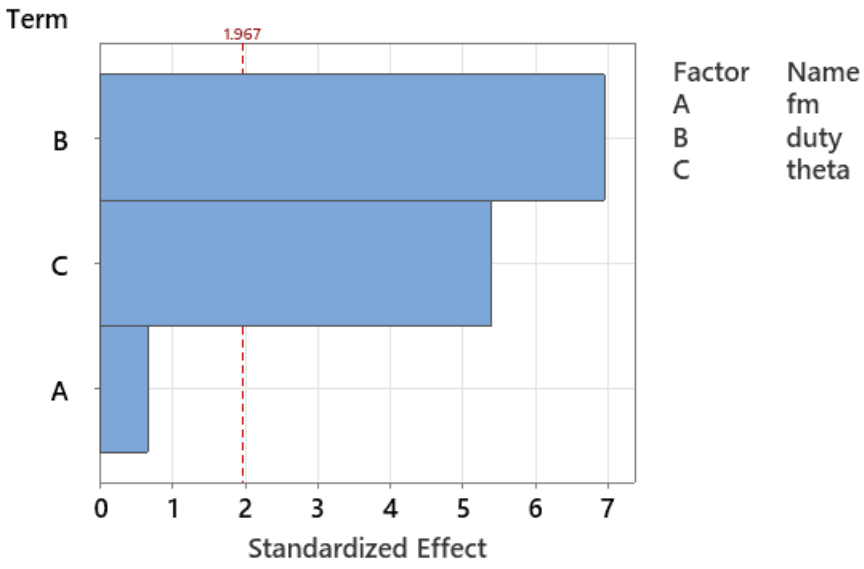

Figure 2.25: Pareto chart for velocity at x/h = 70.

Similarly to velocity, identifying the most critical operating parameters of plasma actuators is crucial for optimizing the temperature performance when controlling HAR rectangular jet. Full fractional designs was also utilized to draw Fig. 2.24 illustrating the main effects of different parameters for the normalized temperature at x/h = 70. Also, Fig. 2.25 shows the Pareto chart to summarize the analysis result: the duty is the most critical parameter that can affect the temperature at the driver's location; in contrast, the effect caused by modular frequency (f_m) is tiny.

These results differ from the velocity analysis, where the phase difference

(θ) and the modular frequency (f_m) substantially affect the velocity performance, and the effect caused by duty is tiny. There are some possible reasons for this difference. The velocity distribution in the jet is affected by viscous forces, which tend to smooth out the flow and make it more uniform. At the same time, the temperature is affected by heat transfer, which is a function of the temperature gradients. The viscous forces do not affect the temperature like the heat transfer phenomena. As a result, the flow-controlling effect archived by Plasma Actuator is different.

2.4 Energy analysis and Power consumption analysis of the high-aspect-ratio rectangular jet controlled by plasma actuators

2.4.1 Energy analysis

An energy analysis of the plasma actuator and a HAR rectangular jet was conducted to clarify whether the effect of the PA on the velocity was caused by the

injection of kinetic energy or the result of the flow manipulation. This could be achieved by calculating the ratio of the plasma actuator mechanical power (PA kinetic energy flux) to the rectangular jet kinetic energy flux. First, the kinetic energy flux of the rectangular jet was calculated using Equation (2.7):

$$\phi_k = \frac{1}{2}\dot{m}U_0^2 = \frac{1}{2}(\rho U_0 A)U_0^2, \tag{2.7}$$

where,

ϕ_k—Rectangular jet's kinetic energy flux;

$\dot{m}$—Mass flow rate;

ρ—Density of air;

A—Rectangular jet exit area; and

U_0—Initial velocity at the jet exit.

Secondly, the power consumption and kinetic energy flux of a single DBD Plasma Actuator were obtained by the shunt resistor method refer to Tang *et al.* [60] and Ashpis *et al.* [61]. Voltage and current were measured to calculate the power consumption of the Plasma Actuator at $duty$ = 1. The results are illustrated in Fig. 2.26. After that, the power consumption of a Plasma Actuator

was calculated using Equation (2.8):

$$W_{elec} = f_b \int_{t^*=0}^{t^*=1} V(t)I(t)dt, \tag{2.8}$$

where,

W_{elec}—Plasma actuator's electrical power consumption;

f_b—Base frequency;

$V(t)$—Voltage at each point in the period;

$I(t)$—Current at each point in the period; and

t^*—The normalized t represents a single period.

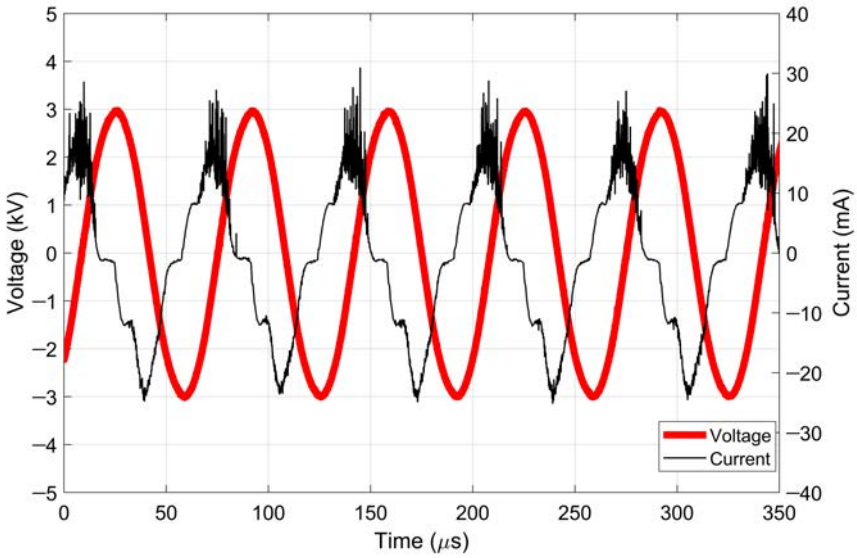

Figure 2.26: Voltage and current applied to a Plasma Actuator used in the experiments, where $duty$ = 1.

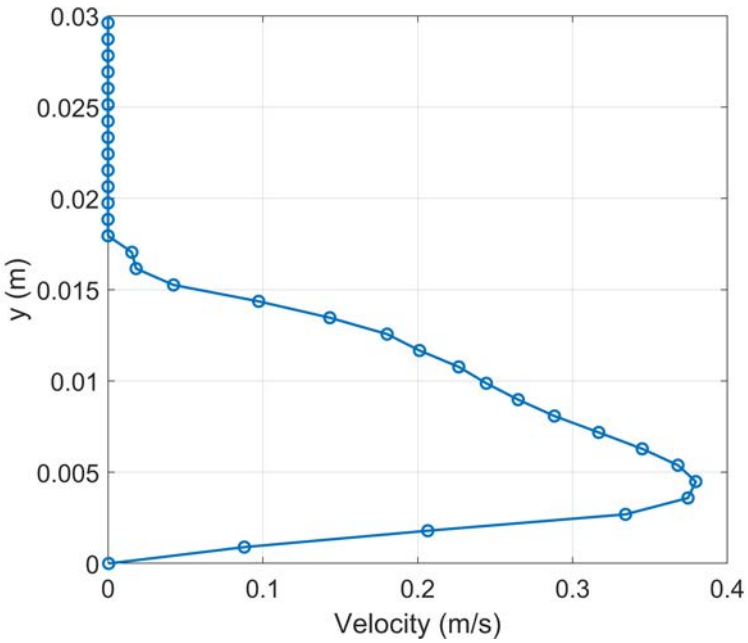

Figure 2.27: Velocity profile of a Plasma Actuator at a distance of 60 mm from the covered electrode.

The mechanical power of the plasma actuator can be calculated based on the velocity profile of a single PA, operating with $duty$ = 1, no free stream flow, and no external force, using Equation (2.9). Under these conditions, the momentum should theoretically be conserved in all velocity profiles. The plasma actuator velocity profile at x = 60 mm (Fig. 2.27) was used to calculate the PA mechanical power.

$$W_{mech} = \frac{1}{2}\rho L \int_{y=0}^{y=\infty} U^3(y)dy, \tag{2.9}$$

where,

W_{mech}—Plasma actuator's mechanical power;

ρ—Density of air;

L—Length of the Plasma Actuator;

$U(y)$—Velocity according to y coordinate at each point.

In this study, two PAs were used under the influence of the duty cycle. Therefore, the power consumption and kinetic energy flux for each case equaled the variables of a single DBD plasma actuator multiple by $(2\times duty)$ to obtain the results. The power analysis results for all cases are described in Table 2.6. The ratio of mechanical power to the power consumed by the plasma actuator as $\left(\frac{W_{mech}}{W_{elec}}\right)$ determines the conversion efficiency. This value was found to be 0.001%. It means most of the electric power was turned into heat energy. The ratio of $\left(\frac{W_{mech}}{\phi_k}\right)$ as the PA mechanical power (also known as PA kinetic energy flux) to the rectangular jet kinetic energy flux implies the power of the control input is influenced by a change in the kinetic energy in the form of velocity. The results show that for high-velocity performance in case A, the energy required to perform the active control technique is 0.048%, which is even smaller than that for case B. Case B, which has a lower velocity performance, has a higher value of energy requirement at 0.067%. Therefore, the plasma actuator can

perform velocity control with only a minor amount of power compared to the kinetic energy flux of the flow.

Table 2.6: Power analysis for all cases.

Case	**Description**	ϕ_k (**W**)	W_{elec} (**W**)	W_{mech} (**W**)	Q_k (**W**)	Q_{pa} (**W**)	$\frac{W_{mech}}{\phi_k}$(%)	$\frac{Q_{pa}}{Q_k}$(%)
Single PA	-	-	3.158	2.985×10^{-5}	-	3.158	-	-
A	High velocity	6.253×10^{-2}	3.158	2.985×10^{-5}	174.0	3.158	0.04773	1.815
B	Low velocity	6.253×10^{-2}	4.421	4.179×10^{-5}	174.0	4.421	0.06682	2.541
C	High Normalized Temp.	6.253×10^{-2}	1.263	1.194×10^{-5}	174.0	1.263	0.01909	0.726
D	Low Normalized Temp.	6.253×10^{-2}	5.052	4.776×10^{-5}	174.0	5.052	0.07637	2.904
E	Low Normalized Temp.	6.253×10^{-2}	2.526	2.388×10^{-5}	174.0	2.526	0.03819	1.452
F	High Normalized Temp.	6.253×10^{-2}	0.632	5.970×10^{-6}	174.0	0.632	0.00955	0.363

Generally, the plasma generated by an Alternating Current (AC) driven DBD plasma actuator is non-thermal plasma in which heavy species have temperatures close to the ambient temperature while the electron temperature is much higher [37]. The energy in this type of plasma is mainly stored in the electrons and consequently does not contribute to the gas's heating [62]. The ratio of $\left(\frac{Q_k}{Q_p a}\right)$ heat flux of the rectangular jet in the experiment to the heat flux of the plasma actuator was calculated to clarify whether the effect of the PA on the temperature was caused by the injection of thermal energy or it was the result of the flow manipulation. The heat flux of the rectangular jet was calculated using Equation (2.10). The heat flux of the plasma actuator was calculated using Equation (2.11), assuming that the total energy input was equal to the kinetic energy plus thermal energy.

$$Q_k = \dot{m} C_p \Delta_t = (\rho U_0 A) C_p \Delta_t, \tag{2.10}$$

where,

Q_k—Heat flux of the rectangular jet;

$\dot{m}$—Mass flow rate;

ρ—Density of air;

A—Rectangular jet exit area;

U_0—Initial velocity at the jet exit;

C_p—Specific heat of air at the experiment condition;

Δ_t—Temperature difference between the outlet and ambient temperature.

$$Q_{pa} = W_{elec} - W_{mech}, \tag{2.11}$$

where,

Q_{pa}—Heat flux of plasma actuator.

The heat-flux results are presented in Table 2.6. The two cases C and F show that only a small amount of energy compared to the heat flux of the flow (0.726% and 0.363% for cases C and F, respectively) can achieve 13.68% and 10.44% lower absolute temperatures (or higher normalized temperatures), respectively. Therefore, it can be concluded that flow manipulation caused a change in the jet temperature. Consequently, the thermal effect of the plasma actuator only affects small and local regions where the plasma exists and does not contribute to airflow heating in a considerably larger area.

Additional investigations on pressure loss caused by Plasma Actuator were conducted. Measuring the pressure drop of an actuator can be necessary for several reasons. One reason is to understand the actuator's performance and

how it affects the fluid flow [63]. By measuring the pressure drop caused by the actuator, it is possible to determine the efficiency of the actuator and how it affects the system's overall performance. Another reason to measure the pressure drop of an actuator is to optimize the design of the actuator. By understanding the pressure drop caused by the actuator, it is possible to make design modifications to improve the efficiency of the actuator and reduce the pressure drop. This can be important for improving the system's overall performance and reducing energy consumption.

Table 2.7: Pressure loss case details.

Case	Description
No Pa	There is no PA installed on the rectangular jet
Base	Plasma Actuators are OFF
Case A	High Velocity Case
Case C	High Normalized Temperature Case

The measurements are taken at a location of the YZ Cut section at x = 15 mm (x/h=2). The measurements are taken at a total of 424 points across an 8 $\times$ 53 measuring grid. This means that the measurements are taken at a total of 424 different locations in the fluid flow, giving a detailed and comprehensive picture of the pressure distribution of the fluid at various points in

the flow. To determine the pressure loss caused by the Plasma Actuator, the difference between the pressure measurements taken without the Plasma Actuator installed (No PA case) and with the Plasma Actuator turned OFF (Base case) is calculated. This will cause pressure loss due to installing the Plasma Actuator as a sudden contraction. To determine the pressure loss caused by the Plasma Actuator's body force, the difference between the pressure measurements taken with the Plasma Actuator operating and without the Plasma Actuator (Base case) is calculated. This will give the pressure loss due to the Plasma Actuator's body force on the flow, converting the mean energy of the flow into coherent structures. Table 2.7 shows the descriptions for pressure loss cases.

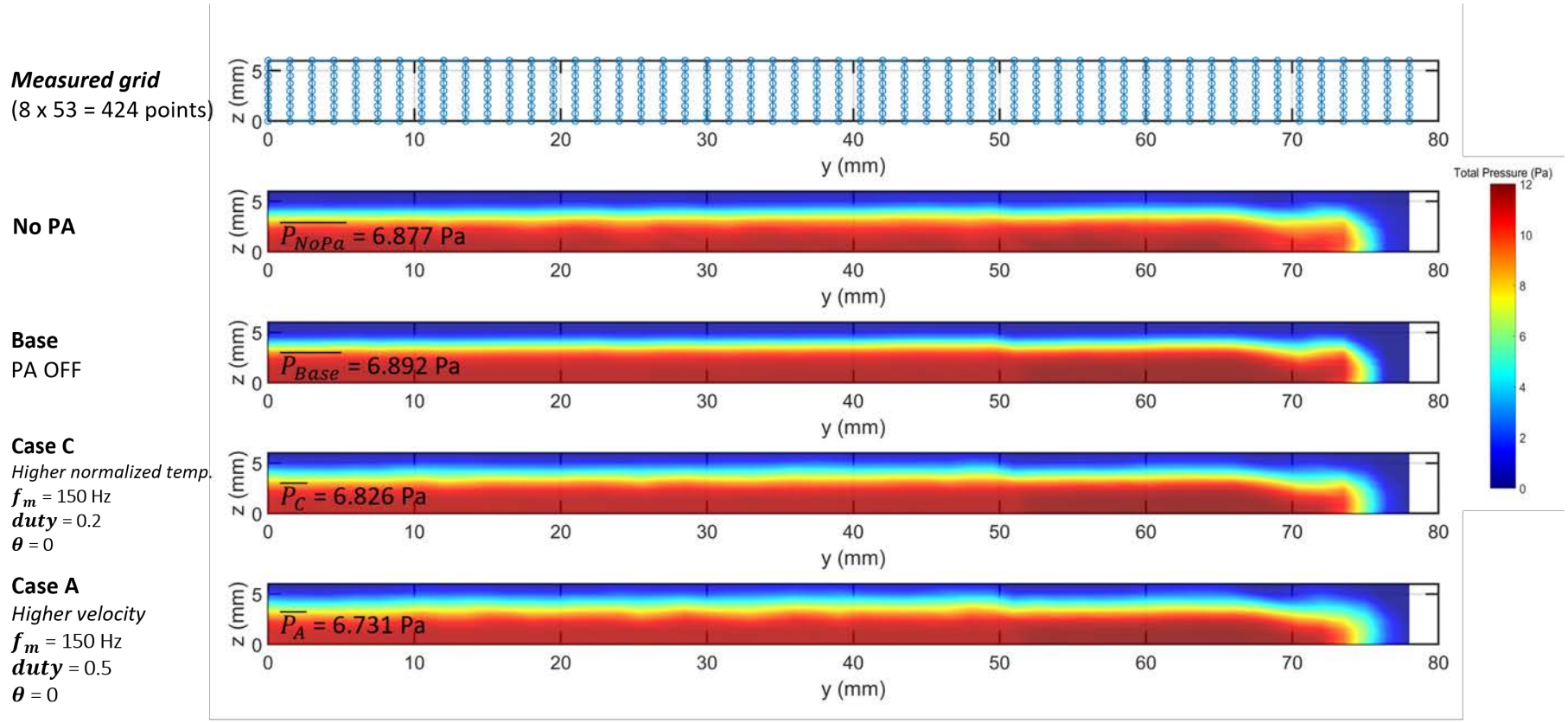

Figure 2.28: Pressure distribution for cases.

The results of total pressure distribution for cases show in Fig. 2.7. Pressure loss due to installation of Plasma Actuators as a sudden contraction can be calculated:

$$\overline{P_{NoPa}} - \overline{P_{Base}} = -0.015 \text{ Pa} \tag{2.12}$$

Pressure loss due to applying Plasma Actuators' body force:

Case A:

$$\overline{P_{Base}} - \overline{P_A} = 0.161 \text{ Pa} \simeq 2.34\% \text{ loss} \tag{2.13}$$

Case C:

$$\overline{P_{Base}} - \overline{P_C} = 0.066 \text{ Pa} \simeq 0.97\% \text{ loss} \tag{2.14}$$

Based on the pressure loss analysis results for the high-aspect-ratio rectangular jet controlled by a Plasma Actuator, the pressure loss caused by the installation of the Plasma Actuators is minimal and can be considered negligible. This is likely because the Plasma Actuators' protrusions are thin (70μm x 2) compared to the width of the rectangular jet (7.5 mm) and the thickness of the boundary layer (1.5 mm). The impact of the Plasma Actuators on the overall pressure of the fluid is minimal. The pressure losses caused by the operation of the Plasma Actuators are also relatively small compared to the velocity gain (15.47%) and temperature gain (13.68%) observed. Additionally,

the differences in pressure loss are within the precision range of the pressure sensor ($\pm 3\%$), indicating that the results are reliable and accurate. Overall, the pressure loss caused by the Plasma Actuators is minor compared to the total pressure of the rectangular jets. This suggests that the Plasma Actuators have a minimal impact on the overall pressure of the fluid and do not significantly alter the system's performance.

2.4.2 Power consumption analysis

Analysis of power consumption effectiveness of the active flow control by Plasma Actuator to the high-aspect-ratio rectangular jet for automobile A/C system is conducted. Let us take case A - High velocity to investigate how much power is needed to achieve the same result as Plasma Actuator controls the jet for the original A/C system. As seen in Eq. 1.4, to archive the velocity with case A while keeping the same normalized velocity, the initial velocity U_0 has to increase the same amount with the velocity increment for case A $\Delta_{V_A} = 15.47\%$. By looking at Eq. 2.7 and 2.10, when the initial velocity U_0 is increased, the kinetic energy flux and the heat flux of the rectangular jet are also increased with the relation:

$$\phi_k \propto {U_0}^3 \text{ and } Q_k \propto U_0$$

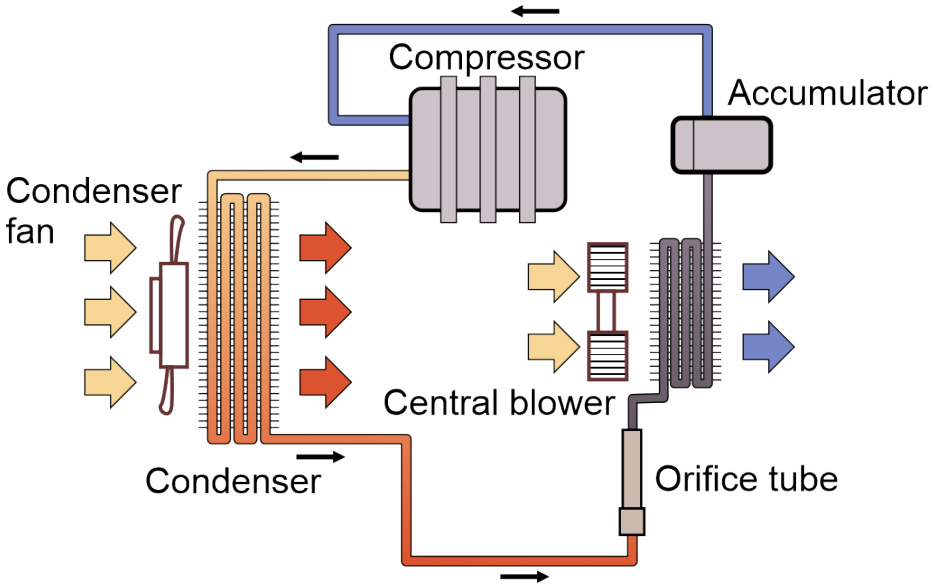

Figure 2.29: Automobile or Car Air Conditioning System Schematic.

Table 2.8: Power consumption for base case, case A, and case A*.

	Baseline (No PA)	Case A Δ_U = ▲15.47% (With PAs)	Case A* Δ_U = ▲15.47% (No PA)
Power Consumption	$P_{fan/blower}$ = 24.48 W $P_{compressor}$ = 1080 W	$P_{fan/blower}$ = 24.48 W $P_{compressor}$ = 1080 W P_{PA} = 3.16 W	$P_{fan/blower}$ = 37.69 W $P_{compressor}$ = 1247.08 W
Total (Δ_P – Difference)	P_{noPA} = 1104.48 W	P_{caseA} = 1107.64 W **(▲0.29 %)**	P_{caseA^*} = 1284.77 W **(▲ 16.3 %)**
Velocity Gain Ratio $\Delta_U / \Delta_{P_{fan/blower}}$	-	**1.2**	**0.29**
System Gain Ratio Δ_U / Δ_P	-	**53.34**	**0.95**

The kinetic and heat flux will increase by $\Delta_{\phi_k} = 53.95\%$ and $\Delta_{Q_k} = 15.47\%$,

respectively, to archive the same result as Case A. The central blower and the compressor will use as much energy to increase the kinetic energy flux and the heat flux at the nozzle exit (refer to Fig. 2.29). Therefore, the total power consumption of the A/C system will be increased to compensate for increasing the jet's initial velocity. The power consumption of the wind tunnel (acting as a central blower in the A/C system) and circulator chiller (acting as compressor and radiator in the A/C system) is $P_{fan} = 24.48$ W and $P_{com} = 1080$ W, respectively. To archive the same result as Case A as case A*, power consumption for fan $\Delta_{P_{fan}}$, for compressor $\Delta_{P_{comA}}$, and the total A/C system Δ_P are needed to be increased. The details of the power consumption for these cases are shown in Table 2.8.

$$\Delta_{P_{fan}} = \Delta_{\phi_k} \times P_{fan} = 13.21 \text{ (W)}$$

$$\Delta_{P_{com}} = \Delta_{Q_k} \times P_{com} = 167.08 \text{ (W)}$$

$$\Delta_P = \Delta_{P_{fan}} + \Delta_{P_{com}} = 180.29 \text{ (W)}$$

The power consumption for Plasma Actuator in case A is $W_{elecA} = 3.16$ (W). Based on that, it can be concluded that to archive the same velocity improvement as case A:

- As for the velocity only, Plasma Actuator consumes 22.71% the amount of energy comparing with ordinary A/C system (case A*). The velocity gain

ratio (calculated by the ratio of increment of velocity over the increment of input energy for the fan or blower $\frac{\Delta_U}{\Delta_{fan}}$) for case A is 1.2, which means that the flow control technique can archive better power saving in terms of kinetic energy.

- As for the total system power consumption, Plasma Actuator consumes 1.75% of the amount of energy compared with an ordinary A/C system. Which results in a huge AC system gain ratio of 53.34. Active flow control by Plasma Actuator can result in a benefit in terms of AC system energy usage.

In a modern automobile, the A/C system will use about four-horsepower (3 kW) of the combustion engine's power or from the electric car's battery (for electric vehicle), thus increasing fuel consumption or decreasing the vehicle's mileage [64]. The central blower (which generates the velocity for the A/C outlet) will use approximately 20% of all energy in automobile A/C system [65], the rest will go to the compressor, and a minor amount of energy goes to the controlling system that can be negligible. As a result of this analysis, using this AFC for a high-aspect-ratio rectangular jet air vent could improve the fuel consumption of an automobile.

2.5 Chapter Summary

- The combination of modular frequency f_m, duty, and phase difference θ determines the working condition of the plasma actuators and has different effects on the HAR (width-to-height ratio 20) rectangular jets flow features;

- Modular frequency substffects the velocity of the rectangular jet compared with duty. In contrast, changing the duty cycle influences the temperature better than the modular frequency. Plasma Actuator can affect the velocity and temperature at a particular point, centerline profile, and distribution across cut sections;

- The plasma actuator can cause the axis-switching phenomenon to occur at a location closer to the rectangular nozzle outlet (Case E). It results in a "thick" distribution of the high normalized temperature in this identical area;

- The maximum improvement for velocity is 15% higher, and the temperature is 14% higher, measured at x/h = 70 on the centerline. The actuator can perform velocity and temperature control with only a minor power compared to the rectangular jet's kinetic energy and heat flux. Because of

that, using this technique for a high-aspect-ratio rectangular jet air vent could improve automobile fuel consumption.

Chapter 3

The Mechanisms of High-aspect-ratio Rectangular Jet Width Controlled by Plasma Actuators

Abstract

Next, this chapter is dedicated to understanding the mechanism of how the Plasma Actuator affects the HAR rectangular jet to use it to craft turbulent structures in the flow and overdrive the vortex-forming nature of the jet, known as Kelvin—Helmholtz Instability. The width of a turbulent jet can significantly affect the flow's velocity and temperature distribution. A wider jet will have a more diffuse velocity and temperature distribution, while a narrower jet will have a more concentrated distribution.

This is because a wider jet will have a greater area over which the fluid can spread out, resulting in a lower velocity and temperature at any given point. Conversely, a narrower jet will have a smaller area over which the fluid can spread out, resulting in a higher velocity and temperature at any given point. Additionally, the width of the jet can also affect the fluid's mixing and the energy dissipation rate, which can also impact the flow's overall velocity and temperature distribution. Therefore, understanding the mechanisms of High-aspect-ratio Rectangular Jet Width controlled by Plasma Actuators will play a vital role in controlling the velocity and temperature.

3.1 Flow Features and Turbulent Structure of High-Aspect-Ratio Rectangular Jet Controlled by PAs

The visualization results of all cases are shown in Fig. 3.1. To obtain a good visualization using a PIV laser sheet and a high-speed camera, it is important to use a lens with a focal length of 50mm. This will ensure that the image captured by the camera is properly focused and has a good field of view. Additionally, since the environment where the PIV laser sheet is used is dark, it is recommended to use an f1.2 or f1.0 aperture lens. This will allow the camera to capture the low light emitted by the laser sheet, resulting in a well-lit and detailed image. It is also crucial to make sure that the focus of the camera is located at the laser sheet. And to ensure the proper amount of smoke is ejected into the flow by the smoke generator, not too much, not too little, this will make the laser sheet more visible, and make the data captured more accurate. This will ensure that the laser sheet is clearly visible in the final image, making it easy to analyze the data captured by the PIV system.

The Kelvin–Helmholtz instability (KHI) vortex appears at the initial vor-

tex's base case. This instability vortex occurs at the interface where two fluid streams with relative motion come into contact [66] [67] because the rectangular jet flows into the still air. The KHI vortex size becomes smaller while traveling streamwise, as can be seen at the X–Y Top View; these vortices lead to a potential core breakdown into turbulence at x/h = 6 [68]. The KHI mechanism of the vortex roll-up and intense mixing between two fluids are comprehensively described by Caulfield and Peltier [69].

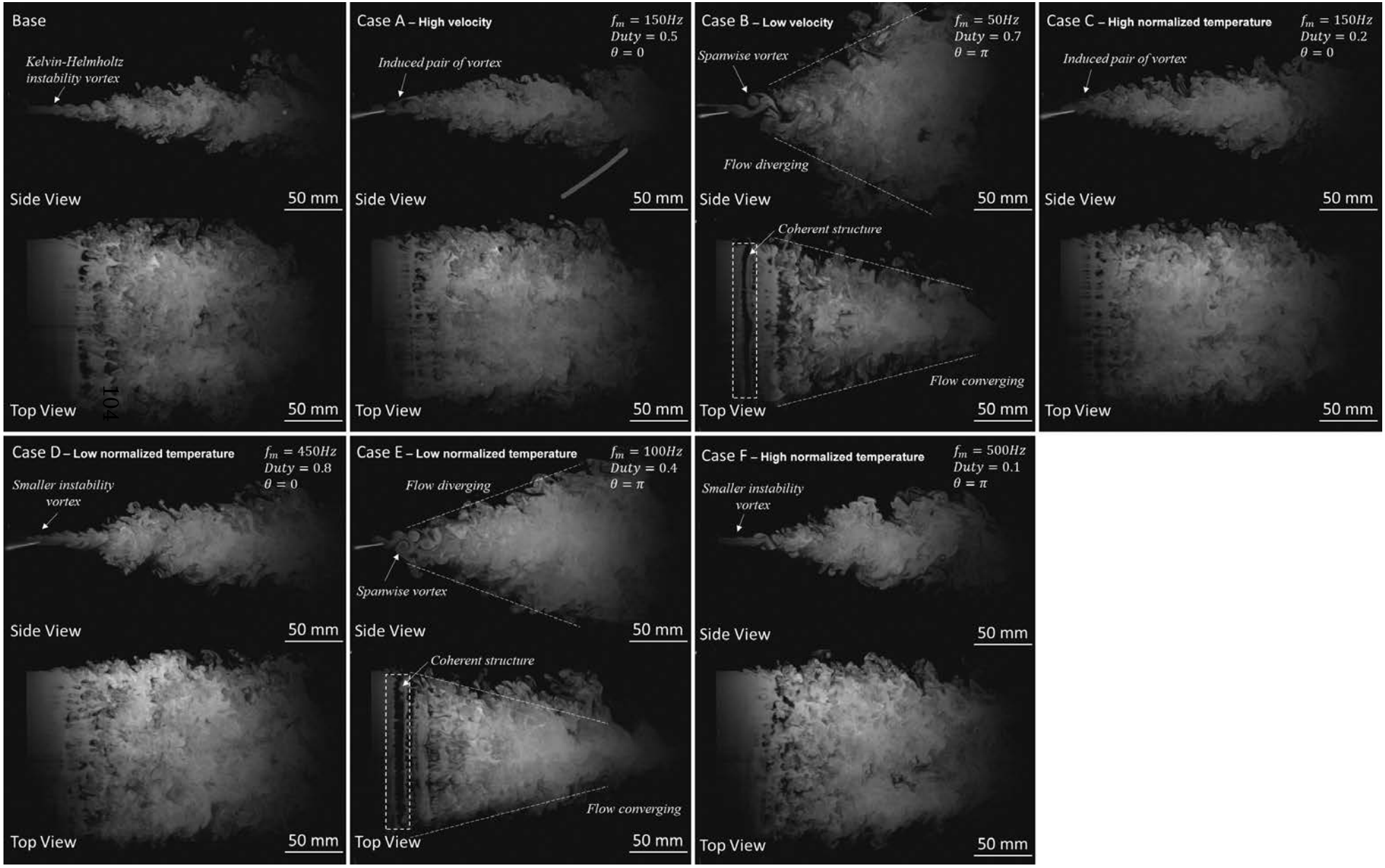

Figure 3.1: Spontaneous flow visualization results for different cases on X–Z Side View and X–Y Top View recorded at 2000 fps.

In cases A and C, the higher velocity and higher normalized temperature cases, respectively, two PAs operating simultaneously induce the flow with plasma wind creating pairs of vortexes, as observed in the X–Z Side View. From the Top View, we see that the flows slightly converge. The vortex-generating frequency can be obtained by counting the number of vortexes in the high-speed camera footage and dividing it by the recorded time. It is found that the vortex-generating frequencies in cases A, B, C, and E are equal to the modular frequency f_m induced by PAs. Furthermore, minor instability compared with the KHI vortexes was found in cases D (low normalized temperature) and F (high normalized temperature) when the modular frequency was higher than that in other cases at 450 and 500 Hz, respectively. Therefore, PAs overdrive the KHI vortex generating frequency.

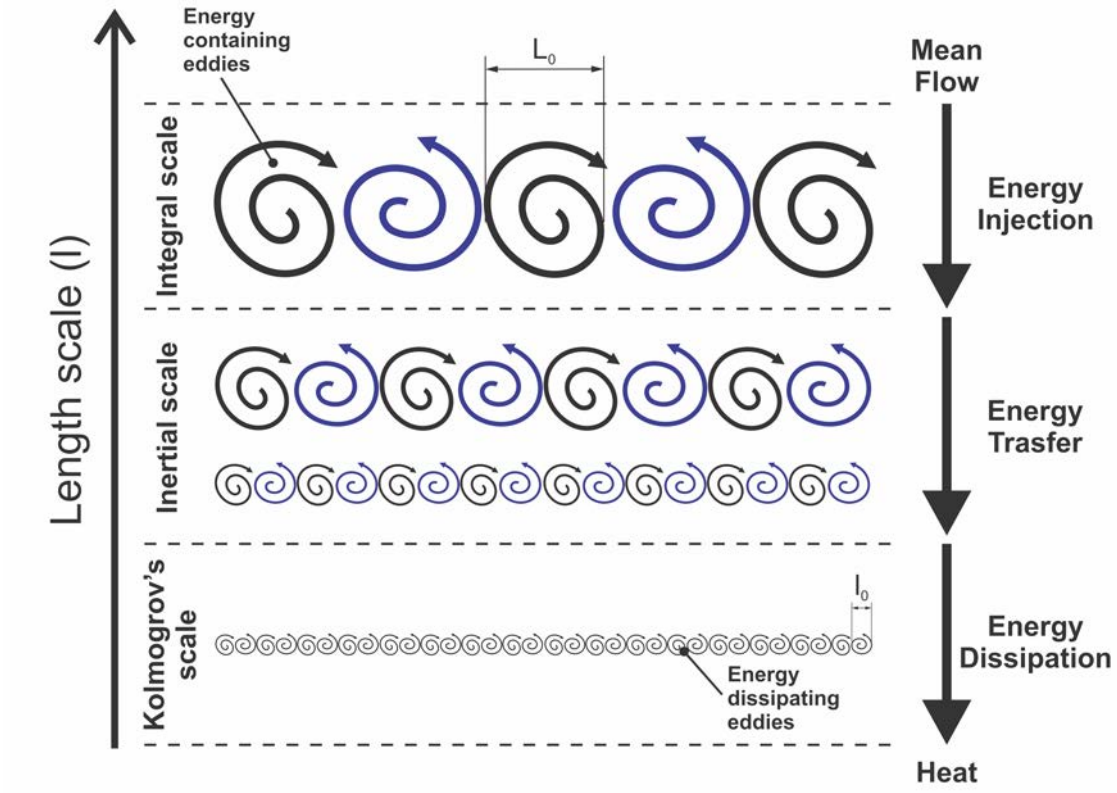

Figure 3.2: Scaling in coherent structures.

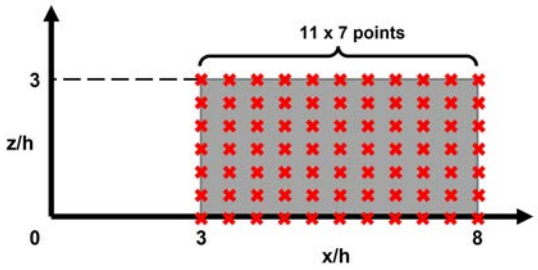

Figure 3.3: Velocity, integral length scale, and dissipation length scale measurement locations.

A train of vortexes is found in cases B (lower velocity) and E (lower normalized temperature), as seen from the X–Z Side View in Fig. 3.1. Moreover, the sizes of individual structures are different. The small vortical structures are random turbulent motions, whereas the spanwise structures appear as coherent structures. These vortex structures are detected by straight bars of smoke and void sequentially appearing in the visualized footage on the X–Y Top View. This phenomenon stemmed from the vectoring effect of PAs operated in alternating mode (i.e., phase difference equals π) combined with the periodic excitation effect when the modular frequency is applied. Furthermore, PAs make the jet width diverge on the X–Z Side View and converge on the X–Y Top View as the spanwise vortex shortens when traveling in the streamwise direction. This observation alludes to the existence of different structures representing various scales in rectangular jet flow controlled by PAs.

Turbulence development in a rectangular jet can be described as a transition from a smooth, orderly flow to a chaotic and disordered flow [70]. When a fluid is forced through a small opening, it creates a laminar jet. This jet initially flows smoothly and orderly in a straight line. As the jet travels further from the opening, the velocity of the fluid decreases and the pressure increases. This causes the jet to spread out and the flow to become less stable. As the jet continues to spread, small disturbances called “vortices” begin to form. The

vortices that form in the jet are called “Kelvin-Helmholtz Instability” vortices, they can also be seen as “roll-up” of the fluid layer. This instability is caused by the difference in velocity between the fluid layers, and it results in the formation of vortices and the breakdown of the laminar flow. As the vortices grow in size and number, they begin to interact with each other, creating even more disturbances in the flow.

Figure 3.2 shows a schematic of the scaling in coherent structures [71] to explain the energy cascading concept. Two physical phenomena occur simultaneously to assemble the flow features. The first process is the formation and growth of the coherent structures owing to the KHI appearing in the base case; the other is self-organization resulting from the flow excitation of PAs. The second process is the energy cascade phenomenon, where the vortical structure size gradually decreases owing to the interaction between multi scale structures. The well-known Kolmogorov scaling law [72] indicates that the largest structure in the flow is the size of the coherent structure holding approximately 80% of the total kinetic energy [73], known as the integral length scale L. The smallest one includes the cascaded structures and random eddies, known as the dissipation scale l or Kolmogorov scale, responsible for turbulent energy dissipation. While the mean and random energies are transferred to the coherent energy by PAs, the coherent energy is transferred to random energy

through the cascade. The random energy is then transferred to heat (molecular energy) through the energy dissipation process. It is currently unknown if there has been any research conducted on using a Plasma Actuator in combination with integral length scale for controlling jet applications. This study aims to be the first to investigate and apply this novel technique, filling the gap in current knowledge.

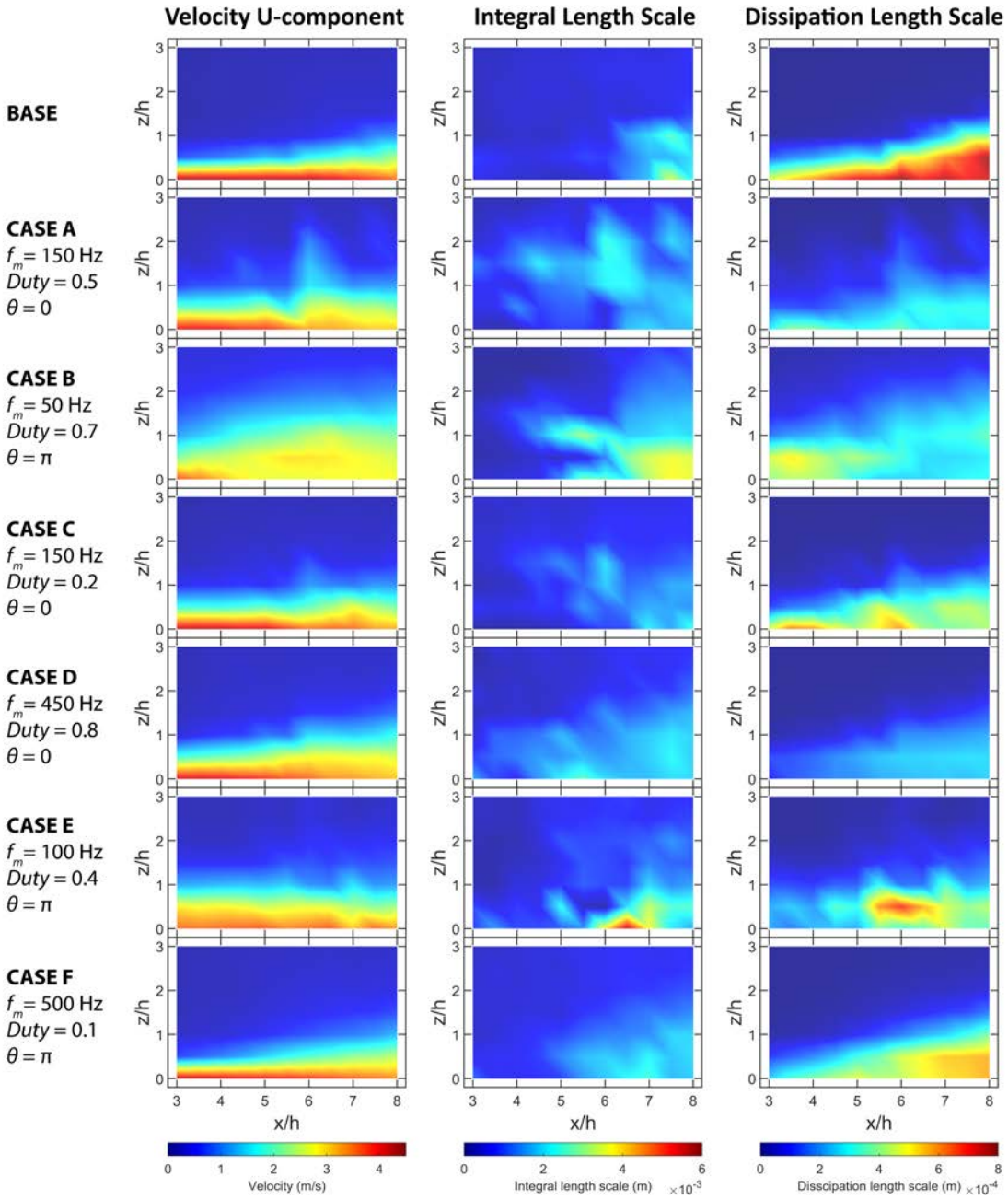

Figure 3.4: U-component velocity, integral length scale, and dissipation scale measurement results for test cases.

A grid containing 77 measuring points where the vortices appeared the most on the visualization results, as shown in Fig. 3.3, was selected to capture the velocity and integral and dissipation length scales for all experimental cases to measure the shear layer near the nozzle exit. The quantitative results of these measurements are shown in the contour plots in Fig. 3.4. The larger the integral scale in the middle column figures, the larger the coherent structures. The dissipation length scale in the right column figures is one order of magnitude smaller than the integral length scale. When PAs are operating, they increase the integral length scale at locations where there is none at the base case from x/h = 3 to 6. PAs also decrease the dissipation length scale in all cases. Without any actuator, the integral length scale depends only on the size and geometry, and the dissipation scale depends on the dissipation rate and viscosity [74] [75]. This result indicates that PAs can change these two length scales without changing flow boundary conditions. Furthermore, when the phase difference equals π, the integral length scale shows larger structures in the flow compared with the others. The most significant coherent structures can be found in case E, where the integral length scale reached the maximum value at 6 mm.

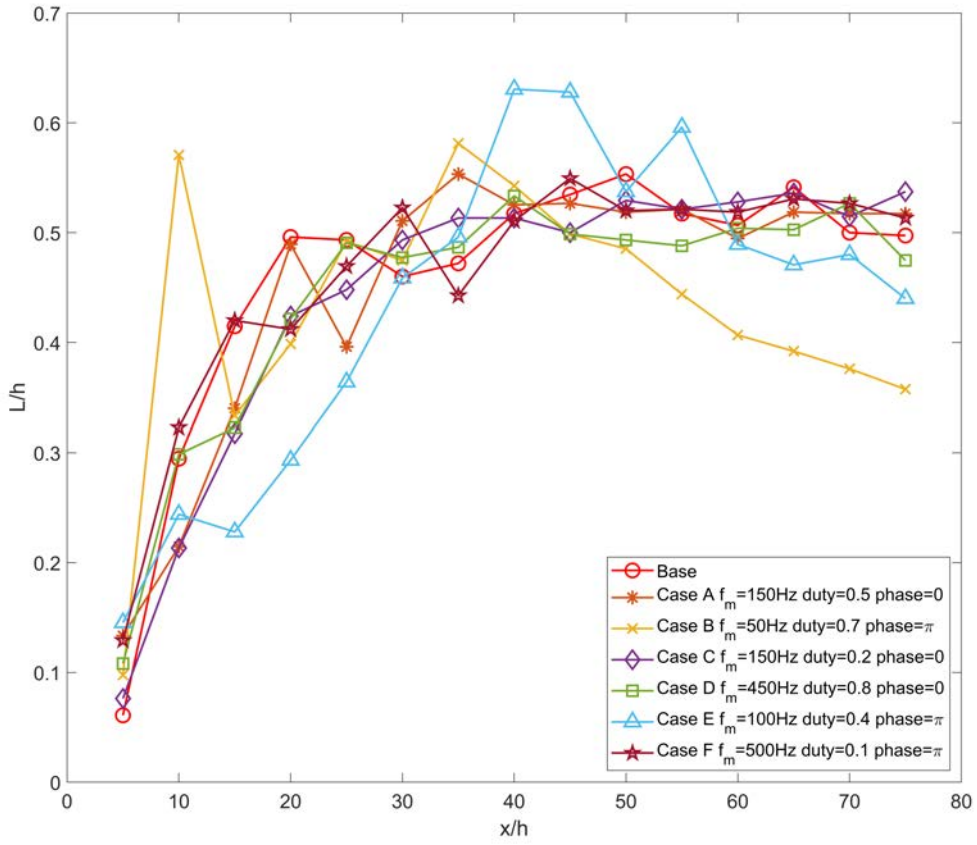

Figure 3.5: Integral length scale along the centerline.

Figure 3.5 shows the integral length scales along the centerline. Except for the two cases with significant coherent structures (i.e., cases B and E), other cases behaved similarly as the structures grew from the nozzle outlet to x/h = 30, where they reached approximately 0.5h and then stabilized. In cases B and

E, the integral length scale reached the first peak (where x/h = 10) and then reduced to the first minimum (where x/h = 15). Subsequently, the scale reached its maximum and then decreased linearly. This represents the mechanisms of energy cascade for cases with larger structures that gradually cascade into smaller ones after covering some distance.

3.2 Mechanism of Rectangular Jet Divergence and Convergence by PA

The mechanism of the diverging and converging of the jet width will strongly relate to the velocity and temperature of the flow. In cases E and B, the jet width diverges on the X–Z Side View and converges on the X–Y Top View. Because case E has the largest coherent structure, it was selected to examine the divergent and convergent mechanisms of the rectangular jet width. An observation plane parallel to the X–Y plane where z = 6 mm (Fig. 3.1 for case E) is shown on Fig. 3.6. Because the observation plane cuts through the spanwise vortex cores, this provides better clues than the observation at the X–Y Top View of the coherent structures by multiple straight bars of smoke and void sequentially appearing in the observed footage. Moreover, convergence of the flow can be observed on the observation plane.

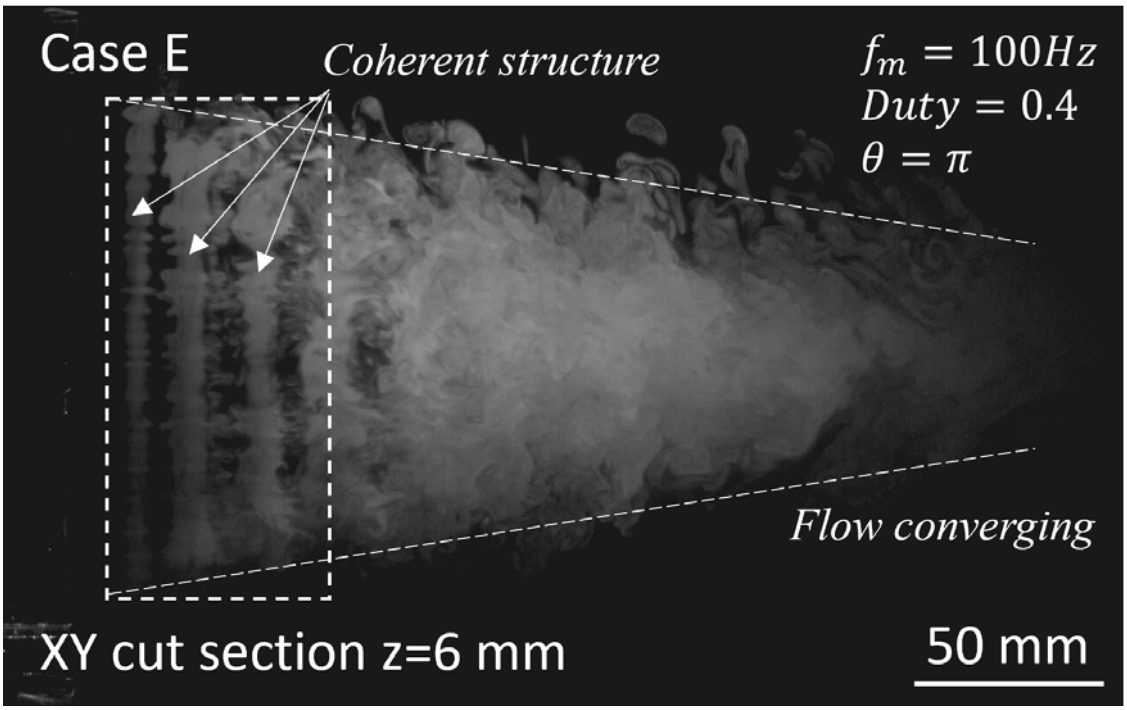

Figure 3.6: Spontaneous flow visualization result of case E on XY cut section while z = 6 mm recorded at 2000 fps.

Flow visualization videos were analyzed by 2D PIV software to extract the velocity and vorticity data. Since the analysis is only on the observed plane, there is a limitation compared with 3D PIV analysis because the measured velocity has only two-dimensional components on the observation plane. Figure 3.7 shows the average velocity contour of case E on the observation plane. The distribution shows the convergence jet width as it is concentrated into a small local area by the centerline from x/h = 15 to 20 maximum at 2 m/s. The

velocity along the y-direction as the V-velocity component velocity is extracted from the mean velocity results in Fig. 3.8. The V-velocity component is directed toward the centerline as the entrained air is drawn into the core of vortexes. This occurs because the train of spanwise vortexes creates a low-pressure zone when it travels streamwise; the same phenomena can be observed in the vortex shedding flow around a cylinder [76] [77]. Additionally, the visualization video shows that the edge of the vortex breaks down into smaller structures which shortens the spanwise vortex when it travels streamwise and finally resulting in a convergence effect of the flow from the X–Y Top View, as seen in Fig. 3.1. From the X–Z Side View, the flow diverges because of momentum conservation.

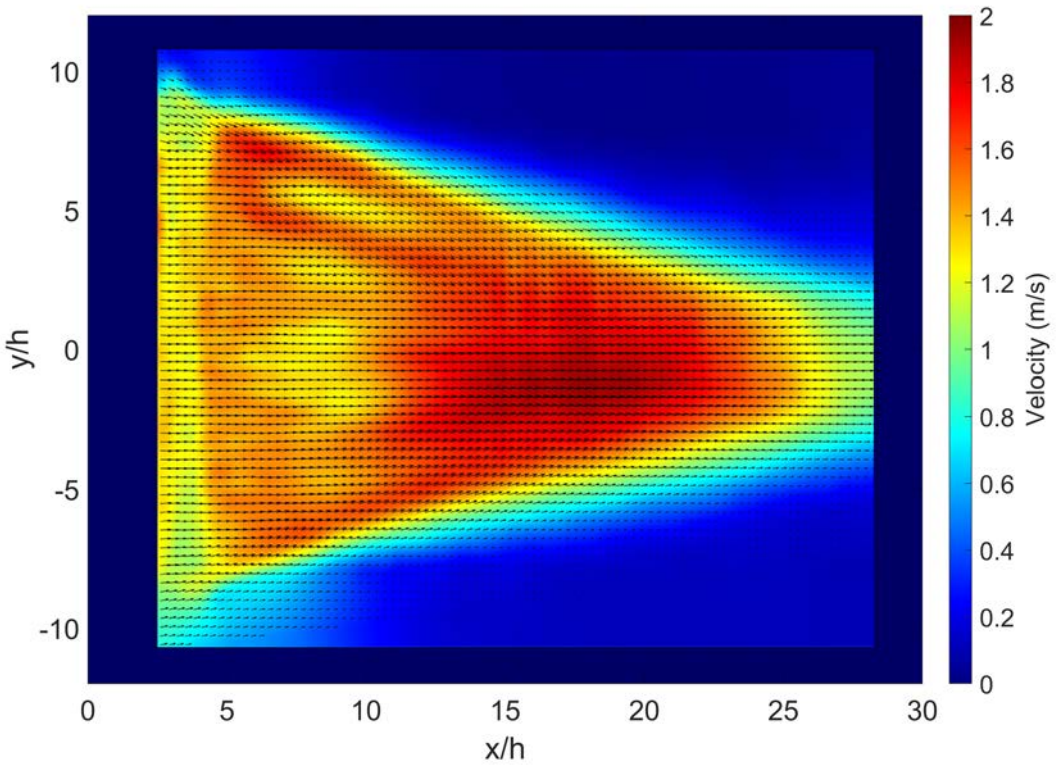

Figure 3.7: Case E, PIV average velocity contour plot on XY parallel plane z = 6 mm.

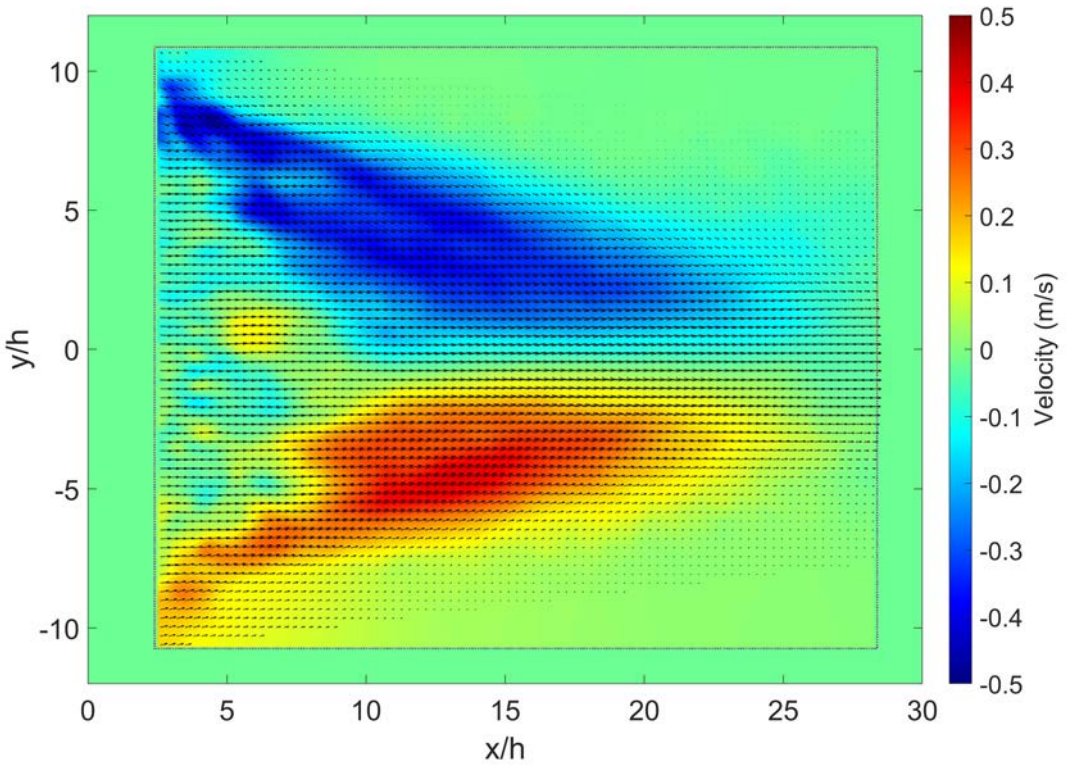

Figure 3.8: Case E, PIV average v component velocity contour plot on XY parallel plane z = 6 mm.

The vorticity distribution on the observation plane is shown in Fig. 3.9. A positive value indicates that the rotation is in the counter-clockwise direction and vice versa. Vorticity values on the top and bottom shear layers have absolute values higher than the inner part of the flow, and their directions are toward the core of the flow. This interpretation is consistent with the V-velocity component results in Fig. 3.8 where the entrainment is directed to the center-

line of the flow. When x/h = 5–14, areas with alternating vorticity signs can be observed as indicated by the $+/-$ signs in Fig. 3.9. The vorticity results reveal the primary coherent structure interacting with the main spanwise vortexes created by the PA effect. Further, the multiscale turbulent structure interacts with random turbulence in the environment, resulting in the primary and secondary structures, as seen in Fig. 3.10. Melander *et al.* [78] studied these structures by direct numerical simulation (DNS) to show the concept of a coherent vortex, as the vortex always couples with a group of smaller-scale vortices winding around it. The existence of these structures is proof of the turbulence cascade and hints at a highly dissipative structure. This proves that the train of spanwise vortexes created by the PA exists in a dissipative environment as the rectangular jet is emitted into the still air.

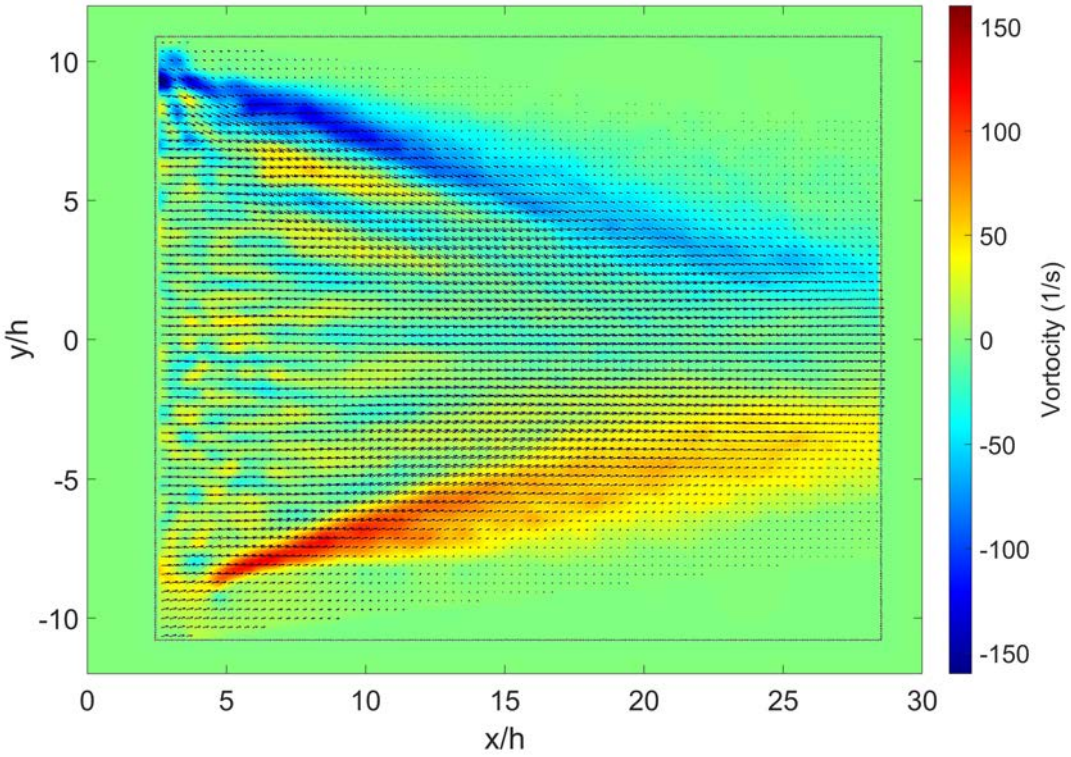

Figure 3.9: Case E, vorticity contour plot on the X–Y Top View at z = 6 mm.

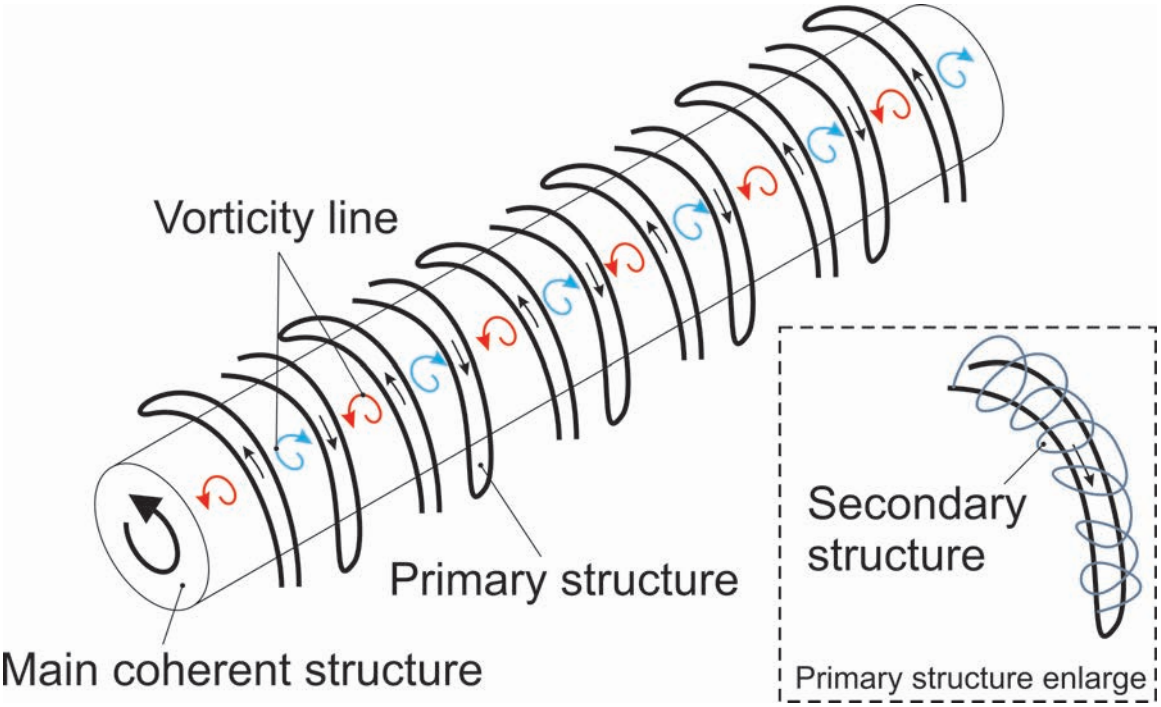

Figure 3.10: Schematic of a coherent structure interacting with random turbulence to create primary and secondary structures.

The vorticity equation is used to explain the mechanisms of jet convergence and divergence induced by the PA. The equation describes the development and decay of any vortex system on all length scales. The derivation of Eq. 3.1 was carried out by Holton *et al.* [79].

$$\overbrace{\frac{D(\zeta+f)}{D_t}}^{\text{I}} = \overbrace{-(\zeta+f)\left(\frac{\delta u}{\delta x}+\frac{\delta v}{\delta y}\right)}^{\text{II}} \overbrace{-\left(\frac{\delta w}{\delta x}\frac{\delta v}{\delta z}-\frac{\delta w}{\delta y}\frac{\delta u}{\delta z}\right)}^{\text{III}} \overbrace{+\frac{1}{\rho^2}\left(\frac{\delta \rho}{\delta x}\frac{\delta \rho}{\delta y}-\frac{\delta \rho}{\delta y}\frac{\delta \rho}{\delta x}\right)}^{\text{IV}}, \tag{3.1}$$

where:

ζ – relative vorticity caused by wind or flow control;

f – planetary vorticity caused by rotation of the earth (for this application, the effect is neglected as $f \approx 0$);

x, y, z – component of coordinate system;

u, v, w – velocity component according to the coordinate system;

ρ – mean density of the fluid.

Term I on the left side of Eq. 3.1 is the rate of change of absolute vorticity $(\zeta + f)$ following the fluid motion. Term II is called the divergence term or vortex stretching. It represents the effects of divergence (compression) and convergence (stretching) on absolute vorticity. Terms III and IV are the transfer of vorticity between horizontal and vertical components and the effect of baroclinicity, respectively. In term II, if $\left(\frac{\delta u}{\delta x}+\frac{\delta v}{\delta y}\right) > 0$ or the horizontal flow is

divergent, vorticity will be diluted since vorticity decreases if absolute vorticity is positive and increases if absolute vorticity is negative. Figure 3.11 shows the vorticity distribution on the X–Z Side View of the flow. The peaks are found at x/h = 7 after which the vorticity decreases. Figure 3.12 shows the vorticity on the X–Z Side View plane along z = 6 mm for a qualitative comparison. The vorticity sharply increases to get the peaks, and then linear decreases. Because the rectangular jet flow existed in the dissipative environment, the horizontal flow is divergent. This results in compression because the absolute vorticity decreases following the fluid motion.

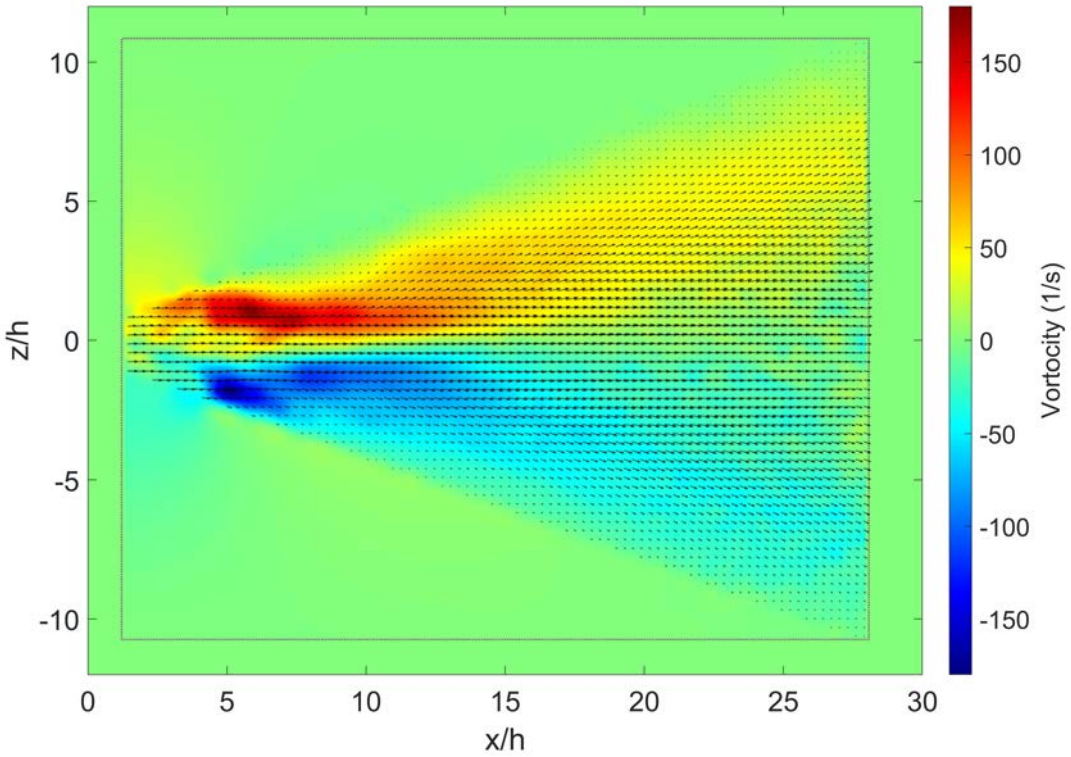

Figure 3.11: Case E, vorticity contour plot on the X–Z Side View.

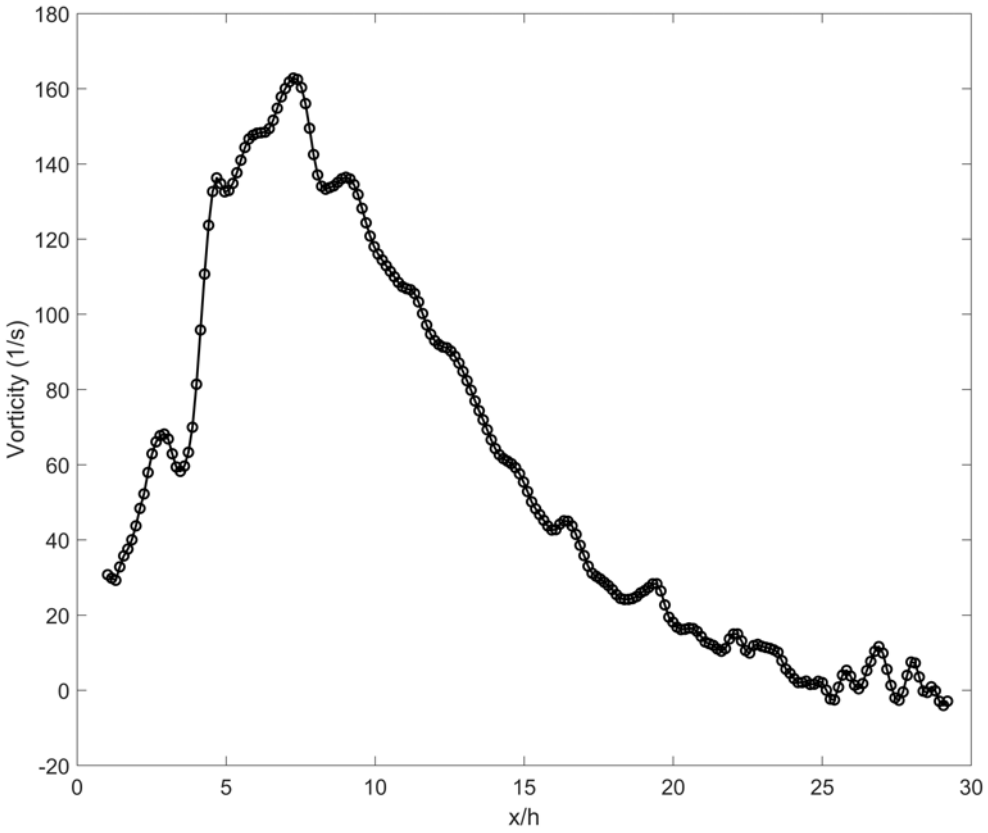

Figure 3.12: Vorticity distribution along y = 0 and z = 6 mm.

$$\frac{D_l}{D_t}\left[\frac{\zeta + f}{l}\right] = 0, \tag{3.2}$$

where: l – length of the coherent structure.

Rossby [80] [81] was the first to introduce the concept of potential vorticity (PV). The PV concept assumes that the fluid is homogeneous and horizontal scales are much larger than the depth of the fluid. The simple form of the PV equation is expressed by Eq. 3.2, where the ratio of $\frac{\zeta+f}{l}$ represents PV. Since PV is conserved while the fluid is in motion, it has a clear physical meaning, as the absolute vorticity must be proportional to the length of the coherent structure. When the absolute vorticity decreases, as seen in Figs. 3.11 and 3.12, the length of the coherent structure also decreases. As a result, the flow converges from the X–Y Top View, and from the X–Z Side View, it diverges owing to the momentum conservation law. This continues until the vortex is fully broken into smaller structures or turbulent flow. By understanding the mechanism, the spanwise vortex created by PA can be utilized to introduce coherent structure into the flow to control the jet width, depending on the orientation of the PA relative to the rectangular jet (e.g., on the long edge or the short edge) converging or diverging effects can be achieved. Because the width of a rectangular jet can significantly affect the flow's velocity and temperature distribution, wider jet width (more mixing effect, velocity, and temperature spread more evenly) and narrower jet (less mixing effect, velocity, and temperature are more focused and less decayed) can be obtained using this know-how to control

the HAR rectangular jet.

3.3 Energy Spectra Analysis of Rectangular Jet with Plasma Actuator

By using the FFT, the velocity trace in the time domain can be converted into the frequency domain for further analysis. Figures 3.13, 3.14, 3.15, and 3.16 show the single-sided amplitude and energy density spectra of all cases measured at the shear layer where x/h = 3, y/h = 0, and z/h = 0.5. The power spectrum indicates the relative magnitudes of the frequency components of the physical phenomena that combine to make up the flow. For the base case, the dominant frequency caused by KHI was 392.6 Hz. The dominant frequencies in cases where PA could create coherent structures, i.e., cases A, B, C, and E were double the PA modular frequency applied to the case. The harmonic of the dominant frequency can also be observed in these cases. For example, in case B where the modular and dominant frequencies are 50 Hz, several harmonic frequencies are multiples of the dominant frequency as 100, 200, 300, 400, 500 Hz, etc.

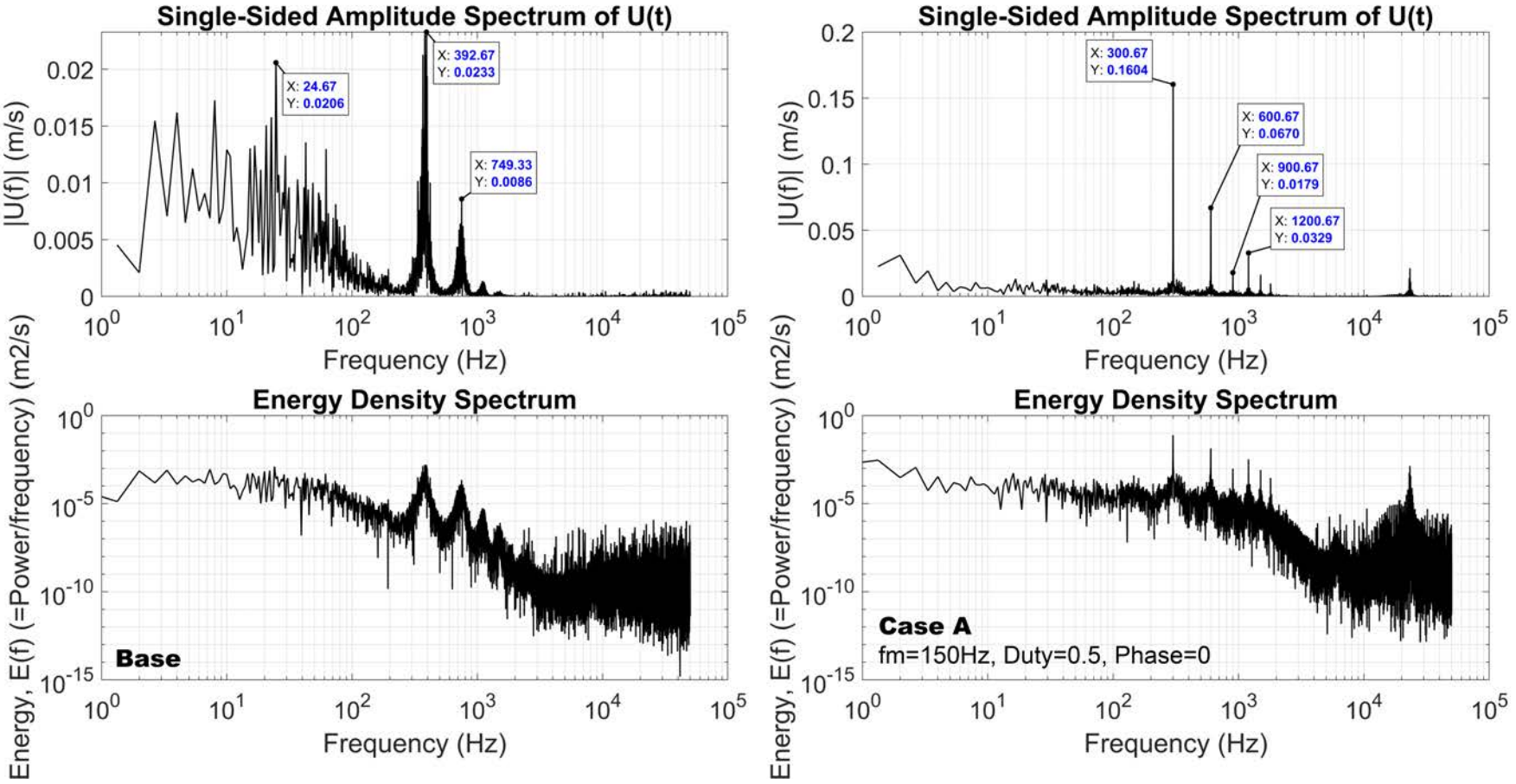

Figure 3.13: Single-sided amplitude and energy density spectra of all cases at x/h = 3, y/h = 0, and z/h = 0.5.

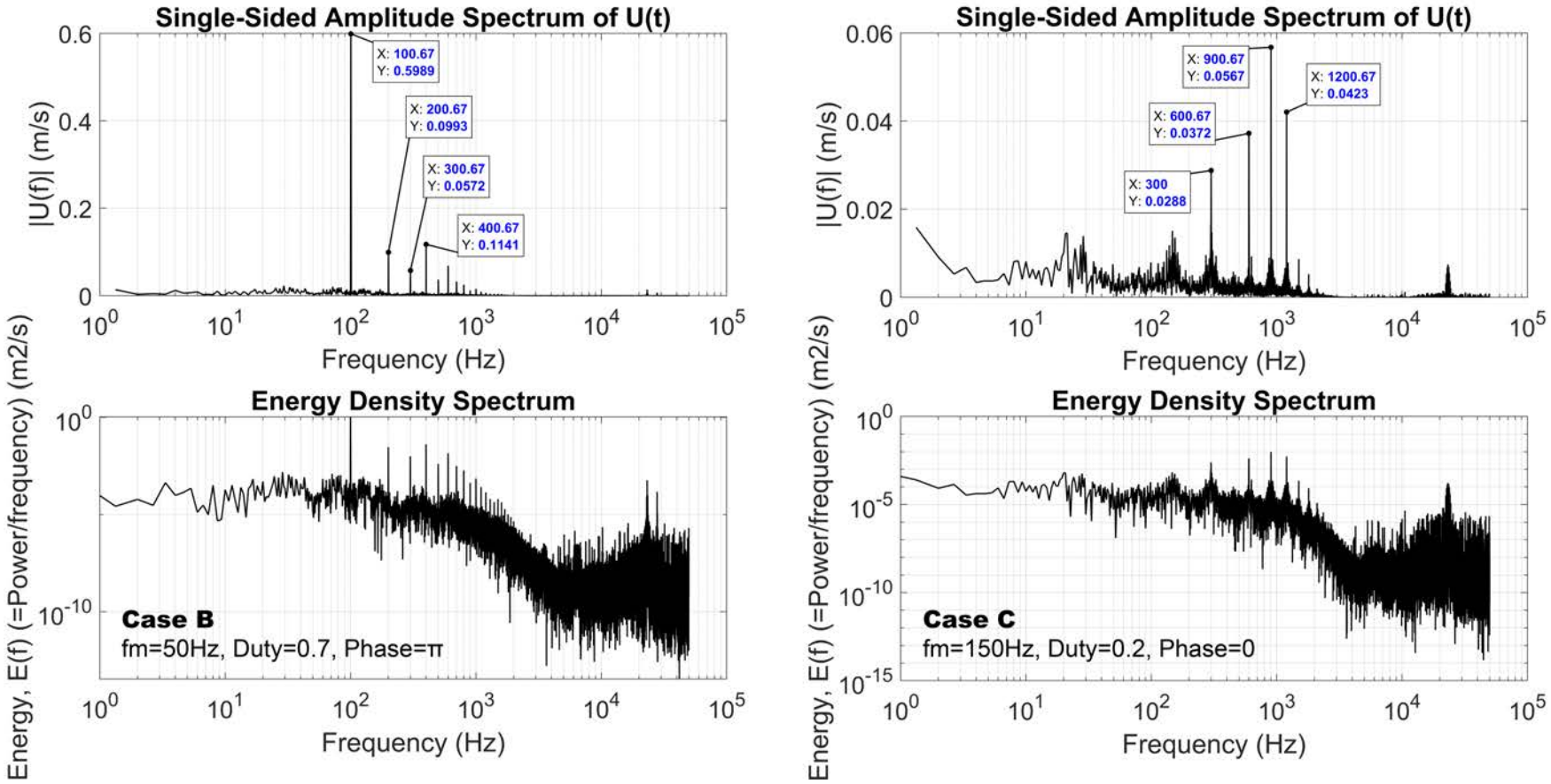

Figure 3.14: Single-sided amplitude and energy density spectra of all cases at x/h = 3, y/h = 0, and z/h = 0.5.

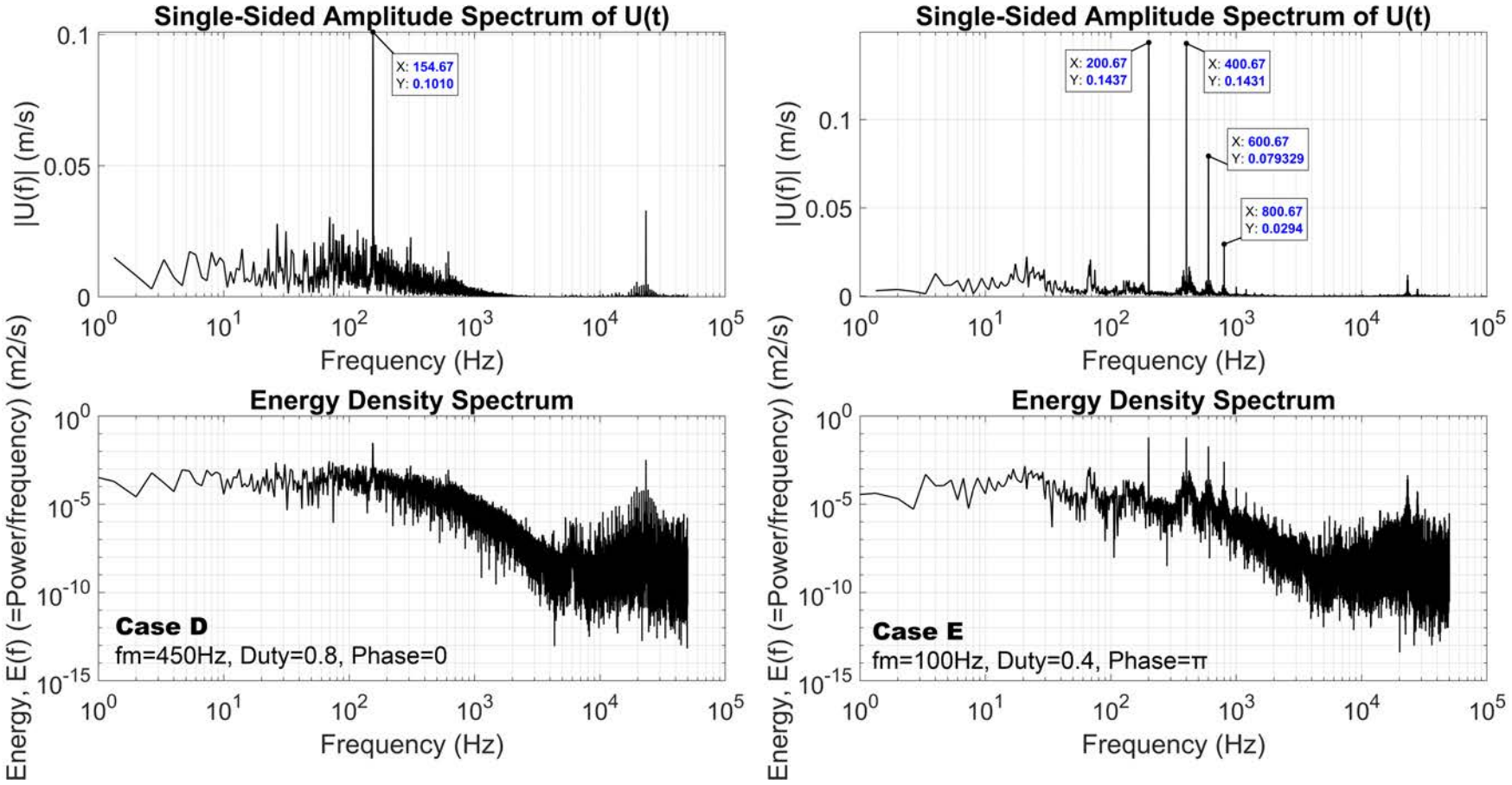

Figure 3.15: Single-sided amplitude and energy density spectra of all cases at x/h = 3, y/h = 0, and z/h = 0.5.

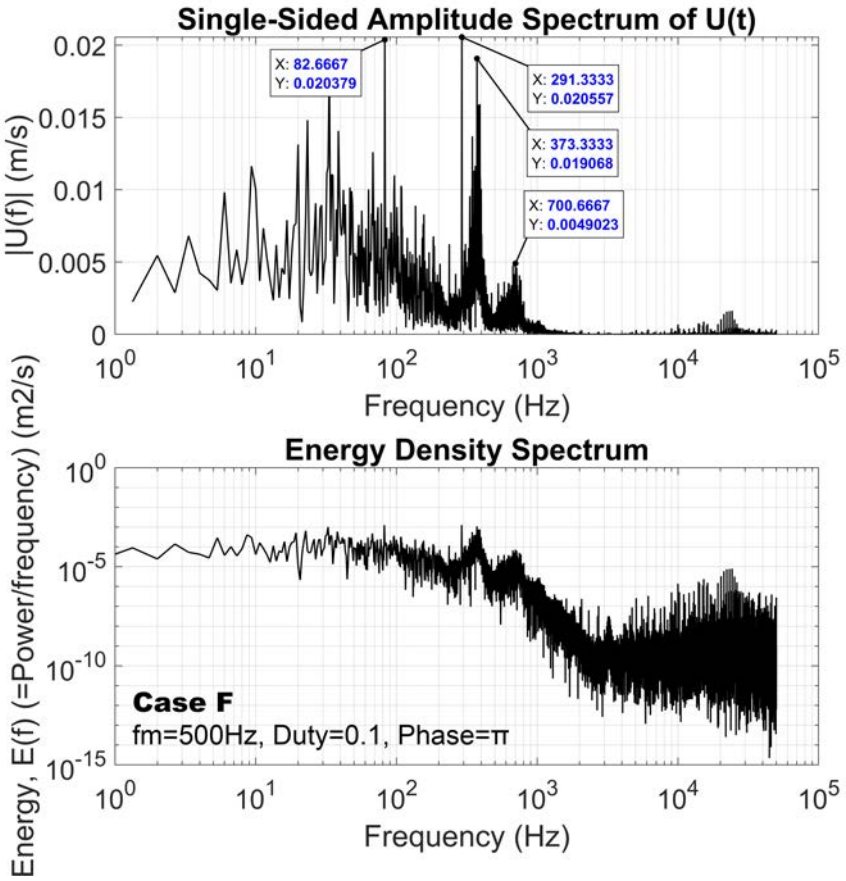

Figure 3.16: Single-sided amplitude and energy density spectra of all cases at x/h = 3, y/h = 0, and z/h = 0.5.

Case E was selected for further examination to understand this phenomenon. As in Fig. 3.17, the U-velocity trace has a repetitive pattern indicating that the raw velocity signal is the sum product of pure sine waves. The schematic in Fig. 3.18 illustrates the relationship between spanwise vortexes and velocity signal wave captured by a hot-wire probe. With a steady vortex pattern, a fixed hot-wire probe can measure the fluctuating velocity signals to detect the vortex

row as waves [71]. The wave frequency depends on the length scale or coherent sizes and background flow velocity at a lower frequency. Smaller vortices or a higher uniform velocity led to a higher frequency in the spectrum. I, II, III, and IV represent the positions of a vortex when it passes through the hot-wire probe, the matching results are shown on both the velocity trace in Fig. 3.17 and in the schematic in Fig. 3.18. Position II has the highest velocity because its position is the closest to the core of the vortex. Observing the visualization video shows the frequency of vortexes passing through the measured position equals the PA modular frequency f_m. The modular frequency corresponded with T_m which is the modular time between two vortexes passing through the hot-wire probe or the time between II - II in the velocity trace. Furthermore, the dominant frequency f_d was found to correspond with the dominant time period T_d measured between I - III, which was half of T_m. These results show that the frequency of vortexes passing through the hot-wire probe equals the PA modular frequency f_m. The dominant frequency f_d is twice the modular frequency f_m because one vortex passing through the hot-wire probe makes two peaks at the U-velocity component.

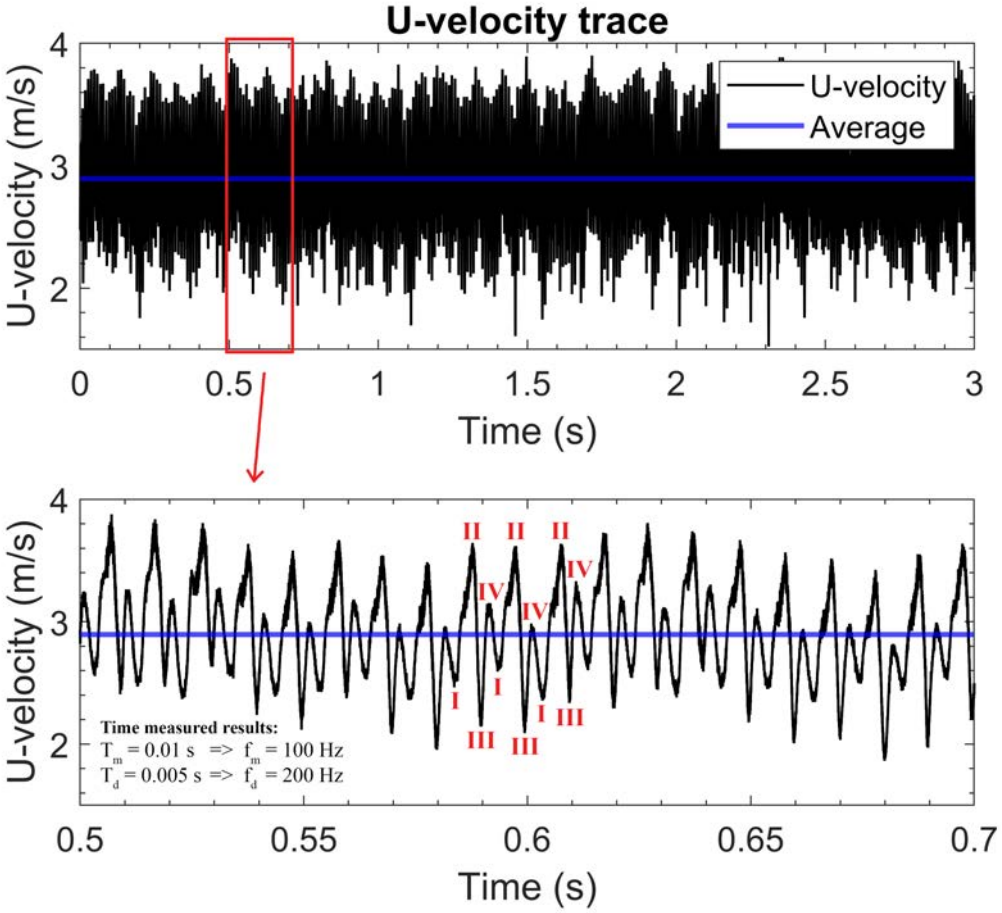

Figure 3.17: U-velocity trace on case E measured by hot-wire X-wire probe at 50-kHz sampling rate.

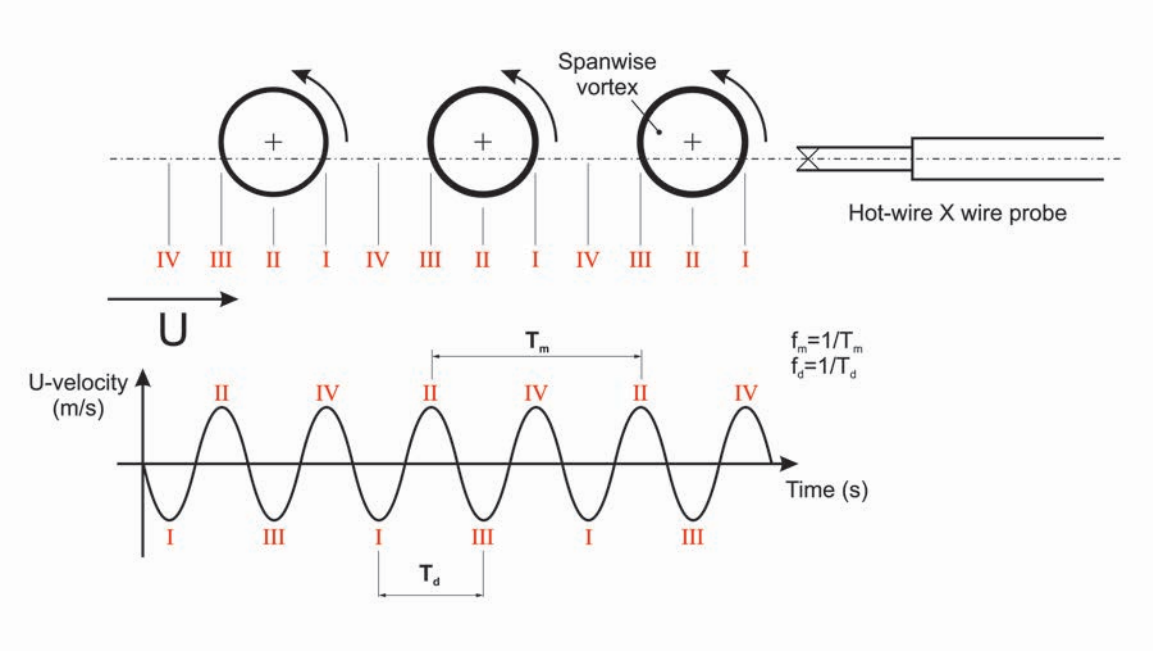

Figure 3.18: Relationship between spanwise vortexes and velocity signal wave captured by hot-wire probe.

$$St = \frac{f_d h}{U_0} = \frac{2 f_m h}{U_0}, \tag{3.3}$$

where:

St – Strouhal number;

f_m – PA modular frequency applied to the rectangular jet flow;

f_d – vortex shedding frequency, also known as the dominant frequency during analysis of the energy density spectrum;

h – characteristic length, i.e., the rectangular nozzle height;

U_0 – velocity of the initial flow.

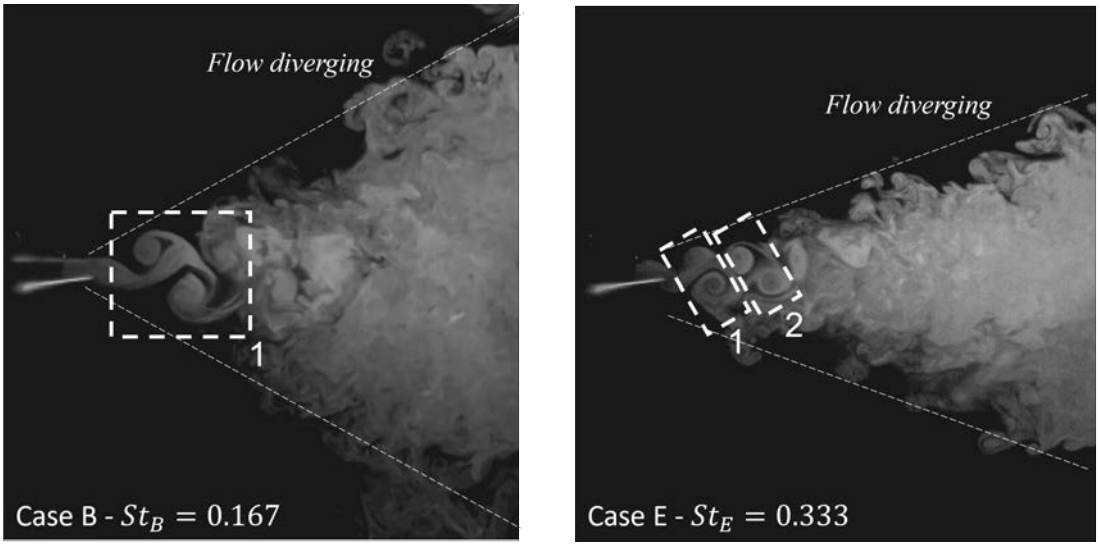

Figure 3.19: Flow pattern and St number for cases B and E.

Based on this analysis, the dominant frequency is the frequency corresponding to the maximum spectrum that can be directly calculated as double the PA modular frequency for cases where coherent structures exist, which is also the shedding frequency used in calculating the Strouhal number [46] [82]. The Strouhal number is related to the ratio of flow oscillations caused by the in-

ertial forces to the changes in velocity caused by the convective acceleration in flows where a periodic motion dominates. It reveals quantitative characteristics of coherent structures within the flow that can be seen in well-know Kármán vortex street [83]. As the coherent structure also can be observed in the HAR Rectangular jet controlled by PA, the Strouhal number also can be calculated using Eq. 3.3. Similar work as the classification of vortex patterns in oscillating foils by Strouhal number can be found in the work of Gungor *et al.* [84], and study of an acoustically excited plane jet at low Reynolds numbers of Marzouk *et al.* [85], which provides an overview of the various appearances and meaning of different St numbers. As the Strouhal number grows, so does the number of vortex pairs as can be seen in Fig. 3.19. There is just one vortex pair in Case B, where the Strouhal number is 0.167. However, two vortex pairs exist in Case E with a Strouhal number of 0.333. Additionally, the formation of the vortex structures on a large scale is observed and measured (see Fig. 3.4) and proves to be larger in the case of the Strouhal number while $St < 0.4$. This is consistent with Marzouk's experimental findings, as cited in [85]. As a result, the flow condition of a HAR rectangular jet controlled by PAs can be predicted by calculating the Strouhal number with a given excitation condition as the PA modular frequency and phase difference equal π.

3.4 Chapter Summary

- The periodic excitation and the vectoring effect transfer the high-aspect-ratio (width-to-height ratio 20) rectangular jets' mean energy to complex organized structures as spanwise vortexes. In two cases, this coherent structure is over-driven in the Kelvin-Helmholtz Instability: forming a large structure in the flow in low-range excitation frequency or suppressing the coherent structure and promoting disturbance in high-rage excitation frequency. Then, if a large coherent structure is formed, the energy cascading process makes the vortical structures smaller and smaller due to the interaction between multi-scale turbulence structures.

- The dissipative environment dilutes the vorticity of the coherent structures, making the compression of the coherent structures strengthen with the distance. As a result, the length of the spanwise vortex shortens when it travels streamwise resulting in a converging effect on the Top View and flow diverging on the Side View.

- By understanding the mechanism, the spanwise vortex created by PA can be utilized to introduce coherent structure into the flow to control the jet width; depending on the orientation of the PA versus the rectangular jets

(e.g., on the long edge or the short edge) converging or diverging effects can be archived. By utilizing this know-how, velocity and temperature of the rectangular jet can be controlled.

- The Strouhal number is used to predict the behavior of turbulent jets, such as their mixing properties and the noise they produce. The flow condition of an HAR rectangular jet controlled by PAs can be predicted by calculating the Strouhal number with a given excitation frequency as the PA modular frequency.

Chapter 4

Summary, Conclusions and Future Works

4.1 Summary

As a high-aspect-ratio rectangular jet is essential for various engineering applications, controlling this jet using an active flow control technique using plasma actuators opens new possibilities. The combination of modular frequency, duty, and phase difference determines the working condition of the plasma actuators and has different effects on the flow features. The PA can affect the initial vortex and overdrive the natural vortex generation frequency and size.

The plasma Actuator can perform active flow control with high-aspect-ratio

(width-to-height ratio 20) rectangular jets to enhance the centerline velocity and temperature performance. The velocity increased to 15% higher, and the temperature is 14% higher measured at the driver's location where x/h = 70 on the centerline as the initial target is a 20% improvement. With 362 tested cases and results of full fractional designs, the phase difference is the most important parameter to the velocity; it is also known that the timing of the induced wind as a modular frequency has a substantial effect on the velocity of the rectangular jet compared with duty. It can increase or decrease the velocity at a certain point and change the profile of the centerline velocity. Additionally, duty is the most important parameter to the temperature as changing the duty cycle influences the temperature better than the modular frequency. It can also affect the temperature at a particular point, centerline temperature profile, and temperature distribution across cut sections. It was also found that under specific conditions, the plasma actuator can cause the axis-switching phenomenon to occur at a location closer to the rectangular nozzle outlet (Case E), where x/h = 20–30. It results in a "thick" distribution of the high normalized temperature in this identical area.

The PA can introduce coherent structures to HAR rectangular jet flows. The combination of the periodic excitation and vectoring effects stemmed from the modular frequency and phase difference, respectively, which transfers the

mean energy of the flow to complex organized structures called spanwise vortexes. Simultaneously, during the formation of the coherent structures, the energy cascading process gradually decreases the vortical structures owing to the interaction between multi-scale turbulence structures. These spanwise vortexes create low-pressure zones when they travel streamwise that create suction, drawing low-energy air into the core of the vortexes. The concept of PV was used to explain the mechanism. When the rectangular jet flow is released into the still air, the flow enters a highly dissipative environment. This environment dilutes the vorticity of the coherent structures, making it decrease rapidly after fully forming spanwise vortexes. The compression of the coherent structures then occurs since the absolute vorticity must be proportional to the length of the coherent structure. As a result, the length of the spanwise vortex shortens when it travels streamwise resulting in a convergence effect from the X–Y Top View and a divergence effect from the X–Z Side View. Energy spectra analysis showed that PAs can overdrive the dominant frequency by doubling the modular frequency for cases where coherent structures are created. The flow features and quantitative characteristics of the rectangular jet flow controlled by PAs can be predicted by calculating the Strouhal number using the modular frequency applied to PA to control the flow.

4.2 Conclusion of thesis

The velocity and temperature performance are improved by using Plasma Actuator to actively control the high-aspect-ratio rectangular jet without increasing the air-conditional total energy budget. Just by changing the PA operating parameters, various flow effects will be created to fit various thermal conditions of an automobile.

For the novelty and academic contributions of this research, there are three points:

- Applying a small amount of control comparing the main jet energy at the beginning shear layer can affect the velocity and temperature performance further in the flow field. This can be done by manipulating (enhancing or suppressing) the integral length scale introduced into the flow (as can be seen in Fig. 1.11);
- Mechanisms of PAs to control sub-sonic high-aspect-ratio rectangular jet width are multi-scale turbulence structures, energy cascade, and potential vorticity;
- Among the operating parameters of Plasma Actuators, the most important parameter to control velocity and temperature is identified.

4.3 Future Works

If this technology is improved, it could open the opportunity to implement it in controlling air conditioner outlets for air conditioning applications because Plasma Actuator is a simple flow-control device that requires minor power input. By optimizing the operating conditions, further performance targeted at a 20% improvement could be achieved in the future concerning the velocity and temperature of the jet. As an active flow-controlling technique, PAs can create flow features without introducing new hardware into the flow. The actuator is a powerful tool for prototyping and crafting turbulent characteristics within the flow field of a rectangular jet. With this technique applied in automobiles, this could help to reduce fuel consumption and increase mileage. Also, understanding how the PA affects the HAR rectangular jet will help recreate flow features with other active flow control techniques and actuators for various engineering applications.

A high-aspect-ratio rectangular jet controlled by Plasma Actuators (PAs) will be implemented into a CFD simulation to have a better understanding of the phenomena occurring within the jet. This simulation will also serve as a valuable tool for studying the effects of using PAs to create turbulence structures without needing costly and time-consuming experiments.

In addition, the Plasma Actuators' size, shape, and working conditions will be altered to discover more flow features that can be introduced into the rectangular jet flow. By doing this, it is hoped that more will be learned about the flow dynamics and potential new ways to manipulate the flow using PAs will be found. The relation between the modular frequency and the HAR Rectangular Jets size is also a potential future work by conducting a parametric study. The appropriate modular frequency can be investigated using the Strouhal number to find the appropriate modular frequency for different velocities, HAR Rectangular Jet sizes, and other parameters. Different actuators will also be explored to actively control the flow in high-aspect-ratio rectangular jets. The goal is to identify the most effective means of controlling and manipulating the flow in these systems.

Published Contents

Chapter 2:

[1] A. V. Pham, K. Inaba, J. Yamaoka, and M. Sakai, "Effect of dbd plasma actuator on high aspect ratio rectangular jet," in *2020 JSAE Annual Congress Proceeding (Spring)*, 2020

[2] A. V. Pham, K. Inaba, M. Saito, and M. Sakai, "Effect of plasma actuator on velocity and temperature profiles of high aspect ratio rectangular jet," *Fluids*, vol. 7, no. 8, 2022

Chapter 3:

[3] A. V. Pham and K. Inaba, "Mechanisms of plasma actuators controlling high-aspect-ratio rectangular jet width for automobile air conditioning systems," *Fluids*, vol. 8, no. 7, p. 186, 2023

Bibliography

[1] M. Luo, Z. Wang, H. Zhang, E. Arens, D. Filingeri, L. Jin, A. Ghahramani, W. Chen, Y. He, and B. Si, "High-density thermal sensitivity maps of the human body," *Building and environment*, vol. 167, p. 106435, 2020.

[2] J. Costa, L. Oliveira, and M. Silva, "Energy savings by aerodynamic sealing with a downward-blowing plane air curtain—a numerical approach," *Energy and Buildings*, vol. 38, no. 10, pp. 1182–1193, 2006.

[3] G. Castiglioni, R. N. Russo, J. Mardall, and N. Mancini, "Thermal system with high aspect ratio vent," Nov. 5 2019, uS Patent 10,464,397.

[4] "Top 7 automotive hvac market trends," https://mobilityforesights.com/top-7-automotive-hvac-market-trends/, Apr 2021, [Accessed 15-Dec-2022].

[5] "Nissan IMk Concept — — nissan-global.com," https://www.nissan-global.

com/JP/INNOVATION/DESIGN/DESIGNWORKS/IMK/, [Accessed 15-Dec-2022].

[6] "2021 tesla model 3 price, reviews, pictures," https://cars.usnews.com/cars-trucks/tesla/model-3/2021, [Accessed 15-Dec-2022].

[7] "Nio et7: Our electric sedan with a range of up to 1000 km," https://www.nio.com/et7, [Accessed 15-Dec-2022].

[8] "Polestar 3: Polestar us," https://www.polestar.com/us/polestar-3/, [Accessed 15-Dec-2022].

[9] https://www.mitsuyaj.co.jp/dcms_media/other/mitsuyafan-technote.pdf.

[10] M. Jahanmiri, "Active flow control: a review," *Chalmers University of Technology*, 2010.

[11] N. Rajaratnam, *Turbulent jets*. Elsevier, 1976.

[12] T. Shakouchi *et al.*, "Jet flow engineering-fundamentals and application," *Morikita-shuppan Co*, 2004.

[13] R. C. Deo, J. Mi, and G. J. Nathan, "The influence of nozzle-exit geometric profile on statistical properties of a turbulent plane jet," *Experimental Thermal and Fluid Science*, vol. 32, no. 2, pp. 545–559, 2007.

[14] T. G.L, "Air velocity in ventilating jets," *ASHVE Transactions 59*, vol. ASHVE Research Report No. 1476, p. 261, 1953.

[15] H. B. Awbi, *Ventilation of buildings*. Routledge, 2002.

[16] I. Shepelev, "Supply ventilation jets and fountains," *Proceedings of the Academy of Construction and Architecture of the USSR*, vol. 4, 1961.

[17] K. Kraemer, "Die potentialströmung in der umgebung von freistrahlen," *Z. Flugwiss*, vol. 19, pp. 93–104, 1971.

[18] G. Heskestad, "Hot-wire measurements in a plane turbulent jet," *Trans ASME J Appl Mech*, vol. 32(4), pp. 721–31, 1965.

[19] N. E. Kotsovinos and E. J. List, "Plane turbulent buoyant jets. part 1. integral properties," *Journal of Fluid Mechanics*, vol. 81, no. 1, pp. 25–44, 1977.

[20] A. Koestel, "Pathsof horizontally projected heated and chilled airjets," *ASHVE Journal*, vol. Vol 27, no. 1, p. 55, 1955.

[21] G. Abramovich, "Free turbulent jets of liquids and gases," *Gos˜ nergoizdat, Moscow-Leningrad*, 1948.

[22] L. N. Cattafesta III and M. Sheplak, "Actuators for active flow control," *Annual Review of Fluid Mechanics*, vol. 43, pp. 247–272, 2011.

[23] R. Woszidlo, H. Nawroth, S. Raghu, and I. Wygnanski, "Parametric study of sweeping jet actuators for separation control," in *5th flow control conference*, 2010, p. 4247.

[24] A. Cutler, B. Beck, J. Wilkes, J. Drummond, D. Alderfer, and P. Danehy, "Development of a pulsed combustion actuator for high-speed flow control," in *43rd AIAA Aerospace Sciences Meeting and Exhibit*, 2005, p. 1084.

[25] Y. Katz, B. Nishri, and I. Wygnanski, "The delay of turbulent boundary layer separation by oscillatory active control," *Physics of Fluids A: Fluid Dynamics*, vol. 1, no. 2, pp. 179–181, 1989.

[26] L. Cattafesta, III, S. Garg, M. Choudhari, F. Li, L. Cattafesta, III, S. Garg, M. Choudhari, and F. Li, "Active control of flow-induced cavity resonance," in *28th Fluid Dynamics Conference*, 1997, p. 1804.

[27] H. Viets and M. Ball, "Forced vortices near a wall," in *19th Aerospace Sciences Meeting*, 1981, p. 256.

[28] C. Thill, J. Etches, I. Bond, K. Potter, and P. Weaver, "Morphing skins," *The Aeronautical Journal*, vol. 112, no. 1129, p. 117–139, 2008.

[29] T. C. Corke, C. L. Enloe, and S. P. Wilkinson, "Dielectric barrier dis-

charge plasma actuators for flow control," *Annual review of fluid mechanics*, vol. 42, pp. 505–529, 2010.

[30] A. Sfeir, "The velocity and temperature fields of rectangular jets," *International Journal of Heat and Mass Transfer*, vol. 19, no. 11, pp. 1289–1297, 1976.

[31] N. Benard, N. Balcon, and E. Moreau, "Electric wind produced by a surface dielectric barrier discharge operating over a wide range of relative humidity," in *47th AIAA Aerospace Sciences Meeting including The New Horizons Forum and Aerospace Exposition*, 2009, p. 488.

[32] T. C. Corke, M. L. Post, and D. M. Orlov, "Sdbd plasma enhanced aerodynamics: concepts, optimization and applications," *Progress in Aerospace Sciences*, vol. 43, no. 7-8, pp. 193–217, 2007.

[33] M. L. Post, *Plasma actuators for separation control on stationary and oscillating airfoils*. University of Notre Dame, 2004.

[34] R. D. Whalley and K.-S. Choi, "The starting vortex in quiescent air induced by dielectric-barrier-discharge plasma," *Journal of Fluid Mechanics*, vol. 703, pp. 192–203, 2012.

[35] N. Benard, J. P. Bonnet, G. Touchard, and E. Moreau, "Flow control by

dielectric barrier discharge actuators: Jet mixing enhancement," *AIAA Journal*, vol. 46, no. 9, pp. 2293–2305, sep 2008.

[36] T. Corke and E. Matlis, "Phased plasma arrays for unsteady flow control," in *Fluids 2000 Conference and Exhibit*, 2000, p. 2323.

[37] H. Jakob and M. K. Kim, "Feasibility study on the use of non-thermal plasma for a cold radio blackout experiment," in *AIAA Scitech 2020 Forum*, 2020, p. 2150.

[38] T. N. Jukes, K.-S. Choi, G. A. Johnson, and S. J. Scott, "Characterization of surface plasma-induced wall flows through velocity and temperature measurements," *AIAA journal*, vol. 44, no. 4, pp. 764–771, 2006.

[39] D. P. Rizzetta and M. R. Visbal, "Numerical investigation of plasma-based control for low-reynolds-number airfoil flows," *AIAA journal*, vol. 49, no. 2, pp. 411–425, 2011.

[40] S. Portugal, B. Choudhury, A. Lilley, C. Charters, C. Porrello, J. Lin, and S. Roy, "A fan-shaped plasma reactor for mixing enhancement in a closed chamber," *Journal of Physics D: Applied Physics*, vol. 53, no. 22, p. 22LT01, 2020.

[41] M. M. Wojewodka, C. White, and K. Kontis, "Effect of permittivity and

frequency on induced velocity in ac-dbd surface and channel plasma actuators," *Sensors and Actuators A: Physical*, vol. 303, p. 111831, 2020.

[42] E. Moreau, J. Cazour, and N. Benard, "Influence of the air-exposed active electrode shape on the electrical, optical and mechanical characteristics of a surface dielectric barrier discharge plasma actuator," *Journal of Electrostatics*, vol. 93, pp. 146–153, 2018.

[43] F. Rodrigues, A. Mushyam, J. Pascoa, and M. Trancossi, "A new plasma actuator configuration for improved efficiency: the stair-shaped dielectric barrier discharge actuator," *Journal of Physics D: Applied Physics*, vol. 52, no. 38, p. 385201, July 2019.

[44] D. Parekh, V. Kibens, A. Glezer, J. Wiltse, and D. Smith, "Innovative jet flow control-mixing enhancement experiments," in *34th Aerospace Sciences Meeting and Exhibit*, 1996, p. 308.

[45] P. Strykowski and R. Wilcoxon, "Mixing enhancement due to global oscillations in jets with annular counterflow," *AIAA journal*, vol. 31, no. 3, pp. 564–570, 1993.

[46] A. Ginevsky, Y. V. Vlasov, E. V. Vlasov, and R. Karavosov, *Acoustic control of turbulent jets*. Springer Science & Business Media, 2004.

[47] H. Suzuki, N. Kasagi, and Y. Suzuki, "Active control of an axisymmetric jet with distributed electromagnetic flap actuators," *Experiments in fluids*, vol. 36, no. 3, pp. 498–509, 2004.

[48] Y. Kozato, S. Kikuchi, S. Imao, Y. Kato, and K. Okayama, "Flow control of a rectangular jet by dbd plasma actuators," *International Journal of Heat and Fluid Flow*, vol. 62, pp. 33–43, 2016.

[49] S. Monin, Andre and A. M. Yaglom, *Statistical fluid mechanics, volume II: mechanics of turbulence*. Courier Corporation, 2013, vol. 2.

[50] E. List, "Turbulent jets and plumes," *Annual review of fluid mechanics*, vol. 14, pp. 189–212, 1982.

[51] L. A. El-Gabry, D. R. Thurman, and P. E. Poinsatte, "Procedure for determining turbulence length scales using hotwire anemometry," National Aeronautics and Space Administration, Tech. Rep., 2014.

[52] W. Thielicke and R. Sonntag, "Particle image velocimetry for matlab: Accuracy and enhanced algorithms in pivlab," *Journal of Open Research Software*, vol. 9, no. 1, 2021.

[53] S. Grosse and D. Angland, "Parametric investigation of the fluid mechanic

performance of an ac dielectric barrier discharge plasma actuator," *Journal of Physics D: Applied Physics*, vol. 53, no. 45, p. 455202, 2020.

[54] M. Forte, J. Jolibois, J. Pons, E. Moreau, G. Touchard, and M. Cazalens, "Optimization of a dielectric barrier discharge actuator by stationary and non-stationary measurements of the induced flow velocity: application to airflow control," *Experiments in fluids*, vol. 43, pp. 917–928, 2007.

[55] F. O. Thomas, T. C. Corke, M. Iqbal, A. Kozlov, and D. Schatzman, "Optimization of dielectric barrier discharge plasma actuators for active aerodynamic flow control," *AIAA journal*, vol. 47, no. 9, pp. 2169–2178, 2009.

[56] T. Abe, Y. Takizawa, S. Sato, and N. Kimura, "Experimental study for momentum transfer in a dielectric barrier discharge plasma actuator," *AIAA journal*, vol. 46, no. 9, pp. 2248–2256, 2008.

[57] K. Fukagata, S. Yamada, and H. Ishikawa, "Plasma actuators: Fundamentals and research trends," *Journal of Japan Society of Fluid Mechanics*, vol. 29, no. 4, pp. 243–250, 2010.

[58] H. D. Goodfellow and R. Kosonen, *Industrial Ventilation Design Guidebook: Volume 1: Fundamentals*. Academic Press, 2020.

[59] I. Shepelev and N. Gelman, "Universal equations for velocity and temper-

ature computation along the ventilation jets, supplied from rectangular outlets," *Water Supply Sanit Tech*, 1966.

[60] A. Tang, R. S. Vaddi, A. Mamishev, and I. V. Novosselov, "Empirical relations for discharge current and momentum injection in dielectric barrier discharge plasma actuators," *Journal of Physics D: Applied Physics*, vol. 54, no. 24, p. 245204, mar 2021.

[61] D. E. Ashpis, M. C. Laun, and E. L. Griebeler, "Progress toward accurate measurement of dielectric barrier discharge plasma actuator power," *AIAA Journal*, vol. 55, no. 7, pp. 2254–2268, 2017.

[62] E. Moreau, "Airflow control by non-thermal plasma actuators," *Journal of physics D: applied physics*, vol. 40, no. 3, p. 605, 2007.

[63] M. Bassett, D. Winterbone, and R. Pearson, "Calculation of steady flow pressure loss coefficients for pipe junctions," *Proceedings of the institution of mechanical engineers, part C: Journal of Mechanical Engineering Science*, vol. 215, no. 8, pp. 861–881, 2001.

[64] R. Farrington and J. Rugh, "Impact of vehicle air-conditioning on fuel economy, tailpipe emissions, and electric vehicle range," National Renewable Energy Lab.(NREL), Golden, CO (United States), Tech. Rep., 2000.

[65] N. Brelih, "How to improve energy efficiency of fans for air handling units," *REHVA J*, vol. 49, pp. 5–10, 2012.

[66] H. von Helmholtz, *über discontinuirliche Flüssigkeits-Bewegungen*. Akademie der Wissenschaften zu Berlin, 1868.

[67] W. S. THOMPSON, "Hydrokinetic solutions and observations," *Phil. Mag.*, no. 4, p. 374, 1871.

[68] N. Rajaratnam, *Turbulent jets*. The Netherlands: Elsevier, 1976, ch. 13, p. 267.

[69] C. Caulfield and W. Peltier, "The anatomy of the mixing transition in homogeneous and stratified free shear layers," *Journal of Fluid Mechanics*, vol. 413, pp. 1–47, 2000.

[70] F. Charru, *Hydrodynamic instabilities*. Cambridge University Press, 2011, vol. 37.

[71] J.-Z. Wu, H.-Y. Ma, and M.-D. Zhou, *Vorticity and vortex dynamics*. Springer Science & Business Media, 2007.

[72] A. N. Kolmogorov, "The local structure of turbulence in incompressible viscous fluid for very large reynolds numbers," *Cr Acad. Sci. URSS*, vol. 30, pp. 301–305, 1941.

[73] S. B. Pope and S. B. Pope, *Turbulent flows*. Cambridge university press, 2000.

[74] J. Hinze, "Isotropic turbulence," *Turbulence, Second Edition, McGraw-Hill, New York*, p. 790, 1975.

[75] H. Tennekes, J. L. Lumley, J. L. Lumley *et al.*, *A first course in turbulence*. MIT press, 1972.

[76] E. Palkin, M. Hadžiabdić, R. Mullyadzhanov, and K. Hanjalić, "Control of flow around a cylinder by rotary oscillations at a high subcritical reynolds number," *Journal of Fluid Mechanics*, vol. 855, pp. 236–266, 2018.

[77] X. Mao and B. Wang, "Spanwise localized control for drag reduction in flow passing a cylinder," *Journal of Fluid Mechanics*, vol. 915, 2021.

[78] M. V. Melander and F. Hussain, "Coupling between a coherent structure and fine-scale turbulence," *Physical Review E*, vol. 48, no. 4, p. 2669, 1993.

[79] J. R. Holton and G. J. Hakim, *An Introduction to Dynamic Meteorology (Fifth Edition)*. Boston: Academic Press, 2013.

[80] C.-G. Rossby, "Dynamics of steady ocean currents in the light of experimental fluid mechanics," *Massachusetts Institute of Technology and Woods Hole Oceanographic Institution*, 1936.

[81] C. G. Rossby, "Planetary flow pattern in the atmosphere. quart." *J. Roy. Meteor. Soc.*, vol. 66, pp. 68–87, 1940.

[82] H. Sakamoto and H. Haniu, "A Study on Vortex Shedding From Spheres in a Uniform Flow," *Journal of Fluids Engineering*, vol. 112, no. 4, pp. 386–392, 12 1990.

[83] N. D. Katopodes, *Free-surface flow: environmental fluid mechanics*. Butterworth-Heinemann, 2018.

[84] A. Gungor, M. S. U. Khalid, and A. Hemmati, "Classification of vortex patterns of oscillating foils in side-by-side configurations," *Journal of Fluid Mechanics*, vol. 951, p. A37, 2022.

[85] S. Marzouk and N. Hnaien, "Experimental study of an acoustically excited plane jet at low reynolds numbers," *Journal of Applied Fluid Mechanics*, vol. 12, no. 2, pp. 527–537, 2019.

[86] A. V. Pham, K. Inaba, J. Yamaoka, and M. Sakai, "Effect of dbd plasma actuator on high aspect ratio rectangular jet," in *2020 JSAE Annual Congress Proceeding (Spring)*, 2020.

[87] A. V. Pham, K. Inaba, M. Saito, and M. Sakai, "Effect of plasma actuator

on velocity and temperature profiles of high aspect ratio rectangular jet," *Fluids*, vol. 7, no. 8, 2022.

[88] A. V. Pham and K. Inaba, "Mechanisms of plasma actuators controlling high-aspect-ratio rectangular jet width for automobile air conditioning systems," *Fluids*, vol. 8, no. 7, p. 186, 2023.